UNIVERSITY OF CALIFORNIA, SAN DIEGO

IIIV/Si Nanoscale Lasers and Their Integration with Silicon Photonics

A dissertation submitted in partial satisfaction of the
requirements for the degree
Doctor of Philosophy

in

Electrical Engineering (Photonics)

by

Olesya Bondarenko

Committee in charge:

Professor Yeshaiahu Fainman, Chair
Professor Vitaliy Lomakin
Professor Shirley Meng
Professor Ivan Schuller
Professor Charles Tu

2015

ProQuest LLC.
789 East Eisenhower Parkway
P.O. Box 1346
Ann Arbor, MI 48106 - 1346

The dissertation of Olesya Bondarenko is approved, and it is acceptable in quality and form for publication on microfilm and electronically:

_____

_____

_____

_____

_____

Chair

University of California, San Diego

2015

DEDICATION

Посвящаю моим дорогим родителям, Елене Николаевне и Владимиру Степановичу Бондаренко.

EPIGRAPH

RESEARCH: That moment when not even Google knows what you are talking about.

—www.phdcomics.com

TABLE OF CONTENTS

LIST OF FIGURES

LIST OF TABLES

ACKNOWLEDGEMENTS

I would like to thank Professor Shaya Fainman for the opportunity to study the craft of experimental research by many a trial and error and the occasional success. Those few moments of success were entirely worth the hard work and frustration.

I would like to thank my fellow graduate students, for without their peer support, advice and great company the time in graduate school would have been so much harder. Every one of you contributed to my work directly or indirectly. In particular, I want to thank Dr. Maziar Nezhad and Dr. Aleksandar Simic for their invaluable senior student mentorship and guidance in the first years of school. I am very grateful to Dr. Janelle Shane and Dr. Qing Gu for their friendship, helpful discussions and great humor, which helped this dissertation to progress even in hardest of times.

I would like to thank Nano3 staff members for their enormous help, patience and kind understanding.

I am particularly grateful to you, Cesar. You were by my side through the hardest of times and shared with me so many happy moments. Thank you for your love, help, patience, understanding and true partnership. Thank you for being the part of my life.

I also want to thank all my friends for helping me to make it through the program as a sane and happy person. I am very thankful for the fun downtime, spark and adventures we shared, which mark graduate school not merely as six years of hard work, but also as a colorful period of my life, full of smart, interesting people and new experiences.

Finally, I am very thankful to my wonderful family: My grandparents for inspiring to become a scientist and holding so much pride in my every achievement; my brother Dmitriy for his ability to make my day even via Skype; my aunt Tatiana for her mentorship and support during my undergrad years. I am very grateful to my dear parents, Elena and Vladimir Bondarenko, for their endless support that made this epic journey possible.

Chapter 1, in part, is a reprint of the material as it appears in " Extremely compact hybrid III-V/SOI lasers: design and fabrication approaches," O. Bondarenko, C.-Y. Fang, F. Vallini, J. Smalley, and Y. Fainman, *Optics Express*, vol. 23, no. 6, pp. 2696–2712, 2015. The dissertation author was the primary co-investigator and coauthor of this paper.

Chapter 3, in full, is a reprint of the material as it appears in "Room-temperature subwavelength metallo-dielectric lasers," M. Nezhad, A. Simic, O. Bondarenko, B. Slutsky, A. Mizrahi, L. Feng, V. Lomakin, and Y. Fainman, *Nature Photonics*, vol. 4, issue 3, pp. 395–399, 2010. The dissertation author was the primary co-investigator and coauthor of this paper.

Chapter 4, in full, is a reprint of the material as it appears in "Wafer bonded subwavelength metallo-dielectric laser," O. Bondarenko, A. Simic, Q. Gu, J. H. Lee, B. Slutsky, M. P. Nezhad, and Y. Fainman, *IEEE Photonics Journal*, vol. 3, no. 3, pp. 608–616, 2011. The dissertation author was the primary co-investigator and coauthor of this paper.

Chapter 7, in full, is a reprint of the material as it appears in "Wafer bonded distributed feedback laser with sidewall modulated Bragg gratings," O. Bondarenko, Q, Gu, J. Shane, A. Simic, B. Slutsky, and Y. Fainman, *Applied Physics Letters* 103, 043105 (2013). The dissertation author was the primary co-investigator and coauthor of this paper.

VITA

2005	M. S. in Material Science *cum laude*, St Petersburg State Instute of Technology, St Petersburg, Russia
2005-2009	Research Assistant, Ioffe Institute of RAS, St. Petersburg, Russia
2009-2014	Research Assistant, University of California, San Diego
2011	M. S. in Electrical Engineering, University of California, San Diego
2015	Ph. D. in Electrical Engineering (Photonics), University of California, San Diego

PUBLICATIONS

O. Bondarenko, C.-Y. Fang, F. Vallini, J. Smalley, and Y. Fainman, " Extremely compact hybrid III-V/SOI lasers: design and fabrication approaches," *Optics Express*, vol. 23, no. 6, pp. 2696–2712, 2015.

Q. Gu, J. ST Smalley, M. P. Nezhad, A. Simic, J. - H. Lee, M. Katz, **O. Bondarenko**, B. Slutsky, A. Mizrahi, V. Lomakin and Y. Fainman, "Sub-wavelength semiconductor lasers for dense chip-scale integration," Advances in Optics and Photonics, vol. 6, no. 1, 1-56 (2014).

O. Bondarenko, Q. Gu, J. Shane, A. Simic, B. Slutsky and Y. Fainman, "Wafer Bonded Distributed Feedback Laser with Sidewall Modulated Gratings", Appl. Phys. Lett. 103, 043105 (2013).

J.-H. Lee, M. Khajavikhan, A. Simic, Q. Gu, **O. Bondarenko**, B. Slutsky, M. P. Nezhad, and Y. Fainman "Electrically pumped sub-wavelength metallo-dielectric pedestal pillar lasers", Optics Express, Vol. 19, No. 22 (2011).

M. Nezhad, **O. Bondarenko**, M. Khajavikhan, A. Simic, and Y. Fainman, "Etch-free low loss silicon waveguides using hydrogen silsesquioxane oxidation masks", Optics Express, Vol. 19, No. 20 (2011).

O. Bondarenko, A. Simic, Q. Gu, J.-H. Lee, B. Slutsky, M. P. Nezhad, Y. Fainman "Wafer bonded metallodielectric subwavelength laser", (Invited, Focus issue), IEEE Photonics Journal, Vol. 3, No. 3 (2011).

M.P. Nezhad, A. Simic, **O. Bondarenko**, B. Slutsky, A. Mizrahi, L. Feng, V. Lomakin, and Y. Fainman, "Room-temperature subwavelength metallo-dielectric lasers", Nature Photonics 4 (2010).

V. Mamutin,**O. Bondarenko**, A. Vasil'ev, A. Gladyshev, A. Egorov, N. Kryjanovskaya, V. Mikhrin, V. Ustinov, "Optical properties of strain-compensated InAs/InGaAsN/InGaAs superlattices", Technical Physics Letters, Vol. 33, No 9, (2007).

V. Mamutin, **O. Bondarenko**, A. Egorov, N. Krijanovskaya, Yu. Shernyakov, V. Ustinov, "Lasing properties of strain-compensated InAs/InGaAsN/GaAsN heterostructures in 1.3-1.55 micron spectral range", Technical Physics Letters, Vol. 32, No 3, (2006).

L. Vorob'ev, D. Firsov, V. Shalygin, V. Panevin; A. Sofronov, D. Tsoi, A. Egorov, A. Gladyshev, **O. Bondarenko**, "Impurity breakdown and electroluminescence in the terahertz range in p -GaAs and p -GaAsN microstructures", Technical Physics Letters, Vol. 32, No 5, (2006).

ABSTRACT OF THE DISSERTATION

IIIV/Si Nanoscale Lasers and Their Integration with Silicon Photonics

by

Olesya Bondarenko

Doctor of Philosophy in Electrical Engineering (Photonics)

University of California, San Diego, 2015

Professor Yeshaiahu Fainman, Chair

The rapidly evolving global information infrastructure requires ever faster data transfer within computer networks and stations. Integrated chip scale photonics can pave the way to accelerated signal manipulation and boost bandwidth capacity of optical interconnects in a compact and ergonomic arrangement. A key building block for integrated photonic circuits is an on-chip laser. In this dissertation we explore ways to reduce the physical footprint of semiconductor lasers and make them suitable for high density integration on silicon, a standard material platform for today's integrated circuits. We demonstrated the first room temperature metalo-dielectric nanolaser, sub-wavelength in all three dimensions. Next, we demonstrated a nanolaser on silicon, showing the feasibility of its integration with this platform. We also designed and realized an ultracompact feedback laser with

edge-emitting structure, amenable for in-plane coupling with a standard silicon waveguide. Finally, we discuss the challenges and propose solutions for improvement of the device performance and practicality.

Chapter 1

Introduction

Global data traffic is expected to exceed the zetabyte mark by 2017 due to the exponentially growing number of Internet applications for stationary and mobile devices, as well as the number of their users, according to the recent Cisco Visual Network Index (VNI) forecast. Several new trends are driving this rapid expansion, including high definition mobile-to-mobile video streaming, Internet of Things phenomena and rapid cloud computing [1]. Support of high information density requires powerful processing capabilities for fast data access. This is important not only in datacenters but also in computational research labs and supercomputers, where large amounts of data have to be processed quickly. Consequently, efficient information transfer between microprocessor cores, memory and peripherals is essential.

Significant advances in communication technologies are vital to keep up with this progression. State of the art 40 Gb/s and 100 Gb/s data transmission protocols are supported with both copper wire and fiber optics [2]. Theoretically, however, optical interconnects make a stronger contender for high speed networks due to their exceptional potential for higher bandwidth, lower latency, lower energy consumption, and scalability [3]. New fiber technologies (multi-core and hollow core fiber) have enabled up to 100 Tb/s aggregate transmission rate in a single fiber [4]. Further, several types of multiplexing technologies offer extra leeway in bandwidth capacity enhancement [5, 6]. The achievement of Tb/s range bandwidth capacity is of particular significance for massively parallel computing,

many fundamental physics experiments and state of the art reduced-latency internet applications, such as video surveillance, telemedicine, smart car navigation, tracking and more [7]. Although these record numbers are shown in optical fiber, many of the bandwidth enhancement techniques, such as wavelength and mode division multiplexing, are also applicable to silicon photonics [8, 9], where the limits are currently being explored. Recent examples include the first demonstration of the wavelength division multiplexing (WDM) compatible silicon photonic platform, with aggregate data rates up to 60 Gb/s [10] and 1x8 Mach-Zehnder WDM (de)multiplexers fabricated using a standard 90 nm CMOS process [11].

While optical interconnects already comprise the backbone of modern information processing systems, low cost electronics will continue to support many important functions such as data transport monitoring, switching, modulation, forward error correction, and fault control. However, efficient data conversion between the optical and electrical domains relies upon seamless integration of multiple components, such as lasers, modulators, detectors, amplifiers, multiplexers, demultiplexers and logic. Systems assembled with many discrete components need to be further aligned and interconnected with optical fibers and copper wires. For example, a single 40 channel WDM terminal node can contain more than 100 devices and components and nearly 300 fiber coupling connections [12]. Hence, various types of losses can accrue quickly, dramatically increasing power consumption and leading to high maintenance costs for these systems. The sheer number of wires and fibers, growing in response to ever-increasing volumes of data, will soon become architecturally and ergonomically unviable. The recent U.S. Government overview of best practices for energy-efficient data centers design suggested implementation of energy efficient cooling systems, higher efficiency equipment and consolidation of components [13]. Evidently, to overcome these deficiencies we need to develop new integration platforms for efficient, scalable and multifunctional integrated systems. One of the key elements required to enable such integrated systems is an ultra-compact, energy efficient and robust near infrared laser source.

A major driving force of optical interconnects research is device and circuit footprint reduction for scalable on-chip networks [14]. In this quest for the ultimate

miniaturization, a variety of subwavelength lasers have been demonstrated [15–18], including an epitaxially grown nanolaser on silicon [9], a IIIV/Si photonic crystal nanolaser [18] and a wafer bonded nanolaser on silicon [19]. We have previously shown that room temperature lasing could be achieved using metal-dielectric and coaxial sub-wavelength cavities [20–22]. These metal-based resonators are also uniquely suitable for high density integration, since this design limits cross-coupling between adjacent devices [23].

In this dissertation we explore new design and fabrication approaches with the goal of enabling ever smaller hybrid III-V/Si lasers. In this chapter we give a brief overview of state of the art hybrid photonic devices and integration technologies.

1.1 Chip scale integrated photonics: state of the art

While on-chip PICs do not currently enable as much bandwidth capacity as optical fibers, they have many advantages. Firstly, they can be mass produced at a very low cost in a standard CMOS foundry, rather than assembled from multiple parts made with various expensive compound semiconductor technologies. Secondly, consolidation of as many components as possible on a single chip will improve overall efficiency of information processing networks and clean up the complexity in data centers. In particular, silicon makes a great material platform for on-chip PICs. Low optical loss, mature technology, great potential for miniaturization and an extensive library of silicon-based photonic and electronic devices make silicon photonic circuits a future technology for chip scale optical information processing.

Notable advances have been made in the industry within the past few years. In 2010 IBM announced a new CMOS integrated nanophotonics technology for dense integration of electrical and optical devices on a silicon chip. This technology enables monolithic integration of electrical and optical circuits on the same chip via the front-end of a standard 90 nm CMOS line. Over several years IBM Research has

developed a whole library of front-end integrated active and passive silicon devices, scaled down to the diffraction limit [23]. In 2013, Intel announced transceiver and connector modules based on silicon photonics technology, which will be able to carry 100 Gb and 1.6 Tb of data per second, respectively. The Intel connector can optically convert bits of information and send them through 64 optical fibers at once [24]. In 2013 Skorpios Technologies and Aurrion, reported the first III-V/SOI hybrid lasers, fabricated in a commercial CMOS foundry [25, 26]. These breakthrough technologies can significantly reduce the costs of running a data center.

An emerging trend of mid-infrared PICs (wavelength range of 2-10 µm) takes integrated photonics beyond telecommunications and expands its applications to portable sensing, imaging and spectroscopy. Advancements in mid-IR photonics may greatly enhance analytical capabilities of life sciences, defense, pharmaceutical and food industries in a compact and inexpensive format. One of the difficulties this research is facing today is the strong light absorption in SiO_2 above 4 µm. The standard silicon-on-insulator (SOI) platform is sub-optimal in this wavelength range and needs to be replaced by a material transparent in the mid-IR. As such, silicon-on-sapphire or silicon-on-silicon nitride are potential candidates for CMOS compatible mid-IR PICs. The scope of this paper is limited to near-IR hybrid lasers, thereby we suggest a recent paper by Roelkens et al. [27] for further reading on mid-IR photonics.

1.2 Active optical components on silicon

An array of CMOS compatible hybrid components has been reported in the literature including electro-refractive and electro-absorptive silicon optical modulators [28, 29], high performing photodetectors in silicon [30, 31] germanium [32, 33] and even graphene [34]. Light generation and amplification has also been demonstrated in indirect bandgap materials such as silicon and germanium, but building high performance lasers with these materials is still facing considerable complications. For example, Raman lasers require an external optical pump to trigger

Raman scattering in silicon and induce Raman amplification [35]. An electrically pumped Raman laser is fundamentally attainable, but a highly complex engineering endeavor [36]. Silicon and germanium can also exhibit optical gain under tensile stress due to bandgap modification, as exemplified by recent demonstrations of electrically pumped strained germanium lasers [37, 38]. However, the lasing threshold in these devices is still in the hundreds of $\mathrm{kA/cm^2}$ range, compared to 1-3 $\mathrm{kA/cm^2}$ in III-V semiconductor laser diodes [39, 40].

Most III-V compound semiconductors are direct bandgap materials with gain values often in the range of several thousand $\mathrm{cm^{-1}}$ [39]. Other advantages of III-V compounds include bandgap energies that can be tuned by varying the alloy composition, as well as high carrier mobilities [41]. Unsurprisingly, III-V semiconductors remain the materials of choice when high optical gain or fast electronic response is required. Frequently implemented heterogeneous integration solutions of III-V and silicon components are flip-chip bonding and chip-to-chip butt coupling. Both technologies are very advanced, reliable and allow submicron alignment precision. A great example of an efficient flip-chip bonded laser is the device demonstrated by researchers from Fujitsu [42]. The laser exhibited high wall plug efficiency(WPE) of 7.6 %. High precision flip-chip bonding technology with exceptionally low alignment error ($\approx$0.1 µm) was a crucial factor in misalignment loss reduction.

The highest reported WPE to date (9.5 %) has been achieved in a hybrid laser by Kotura (Mellanox) [43]. The Kotura design utilizes an external cavity reflective semiconductor optical amplifier (SOA), butt-coupled to a silicon waveguide Bragg mirror on SOI chip. A spot size converter is also an important part of the design and is incorporated to minimize coupling losses. This approach has proven to work very well for realization of high efficiency and high power hybrid lasers. With this cavity design (reflective SOA and waveguide mirror) and device-to-waveguide coupling architecture, Oracle has reported a butt-coupled laser with waveguide coupled power of 20 mW, tuning range of 8 nm and 35 nm, depending on tuning mechanism, and WPE of 7.8 % [44]. Flip-chip bonding and butt coupling are amongst the best technologies to achieve the record device performance when

the footprint is not a concern. However, another approach is required when the component features are deeply sub-micron. In this case, monolithic integration of as-grown III-V and Si materials, followed further by processing of III-V/Si composite material as a single monolithic structure, is naturally a better choice. The main advantage of monolithic integration is that alignment can be avoided altogether.

Two fundamentally different approaches to monolithic integration have emerged in pursuit of merging III-V's and silicon: epitaxial growth and wafer bonding. Strong lattice mismatch between silicon and III-V compounds presents a great technological roadblock to the former [45–47]. Despite this, several as-grown III-V/Si lasers have been demonstrated including the recently reported first electrically pumped edge-emitting III-V nanowire laser on silicon [9, 48, 49]. The alternative approach, wafer bonding, has yielded the best results so far, both in terms of scalability and laser performance, which will be discussed in greater detail in the following section.

Among many types of lasers to be developed for the new generation integrated chip scale photonic circuits, DFB lasers have drawn particular interest in the research community. Because Bragg gratings allow a limited phase window for constructive interference, DFBs provide extremely stable, single mode, narrow linewidth operation. Such signals can propagate in optical fibers or waveguides with minimal dispersion and noise. In optical communications, this translates into preserving signal integrity over long propagation distances. The wavelength stability can further be reinforced with single or multiple quarter-wave shifted cavity designs [50]. Additionally, the emission frequency of semiconductor DFB lasers can be tuned via temperature modulation or electrical injection [39].

The first monolithically integrated III-V/Si microdisk laser was demonstrated by Rojo Romeo et al [51]. The authors used molecular wafer bonding to create the III-V/SiO_2/Si composite with $\approx$1.2 µm SiO_2 mediating layer. At the same time, Fang et al. [52] reported the III-V/Si evanescent laser. In this case the optical mode propagates in the silicon waveguide with its evanescent tail interacting with the III-V slab. The authors used plasma assisted wafer bonding, a type of direct hydrophilic bonding. This was an important milestone on the way to

chip scale integrated photonic circuits, as the direct contact between III-V and Si enabled easy, low loss mode coupling between active and passive circuit elements, as well as CMOS compatibility for part of the fabrication process. This work was shortly followed by demonstrations of other types of evanescent devices and an entire evanescent photonic link with lasers, modulators and photodetectors [53–55]. Some of the hybrid devices are already on their way to commercialization. The latest works on wafer bonded hybrid lasers include a BCB bonded DFB [56], a tunable hybrid laser [57], an integrated four-wavelength laser array [58], a sidewall modulated DFB [59], a microlaser [60], a nanolaser [19] and a slotted feedback laser [61]. Recently Santis et al. [62] proposed hybrid cavities as a way to dramatically reduce linewidth in semiconductor lasers by limiting spontaneous emission noise. These works use varying monolithic integration approaches, which we will discuss in the following section.

1.3 Wafer bonding methods

All existing wafer bonding techniques can be roughly divided into two broad classes: direct and indirect. Direct methods rely on molecular forces between the two materials. The main advantage of direct methods is the immediate vertical proximity between the III-V and silicon layers, which allows the composite structure to be treated as a single wafer during fabrication and hybrid device design. Atomic flatness and pristine condition of both surfaces are imperative for direct methods to work [63]. Pressure [64] or thermal treatment [65, 66] (or both) are usually applied to assist molecular-level interactions. Hydrophilic [63, 67] and hydrophobic [64, 68] bonding are examples of the direct bonding technique. In hydrophobic bonding, all native oxides must be stripped to leave both surfaces hydrogenated, and bonding is carried out in vacuum, under pressure at room or elevated temperatures [64, 66, 68]. Hydrophilic bonding relies on Van der Waals forces to facilitate attraction between the surface species. Either wet chemistry or plasma treatment can be used to make the surfaces hydrophilic. After Van der Waals bonding, the composite structure typically undergoes thermal processing to

encourage covalent bond formation.

Indirect methods use a third mediating material between the materials to be bonded. Metal-based [69–71] anodic [72] and adhesive bonding methods [73, 74] are all indirect methods. The indirect approach helps to circumvent the problem of lattice mismatch, surface roughness and poor planarity.

Metal-based bonding techniques are perhaps the oldest and most established to date. The oldest, thermocompression bonding [69], relies on atom diffusion between different metals at elevated temperatures. Another popular indirect method, eutectic bonding, is similar to soldering and based on metal alloy formation [70, 71, 75]. Eutectic bonding uses lower temperatures than thermocompression, but may have poor bond stability. It is also incompatible with CMOS processing because of ion diffusion.

Anodic bonding is normally used for bonding semiconductors to borosilicate glasses. Strictly speaking, anodic bonding does not require an extra material layer, but one of the materials (typically, the glass cathode) must be doped with high mobility charge carriers [66, 72]. This can have an adverse effect on electronic device performance and, thus, is not a good choice for CMOS integration.

Some of the popular wafer bonding adhesives include bensocyclobutene (BCB) by Dow corning, SU-8 polymers [73], and hydrogen silsesquioxane (HSQ) [74]. Typically, adhesive wafer bonding is carried out at lower temperatures than most other wafer bonding techniques, but the downside is low temperature stability of the bonding interface and poor surface quality.

In the rest of this review, we will focus on the direct bonding approach of III-V to silicon on insulator (SOI).

Chapter 1, in part, is a reprint of the material as it appears in " Extremely compact hybrid III-V/SOI lasers: design and fabrication approaches," O. Bondarenko, C.-Y. Fang, F. Vallini, J. Smalley, and Y. Fainman, *Optics Express*, vol. 23, no. 6, pp. 2696–2712, 2015. The dissertation author was the primary co-investigator and coauthor of this paper.

Chapter 2

Experimental methods

In this work we fabricated and tested three optically pumped nanoscale semiconductor lasers: subwavelength laser with hybrid metalo-dielectric optical cavity (Chapter 3), wafer bonded nanolaser (Chapter 4) and wafer bonded edge emitting distributed feedback laser (Chapter 7). Despite their dissimilar design, their fabrication flows are analogous and share most steps, including plasma assisted wafer bonding, electron beam (ebeam) writing, reactive ion etching (RIE), plasma enhanced chemical vapor deposition (PECVD) and sputtering. For some of the nanofabrication steps we were able to use the standard tool manufacturer recipes, for instance, SiO_2 etching in Oxford P80 and Al_2O_3 atomic layer deposition (ALD) in Beneq TFS200). However, most steps required optimization. Specifically, we developed plasma assisted wafer bonding for several pairs of wafers (InGaAsP/InP bonding to bare Si, SiO_2-on-Si and SOI), ebeam patterning of hydrogen silsesquioxane (HSQ) resist, RIE of InGaAsP and PECVD of thin SiO_2 films. We also applied conceptually identical device characterization methodologies to our lasers. Nonetheless, we had to alter the optical injection scheme to measure both vertically and edge emitting laser, as well as add a fiber-coupled characterization arm for high resolution spectral measurements. We also built a setup for transmission measurements of waveguides with gain (see Chapter 8). In this chapter we describe the fabrication and characterization methods we have developed and applied to the nanoscale lasers discussed in this work.

2.1 Fabrication

2.1.1 Plasma assisted wafer bonding

We used a plasma-assisted wafer bonding method to transfer a thin epitaxial InGaAsP layer from its native InP substrate to Si (SiO_2/Si, SOI) wafers. This method has two advantages with respect to our device design. Namely, this technique allows to bond wafers directly, without a thick mediating material; it is also a fairly low temperature process ($\leq 300\,^{\circ}C$). The latter prevents epitaxial layer damage due to the difference in thermal expansion coefficients of InGaAsP and Si [63].

Our wafer bonding process flow includes several key steps: (1) III-V and Si wafer preparation and wet cleaning, (2) O_2 plasma activation of wafer surfaces, (3) III-V and Si wafer manual mating, (4) thermal anneal of the bonded wafer pair (may be under pressure), (5) wet etching of a native carrier substrate of the InGaAsP epitaxial layer (see Figure 2.1, a, for a schematic presentation). Specific bonding processes, developed for InGAsP-to-SiO_2/Si and InGaAsP-to-SOI, are described in detail in the Chapters 4 and 7. The goal of this chapter is to outline the problems we faced while developing the process and our solutions to these problems.

At first we attempted to closely follow the wafer bonding process protocol presented by Liang et al [76]. The authors demonstrated a high quality plasma assisted wafer bonding of a 100mm silicon-to-silicon wafer bonded pair and a $1\,cm \times 1\,cm$ III-V/Si pair with post-bond anneal at $300\,^{\circ}C$ with applied pressure of $1.5\,MPa$, using a commercial wafer bonder. Prior to the anneal, the samples underwent multiple wet cleaning steps, growth of a thin ($\approx$60 nm) mediating SiO_2 layer and a post-plasma surface activation with NH_4OH. As described, the process did not work in our cleanroom conditions and we adapted the original procedure as follows:

– We substituted a commercial wafer bonder with a custom-made hydraulic press fixture. It was designed to apply pressure to a sample pair during the anneal on a hotplate. The fixture translated a 7 lb weight onto a sample with

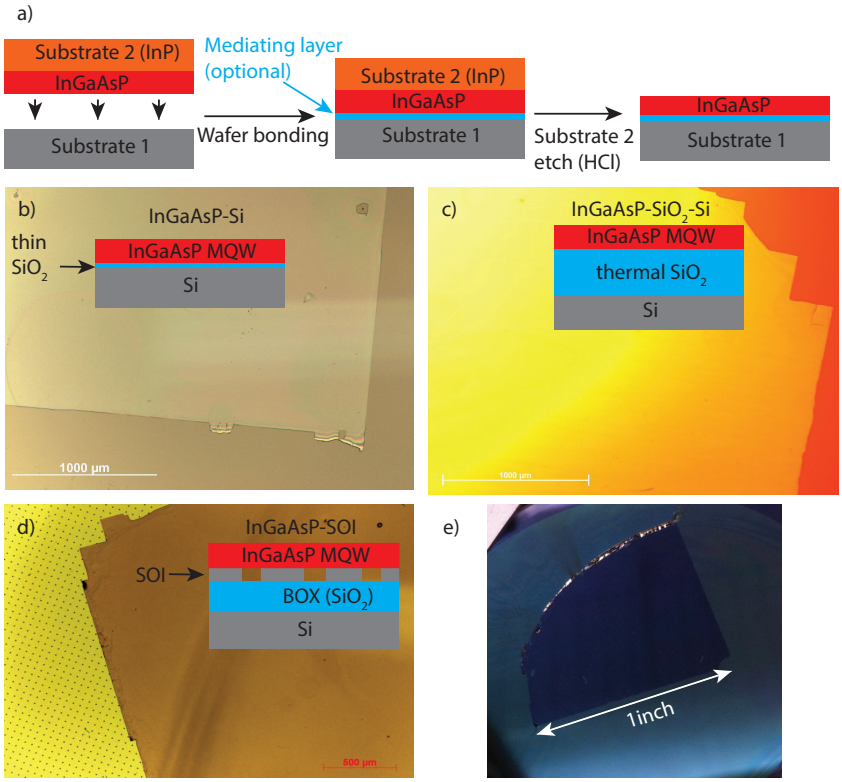

Figure 2.1: Optical microscope images of wafer bonded samples: a) epitaxial layer of InGaAsP bonded to Si with a thin layer (40-60 nm) SiO_2 as a mediating layer; b) InGaAsP on thick (6 µm) thermally grown SiO_2-on-Si; c) InGaAsP on SOI wafer with VOC.

1×1 inch^2 area. This weight exerted a 50 kPa, pressure to the surface of the sample. Placing the sample on a cold hotplate is extremely important, i.e. we applied the weight first and only then ramped up the hotplate temperature. Placing the bonded sample on a pre-heated hotplate causes rapid desorption of the interfacial H_2O molecules, breaking the wafers in the pair apart. In this form, the wafer bonding process worked only on occasion. Eventually we replaced the hotplate-press anneal method with an overnight (≈14-20 hours) anneal in a forced draft furnace (Fisher) at 300 °C and atmospheric pressure. This method yielded consistent success for the InGaAsP/SiO_2-on-Si and InGaAsP/SOI with vertical outgassing channels (VOC) [65].

– We amended the pre-bond wafer cleaning process, because the RCA-2 clean (1 part of 29 % HCl, 1 part of 29 % H_2O_2 and 6 parts H_2O), prescribed for

III-V in the source, reacted with InGaAsP surface. Surface roughness, caused by the reaction was an important factor in the regular bonding failure. To eliminate this problem, we replaced RCA-2 by RCA-1clean (1 part of 29 % NH_4OH, 1 part of 29 %H_2O_2 and 5 parts of H_2O), which did not affect the InGaAsP surface this way. Both RCA cleans were heated to 65-80 °C before use. Later we simplified the cleaning process further by substituting RCA-1 with 29 % NH_4OH to clean InGaAsP/InP wafers and RCA-2 with a mixture of 3 parts H_2SO_4 and 1 part H_2O to clean silicon-based wafers. We also omitted the external heating of these cleaning solutions in the final process. This cleaning step serves the purpose of removing organic contaminants from the wafer surfaces. However, it leaves a thin film of oxide on the surface of the silicon wafer, which needs to be subsequently dissolved in diluted (≈1-2 %) HF. Finally, we omitted the wafer swabbing under a microscope, as we concluded that introduces more particles rather than it removes.

– We replaced NH_4OH vapor activation with DI water dip activation right after O_2 plasma surface activation and prior to thermal anneal to facilitate the Van der Waals bonding between the wafer pairs.

After much experimentation, we can summarize the factors critical to a successful wafer bonding process:

– Extremely careful wafer handling throughout the entire process is imperative to exclude, or at least limit, surface exposure to microscopic particles and other contaminants. The wafer surfaces should stay in as pristine condition as possible, as well as beakers, tweezers and other tools that come in contact with them. If the plasma activation step is carried out on shared equipment, a thorough chamber clean (wet and oxygen plasma) should precede the activation step.

– Appropriate wet chemistry choice is necessary to eliminate surface damage even on a microscopic level, since the surface roughness must be sub-nanometer for a successful bond [63].

– Sealing the bonded III-V wafer edges with a washaway wafer mounting adhesive, such as Crystalbond, or a photoresist prior to the native III-V substrate removal (etching in HCl, in our case) helps to prevent epitaxial layer delamination during the wet etch and yield a larger bonded area.

We developed several different wafer bonding processes for dissimilar silicon-based wafers. Optical microscope photographs of wafer bonded layers after HCl etching of the native InP substrate are shown in Figure 2.1: (1) InGaAsP-on-Si (Fig. 2.1, b); (2) InGaAsP-SiO_2-on-Si (Fig. 2.1, c); (3) InGaAsP-on-SOI (Fig. 2.1, d). While we sucessfully bonded epitaxial InGaAsP to all three types of Si-based wafers (SiO_2-on-Si, SOI and bare Si), the success rate was largely disparate. For instance, bonding to a SiO_2-on-Si (we had a 6 µm thick thermal oxide layer) worked with good consitancy and repeatability, while bonding to bare Si failed most of the time. For SOI, we found that etching vertical outgassing channels (VOCs) in the top silicon layer is extremely beneficial for the bonding process success rate. A good example of nearly full epitaxial InGaAsP layer transfer from a $\frac{1}{4}$ of a 2-inch InP wafer to a SOI wafer is presented in Figure 2.1, e. The likely reason behind the frequent wafer bonding failures is a lack of control over the microscopic particle contamination during the manual wafer handling during the surface preparation. Possibly, having the "softer" SiO_2 as one of the bonding surfaces or VOC network for SOI helps to elevate the surface flatness tolerance.

We optically tested the wafer bonded layers using a setup described further in this chapter (Section 2.2). The characterization results show a red shift and a $4\times$ drop in photoluminescence (PL) intensity in bonded InGaAsP/SiO_2-on-Si samples compared to the unbonded InGaAsP/InP [77]. The measurement suggests that wafer bonding process introduces some damage to the InGaAsP epitaxial layer, and possibly, stress from the lattice mismatch and thermal expansion coefficient difference in InGaAsP and Si-based materials.

2.1.2 Ebeam writing

The electron-beam (ebeam) patterning process should always be optimized, since a properly exposed mask is less susceptible to erosion and provides the best ge-

ometrical conformity to the design. We used negative tone hydrogen silsesquioxane (HSQ) ebeam resist by the in fabrication of all devices described herein. This resist offers very high resolution with minimum defined feature size below $\approx 10\,\text{nm}$ [74]. The key advantages of HSQ include high thermal stability and compatibility with CMOS. Because HSQ monomers cross-link into a silicon based polymer with glass-like properties under extreme ultraviolet (EUV) radiation and ebeam exposure, it can work as a ''spin-on" dielectric and stay as part of the device/circuit [78]. Another potential application for HSQ is a thermal oxidation masking [79] with high resolution and a moderate sensitivity.

We used two different formulations of HSQ: flowable oxide FOx-16 (16 % of HSQ in methyl isobutylketone (MIBK)) and flowable oxide FOx-13 (1 % of HSQ in MIBK) by Dow Corning. The wafers were spun-coated with an $\approx 250\,\text{nm}$ thick layer. If undiluted, FOx-13 should be spun at 3000 rpm to yield an HSQ layer close to the target thickness. To spin the FOx-16 formulation to the same thickness, we diluted it in MIBK 1:1 by volume and spun the resultant solution on the samples at 2000 rpm. Next step for both of these formulations is a softbake on a hotplate at 100 °C for 5 min.

To estimate the target range of area exposure doses based on the set beam spot size s and probe current I, we applied the following formula:

$$A = \frac{I \cdot t}{s^2} \tag{2.1}$$

We chose the values of $I = 100\,\text{pA}$ and s=5 nm because they provide a sufficient area exposure dose at reasonable writing time ($\approx$ 5-15 minutes). A finer step and/or lower current may require longer dwell time, and as a result, a longer pattern exposure time. The downside of a long exposure time is the electron beam susceptibility to drift over time, which in tern leads to pattern distortion.

Ebeam lithography was performed on Raith50 ebeam writer with the following settings: energy - 30 keV, probe current - 100 pA, write field - 100 µm. We developed the exposed HSQ resist in 25 % tetramethylammonium hydroxide (TMAH) for 30 seconds with agitation, followed by a isopropyl alcohol (IPA) or DI water rinse and nitrogen gun blow-dry as a final step.

Figure 2.2 depicts the results of an exposure dose test for HSQ masks

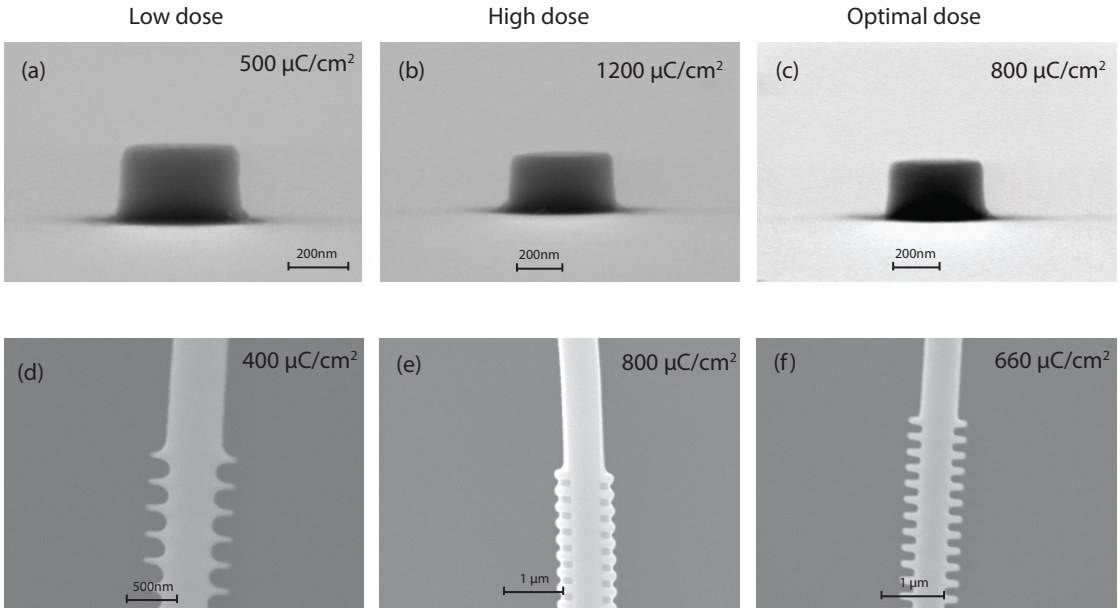

Figure 2.2: Various exposure doses and their effect on resist mask quality: (a-c) FOx-13 mask formed under low, high and optimal exposure conditions; (d-f) diluted FOx-16 mask formed under low, high and optimal exposure conditions.

(FOx-13 and FOx-16 formulations). The top row corresponds to the patterns for nanolasers. Their mask geometry is very simple (circular). This simplicity allows a fairly large tolerance in exposure dose without introducing distorted proportions. The optimal exposure dose window is between 500 and 800 $\mu C/cm^2$ for nanolaser ebeam patterns. However, for more complex structures with small features, such as the grating for a DFB laser in Fig 2.2 (d-f), the optimal exposure dose window narrows down to 600-700 $\mu C/cm^2$.

2.1.3 Reactive ion etch

We performed RIE processes on three different materials: InGaAsP/InP, SiO_2 and Si. Standard RIE recipes rendered good results for SiO_2 and Si materials: CHF_3/O_2 chemistry (Oxford P80 RIE tool) for $SiO_2$and SF_6/O_2 in (Oxford P100 RIE tool) for Si. These processes will be described in Chapters 4 and 7. However, etching of InGaAsP/InP required careful development and optimization for sufficiently vertical and smooth device sidewalls. We explored three different etching chemistries finally obtaining the best results with the Trion RIE tool:

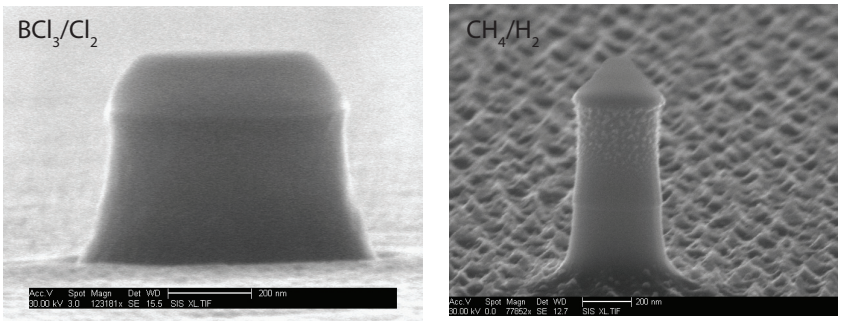

Figure 2.3: SEM images of InGaAsP/InP pillars obtained with (a) etching in BCl_3/Cl_2; (b) etching in CH_4/H_2.

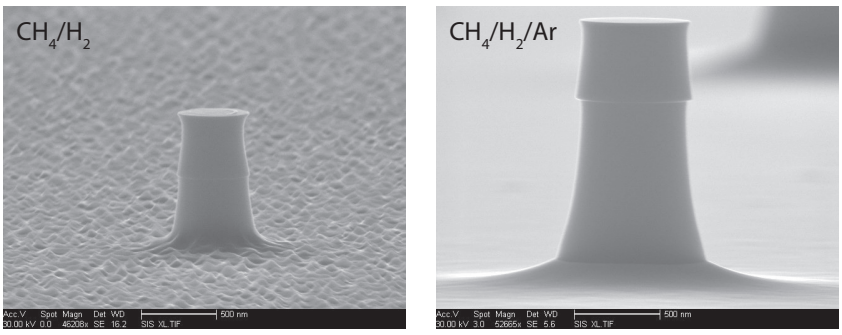

Figure 2.4: SEM images of InGaAsP/InP pillar after etching in (a) CH_4/H_2 (b) $CH_4/H_2/Ar$.

– First, we tried a chlorine-based chemistry, BCl_3/Cl_2, since it typically employed for etching GaAs-based III-V compounds [80]. The etching rate is fast and produces fairly smooth sidewalls in materials such as GaAs, AlGaAs or GaP. This chemistry is uniquely suitable for Ga-containing materials, since the Ga by-products of this process are volatile. However, $InCl_3$, the by-product of indium, is a solid at room temperature. It tends to sediment on the etched surface and severely impede the further process rate, resulting in the sloped sidewalls (Figure 2.3, a).

– Second, we tested CH_4/H_2 dry etch chemistry. In this case, the constituent InGaAsP elements form only volatile by-products: $Ga(CH_3)$, $In(CH_3)$, AsH_3 and PH_3. A major downside of this chemistry is hydrocarbon film formation on the etched surface and the reactor sidewalls. Chamber conditioning, i.e. an empty chamber run, prior to the process for at least 20 min is required

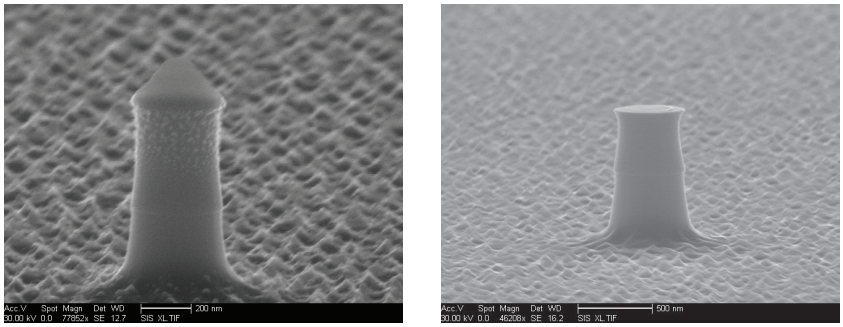

Figure 2.5: SEM images of etched InGaAsP pillar in $CH_4/H_2/Ar$ chemistry (a) with polymer on the sidewalls; (b) after cleaning in O_2 plasma and BOE.

for this process to work. According to a study by Heyes et al [81], the ratio between CH_4 and H_2 gases in the mixture is particularly important for the etch rate repeatability and anisotropy. The authors found the CH_4 content below 25 % allows to keep the polymer growth rate relatively low, thus keeping the etching process undeterred. We fixed CH_4/H_2 ratio at 4:40 sccm, i.e. 10 % to ensure reasonable control over the etching depth with etching rate of 60-80nm/min. The low density plasma is preferential when surface morphology is important and high etch rates are not necessary, and in our case even undesirable. Since our priorities include well controlled etching rate and smooth surface, we run the RIE process without adding the inductively coupled plasma (ICP) component [82]. An SEM image of an etched InGaAsP/InP pillar using CH_4/H_2 gas mixture is shown in Figure 2.3, b. The difference in sidewall slope compared to the BCl_3/Cl_2 (Figure 2.3, a) is easily observed.

– Finally, we optimized the previously developed CH_4/H_2 etching chemistry by adding Ar into the gas mixture and tuning its flow rate. The by-product compounds $Ga(CH_3)$ and $In(CH_3)$ of CH_4/H_2 etch are known to be less volatile than AsH_3 and PH_3. This leads to the preferential loss of As and P elements in InGaAsP and InP semiconductors. Argon dilution helps to ionize and dissociate CH_4 gas molecules, stabilize plasma discharge, activate the etched surface through Ar^+ ion bombardment and sputter non-volatile etch products [83]. This translates into higher vertical etching rate (i.e., steeper

sidewalls) and smoother surface by limiting redeposition of polymer and prevention of micromasking. The result of this RIE process compared to the CH_4/H_2 without Ar is depicted in (Figure 2.4 a,b). Note that these images were taken after the HSQ mask was removed for a clearer presentation.

The final conditions of our optimized $CH_4/H_2/Ar$ reactive ion etch are the following: Trion RIE reactor pressure was kept at 30 mTorr, RF power was 150 W, gas flows were set for $CH_4/H_2/Ar$ are 4:40:20 sccm.

We developed a specific post-RIE cleaning process to remove the HSQ mask and polymer deposited during RIE. First, we carried out a 10-40 minutes microwave O_2 plasma clean in Tepla100 or a brief 10 minute RF plasma clean in Trion RIE tool with a reduced O_2 flow of 30 sccm. Second, we removed the HSQ resist mask in 6 % buffered oxide etch (BOE) by agitating the samples in it for 30-60 seconds. We complete the process with a thorough deionized(DI) water rinse and N_2 gun blow-dry. SEM images of etched samples before and after the post-etching cleaning are presented in Figure 2.5 a, b.

2.1.4 PECVD of thin SiO_2 layers

Plasma enhanced chemical vapor deposition of silicon dioxide yields a high quality conformal layer of oxide. A typical PECVD can be qualitatively expressed by the chemical formula:

$SiH_4 + N_2O \longrightarrow SiO_2 + NH_3 + N_2$

At first we used the basic Oxford Instruments SiO_2 deposition process for the Oxford Plasmalab PECVD tool:

- 5% SiH_4/95%N_2 flow: 170 sccm
- N_2O flow: 710 sccm
- Pressure - 1000 mT
- R. F. power - 20 W at 13.56 MHz
- Temperature - 350 $^\circ C$

– Deposition rate 50-70 nm/min

The resultant SiO_2 layers are rough due to the trapped bubbles (2.6, a) of gas which fail to outgas during the deposition. Slowing the PECVD process down helps to accelerate gas desorption and deposit a smoother SiO_2 layer 2.6, b). We kept the N_2O:SiH_4 gas ratio the same, as well as the rest of the parameters, but reduced the gas flow rates to 177.5 sccm for $N_2O$and 42.5 sccm for SiH_4. We measured the deposition rate to be ≈15-20 nm per minute.

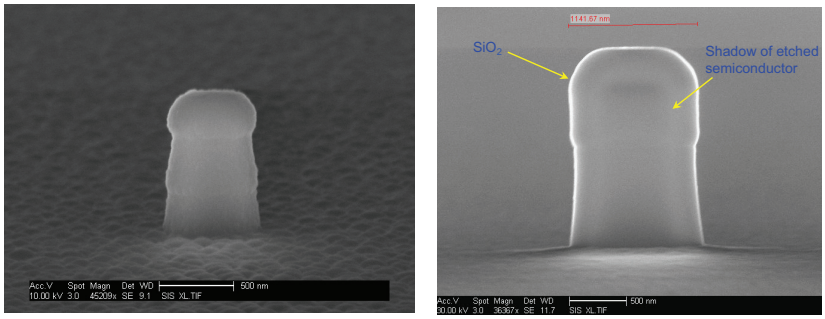

Figure 2.6: Silicon dioxide shield optimization. Presented are the SEM images of a pillar with SiO_2 shield deposited with the (a) standard Oxford Plasmalab PECVD tool recipe; (b) optimized PECVD recipe.

2.2 Optical characterization of small lasers

To optically charactere our samples, as discussed in Chapters 3, 4, and 7, as well as in Appendix A, we designed and built micro photoluminescence (micro-PL) setups in various configurations. Here we will describe the first micro-PL setup in a very condensed manner, since it is discussed in detail elsewhere [77]. The original version of the setup was designed to test optical behavior of metalo-dielectric nanolasers, emitting perpendicularly and vertically with respect to the wafer plane, as well as a Fabri-Perot laser with distributed Bragg reflector (DBR) mirrors (Appendix A). In order to systematically measure an optical response of the in plane-emitting distributed feedback (DFB) laser (Chapter 7), we changed the setup layout and added additional high spectral resolution measurement capabilities. Finally, we designed and built another setup for transmission measurements

in waveguides with gain (hybrid Si/III-V waveguides).

2.2.1 Micro-PL photoluminecence setup for vertical emitting lasers

The original micro-PL optical setup [77] was designed specifically for detection and analysis of very low optical signals, such as emitted by a nanolaser. The setup is schematically depicted in Figure 2.7. It operates in a reflection mode, i. e. the samples were optically pumped and probed from the same direction **??**. For a visual reference, the sample can be imaged on a InGaAs CCD camera (Indigo Alpha) with resolution of 252×316 pixels and 30 µm pixel size, using 1,550 nm illumination source and two cascaded 4-f systems. We optically injected the samples with a 1,064nm pulsed fiber laser (SPI G3 with maximum power of 12 W). The laser was set to operate at 12 ns pulse width and 300 kHz repetition rate to achieve sufficiently high peak powers for population inversion to occur, while keeping the average power low enough to avoid adverse thermal effects.

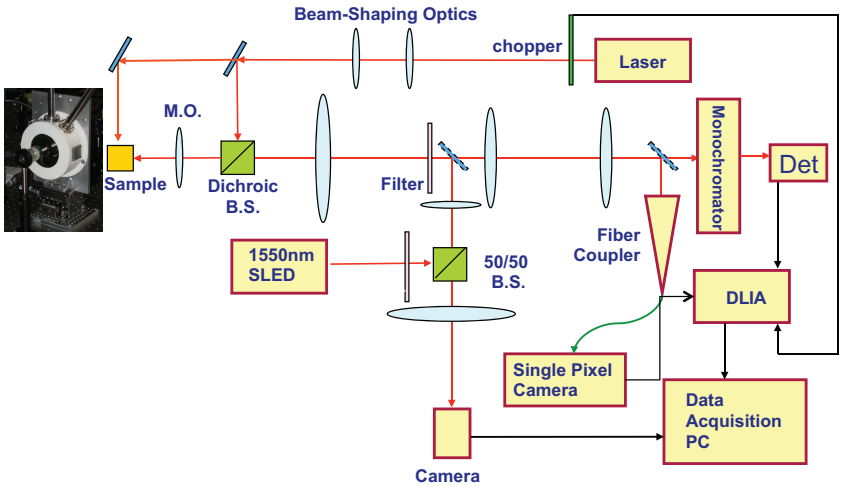

Figure 2.7: Micro-PL optical characterization setup. Reprinted from [77].

The pump beam passes through a dichroic beam splitter and focuses down on the sample to a spot size of 8×8 µm^2 size with 20× microscope objective (Mitutoyo NIR ×20). A telescope (lenses L7 and L8 in Figure 2.7) is built into the setup

to fight chromatic aberration from the dissimilar pump and signal wavelengths (1,064 nm and ≈1,550 nm, respectively). The high-pass edge filter (Semrock RazorEdge) is incorporated between the sample and the detection system of the setup to remove the reflected pump. The detection part of the setup: monochromator (CVI Digikrom DK480) with 70 pm resolution limit, InGaAs fixed-grating spectrometer (Ocean Optics) 3 nm resolution limit and cooled InGaAs single pixel detector.

To improve the signal-to-noise ratio of the setup we used a digital lock-in amplifier (Stanford Research System SR830) in conjunction with a mechanical chopper (Stanford Research System SR540) set at 1 kHz as the source of modulation we lock to. This configuration enables us to detect and spectrally characterize sub picoWatt signals from the nanoscale lasers.

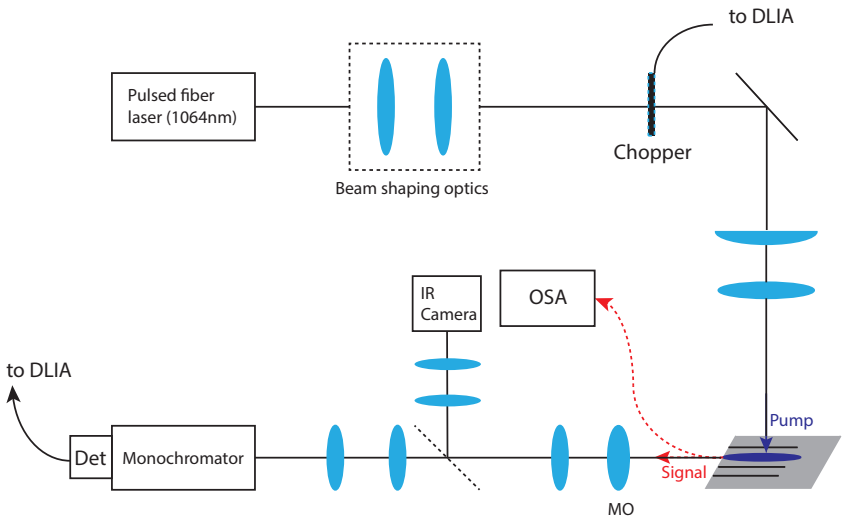

Figure 2.8: Schematics of an optical characterization setup for edge emitting lasers.

2.2.2 Micro PL optical setup for edge emitting device characterization

In order to characterize the optically pumped lasers emitting in the substrate plane, we changed the layout of the micro PL setup described above. The modified configuration allowed us to pump samples from the top (normal to the

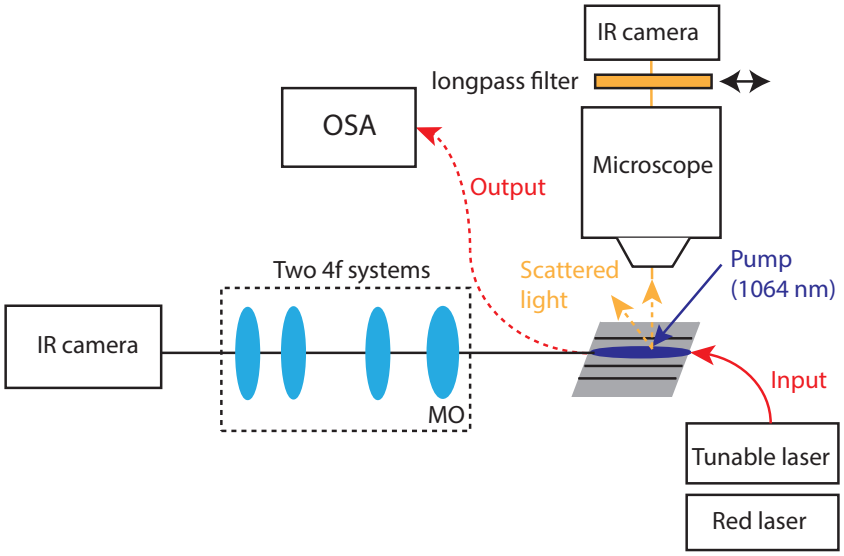

Figure 2.9: Schematics of an optical characterization setup for transmission measurements in waveguides with gain.

substrate plane) with an elliptically shaped beam spot and collect the signal at the edge of the wafer (Figure 2.8). While the signal detection scheme remained the same, the pumping arrangement had to be modified to accommodate the device geometry. First, we implemented a combination of a cylindrical (f=500 mm, Thorlabs AR coated singlet lens) and a spherical (f=5 mm, Thorlabs AR coated achromatic doublet) to form elliptical beam waist to cover the DFB laser area (see setup description in Chapter 7). We supplemented the setup with an optical spectrum analyzer (OSA) ANDO 6317B with a resolution limit of 0.05 nm in near IR for narrow DFB laser linewidth measurements (Appendix F). Since the setup only accepted a single mode fiber input, we collected the signal with a tapered fiber and passed it through a U-bench with a 1,064 nm long pass filter. We found that pump beam/sample/tapered fiber alignment is best done according to the following procedure:

- For the rough alignment, we imaged the sample plane on a microscope and adjusted its position on a mechanical XYZ stage (Newport) with respect to a green alignment laser, collinear with the 1,064 nm pump beam.

- Next, we improve alignment precision by switching to the IR camera imaging

of the microscope field of view. We filter out the scattered 1,064 nm light with a long-pass filter and visually maximize the PL signal from the sample by adjusting the pump beam position.

– Next, we visually align the tapered single mode fiber, mounted on an XYZ-stage (mechanical and piezo), and a sample using a red alignment laser and an upright long working distance microscope.

– We set the signal of interest on the OSA close to the peak wavelength of the sample and adjust the 1,064 nm pump beam until the OSA detects a signal from the sample.

– Finally, we perform fine adjustments to the 1,064 nm beam position with respect to the sample and fiber position using Physics Instrumente piezostage and E-463 HVPZT Piezo Amplifier to maximize the signal detected by the OSA.

2.2.3 Micro PL optical setup for transmission measurements in III-V/Si waveguides

A transmission measurement setup with the capability of optical pumping of gain materials is illustrated in Figure 2.9. The light is coupled from a tunable laser into straight waveguides containing the Bragg grating structures, the output signal is collected from the other end of the waveguide, and sent to an Agilent Optical Spectrum Analyzer with a maximum resolution of 0.01 nm (or 0.1 pm, when used in heterodyne detection configuration). Scattered pump light is filtered out using a series of two 1,100 nm long-pass filters in a fiber U-bench between the collection lens-tipped fiber and the spectrometer. By tuning the wavelength of the input signal, we can probe the transmission response of the entire system. The coupling coefficient depends on material gain/loss; this we control by optically pumping the entire waveguide from above using 1,064 nm pulsed or CW laser illumination with SPI Yb GTWave fiber laser (redEnergy G4) with maximum average power of 20 W). We use an infrared CCD camera (FLIR) with a series of two 1,100 nm

long-pass filters to align the elliptical pump beam with the samples. The beam aspect ratio can be adjusted via two orthogonally oriented cylindrical lenses. Due to the high resolution limit of the optical analyzer, this setup is also well suited for high resolution spectral measurements.

Chapter 3

Room-temperature sub-wavelength metallo-dielectric lasers

3.1 Introduction

Achieving the most compact footprint for photonic components is an important factor in the design of integrated optical devices. Like most other photonic components, the minimum size for a laser is ultimately governed by λ_0, the free-space wavelength. For example, as the size of a conventional Fabry-Pérot semiconductor laser is scaled down in all three dimensions towards λ_0, three effects adversely influence the lasing process. First, the round trip path of the optical wave in the gain medium is shortened. Second, radiative losses from the end mirrors are increased. Third, the lateral field confinement in the resonator waveguide is reduced, resulting in less overlap of the optical mode with the gain medium. All these effects serve to increase the lasing threshold, and lasing cannot therefore be achieved below a certain size limit. By allowing the laser size to increase in one or two dimensions, it is possible to reduce the physical size of the laser in the remaining dimension(s) to values below this limit. For example, the disk thickness in whispering-gallery-mode (WGM) lasers [84] can be reduced to a fraction of the free-space wavelength [85], but to compensate for this thickness reduction the disk diameter should be increased accordingly. The ultimate challenge in this respect

is concurrent reduction of the resonator size in all three dimensions, while still satisfying the requirements for lasing action.

The size of an optical cavity can be defined using different metrics (for example, the physical dimensions of the cavity or the size of the optical mode). However, if the goal of size reduction is to increase the integration density (for example, in a laser array), the effective cavity size should account for both the overall physical dimensions of the resonator and the spread of the optical mode beyond the physical boundary of the resonator. By this token, most conventional dielectric laser cavities are not amenable to dense integration because they either have a large physical footprint or a large effective mode. For example, distributed Bragg resonators [86] and photonic-crystal cavities [87] (both of which can be designed to have very small mode volumes) have physical footprints that are many wavelengths in size, due to the several Bragg layers or lattice periods that are required for maintaining high finesse. On the other hand, it has been demonstrated that the diameter of thick (λ_0/n) micro-disk lasers can be reduced below their free-space emission wavelength [88]; however, the spatial spread of the resultant modes (which have low azimuthal numbers owing to the small disk diameters) into the surrounding space beyond the physical boundaries of the disks may lead to mode coupling and formation of "photonic molecules" in closely spaced disks [89]. To illustrate the case, the $M = 4$ WGM for a semiconductor disk with radius $r_c = 460\,\text{nm}$ and height $h_c = 480\,\text{nm}$ (Figure 3.1a) is shown in Figure 3.1b, clearly indicating the radiative nature of the mode and its spatial spread, which, as mentioned, can lead to mode coupling with nearby structures.

3.2 Design

One approach for alleviating these issues is to incorporate metals into the structure of dielectric cavities, because metals can suppress leaky optical modes and effectively isolate them from their neighboring environment. The modes in these metallo-dielectric cavities can be grouped into two main categories: (i) surface bound (that is, surface plasmon polariton (SPP)) resonant modes and (ii)

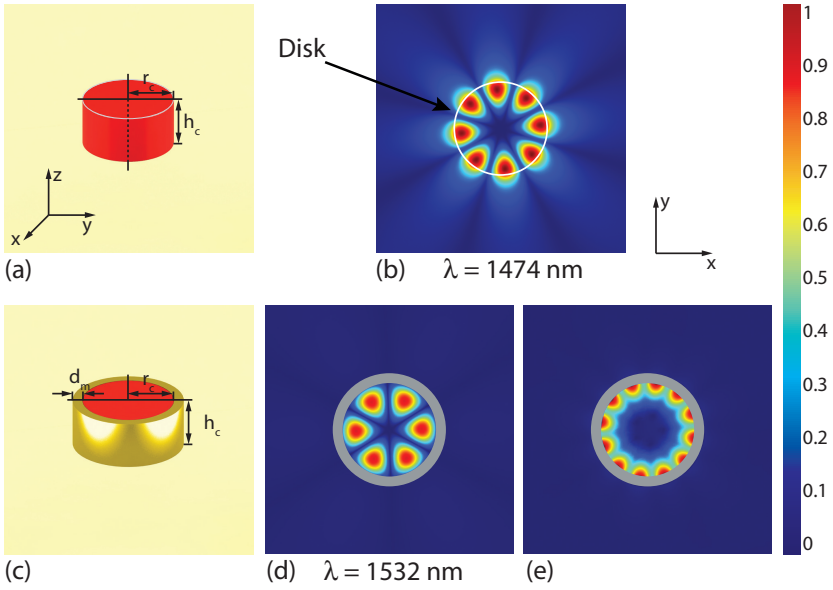

Figure 3.1: **(a)** A thick semiconductor disk ($r_c = 460\,\text{nm}$, $h_c = 480\,\text{nm}$, $n_{semi} = 3.4$) and its $M = 4$ whispering-gallery resonance **(b)** are shown. Note the spatial spread of the mode compared to the actual disk size. **(c – e)** The same disk encased in an optically thick ($d_m = 100\,\text{nm}$) gold shield **(c)** will have well-confined reflective **(d)** and plasmonic **(e)** modes, but with much higher mode losses. |E| is shown in all cases, and the section plane is horizontal and through the middle of the cylinder.

conventional resonant modes, resulting purely from reflections within the metal cavity. Although they are highly confined, the disadvantage of plasmonic modes is their high loss, which is caused by the relatively large mode overlap of the optical field with the metal (compared to the reflective case). Owing to the high Joule loss at telecommunication and visible wavelengths, the lasing gain threshold for such cavities can be very large. On the other hand, the negative permittivity of metals not only allows them to support SPP modes, but also enables them to act as efficient mirrors. This leads to the second class of metallo-dielectric cavity modes, which can be viewed as lossy approximations of the modes in a perfectly conducting metal cavity. Because the mode volume overlap with the metal is usually smaller than in the plasmonic case, in this type of cavity it is possible to achieve higher Q factors and lower lasing gain thresholds, albeit at the expense of reduced mode confinement (compared to plasmonic modes). In general, both types

of mode can exist in a real metal cavity. Embedding the aforementioned gain disk in a gold shield (Figure 3.1c) effectively confines the resonant modes while increasing Joule losses. As discussed, the surface-bound plasmonic mode (Figure 3.1e) has both a higher M number and higher losses (M = 6, Q = 36) compared to the non-plasmonic mode (Figure 3.1d, M = 3, Q = 183).

It should be noted that even though the metal shield is the source of Joule loss, the large refractive index of the semiconductor core ($n_{semi} \approx 3.4$) aggravates the problem and increases both the plasmonic and Fresnel reflection losses. For SPP propagation on a (planar) semiconductor–metal interface, the threshold gain for lossless propagation is proportional to n_{semi}^3 [90]. This means that, even though high-Q plasmonic modes can exist inside metal cavities with low-index cores (for example, silica, $n = 1.48$ [91]), using this approach to create a purely plasmonic, room-temperature semiconductor laser at telecommunication wavelengths will be very challenging, due to the order-of-magnitude increase in gain threshold.

One solution for overcoming the metal loss obstacle is to reduce the temperature of operation. This will have two coinciding benefits, a reduction of the Joule losses in the metal and an increase in the amount of achievable semiconductor gain. Recently Hill and colleagues [92] have demonstrated cryogenic lasing from gold-coated semiconductor cores with diameters as small as 210 nm. However, in this case the metal is directly deposited on the semiconductor core (with a 10 nm SiN insulation layer between; Figure 3.2a, left). As a result, owing to the large overlap of the mode with the metal, the estimated room-temperature cavity Q is quite low. The best case is ~ 180 for a silver coating (assuming the best reported value for the permittivity of silver [93]). This corresponds to an overall gain threshold of $\sim 1{,}700\,\mathrm{cm}^{-1}$ and is quite challenging to achieve at room temperature. Even though this device lases when cooled to cryogenic temperatures, it would be challenging to achieve room-temperature lasing with the same approach and a similarly sized cavity, due to the constraints imposed by the amount of available semiconductor gain and metal losses. The gain coefficient reported for optically pumped bulk InGaAsP emitting at 1.55 µm is reported to be $\sim 200\,\mathrm{cm}^{-1}$ [94]. Electrically pumped multiple quantum wells (MQWs), on the other hand, have been reported

to have higher material gain coefficients of over 1,000 cm^{-1} [?]. Also, recent results obtained from Fabry-Pérot-type metallic nanolasers at room temperature indicate that this level of gain is also achievable from bulk InGaAs [95]. However, even if the required gain is achievable at room temperature, efficient operation of the device would still be a challenge due to thermal heating and non-radiative recombination processes (for example, Auger recombination). In particular, to operate a densely packed array of such devices, thermal management would be a major concern, given the requisite intense pumping levels. Consequently, it is extremely important to optimize the cavity design so that the gain threshold is minimized.

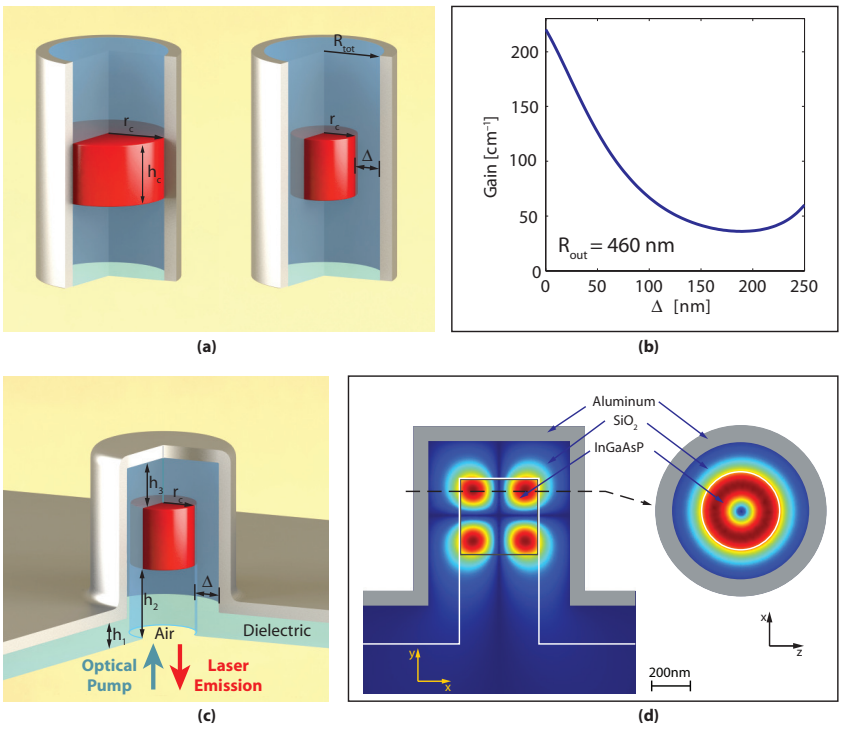

Figure 3.2: **(a)** Metal-coated gain disk with vertical confinement provided by low-index waveguide cutoff sections (left panel) as demonstrated by Hill and colleagues [92]. Same structure, but including a dielectric shield layer of thickness Δ (right panel). **(b)** Variation of gain threshold of the composite gain/dielectric/metal waveguide as the dielectric shield thickness Δ is changed, assuming a fixed total radius $R_{tot} = 460$ nm [20]. **(c)** Practical realization of the laser cavity for compatibility with planar fabrication techniques. The air gap at the bottom of the laser is formed after a selective etch of the InP substrate. **(d)** Cross-sections of |E| for the TE_{012} mode of the cavity. In the designed cavity the values for h_1, h_2 and h_3 are 200, 550 and 250 nm, respectively.

3.3 Design and Simulation

Previously, we have predicted that by incorporating a dielectric shield layer between the metal and the semiconductor (Figure 3.2a, right) and optimizing the dielectric thickness, the gain threshold of the laser can be substantially reduced so that it is amenable to operation at room temperature [20]. The benefit stems from the tendency of the low-index shield to push the electromagnetic mode towards the high-index inner core and away from the metal walls, reducing the mode–metal overlap and hence the Joule loss. Excessive shield thickness can be detrimental, because the shield uses up space within the device that would otherwise be filled with the gain. For a fixed total waveguide radius R_{tot} and for each waveguide mode, an optimal shield thickness Δ (with the corresponding gain core radius $r_c = R_{tot} - \Delta$) exists that minimizes the threshold gain [20]. This is illustrated in Figure 3.2b for the TE_{01} mode and $R_{tot} = 460\,\text{nm}$ (the same device footprint as in Figure 3.1), using silica ($n = 1.46$) as the shield layer. It can be seen that the optimally sized shield ($\Delta \approx 200\,\text{nm}$) reduces the gain requirement several fold relative to a metal-clad device of equal diameter but without the shield ($\Delta = 0$). Furthermore, one can ensure, by proper design, that the mode of interest is in cutoff in the upper and lower sections of the waveguide, where the core is only composed of dielectric with no high-index core (Figure 3.2a). When this is the case, the structure acts as a three-dimensional optical resonator [20].

The conceptual diagram in Figure 3.2a implies that the upper and lower waveguide sections, where the mode is in cutoff, extend to infinity. In practice, we truncate the guide some distance above and below the gain section Figure 3.2c, far enough so that the energy leakage resulting from this truncation is minor. The light escaping from the lower section is used as the laser output, and the upper section is capped with metal for unidirectional emission and fabrication process compatibility. Also, owing to a selective etch step in our fabrication process, the lower cutoff section ends up comprising a composite core with an air column directly underlying the gain block (instead of a solid silica core). This does not compromise the performance of the resonator; in fact, it makes the cutoff in the lower section more severe. Figure Figure 3.2d shows two cross-sections of |E| for

the TE_{012} mode of the resonator in Figure Figure 3.2c.

The resulting room-temperature Q of this cavity is $\sim$ 1,030 (assuming gold, $\epsilon = -95.9 - 11i$ [96], for the metal shield), with a resonance at 1.55 µm and a gain threshold of only 130 cm^{-1}. Note that both the physical size and modal size of this cavity are smaller than the wavelength of emission. Assuming a minimum metal shield thickness of 70 nm (which is twice the skin depth), the diameter and height of this laser are 1.1 and 1.35 µm, respectively. Also, in addition to having a low gain threshold, the laser is optically isolated from any structure placed next to it.

3.4 Fabrication

The shielded laser structure was fabricated from an InGaAsP MQW gain layer grown on InP. Hydrogen silsesquioxane (HSQ) electron-beam resist was patterned into arrays of dots (Figure 3.3a) using a Raith 50 electron-beam writer, and the size of the dots was varied by changing the pattern size and/or the electron-beam dosage. Cylindrical structures were then etched using $CH_4/H_2/Ar$ reactive ion etching (RIE) (Figure 3.3b). Using an optimized and calibrated plasma-enhanced chemical vapor deposition (PECVD) process, the silica shield layer was grown to a thickness of $\sim$ 200 nm (Figure 3.3c). Note that the outline of the embedded gain core is visible through the silica layer. In practice, the low adhesion of gold to silica caused separation of the dielectric portion of the structure from the metal layer. Fortunately, aluminium exhibits has better adhesion properties, and at the wavelength of interest its optical properties are very close to gold.[1] A layer of aluminum with a minimal thickness of 70 nm was sputtered over the silica-covered pillars (Figure 3.3d). The sample was then bonded on the upper side to a glass slide using SU-8, and the InP substrate was subsequently removed in a selective HCl etch, leaving an air void under the structure. Figure 3.3e shows the tilted bottom view of an air void, with the lower face of the gain core visible inside. Figure 3.3f shows the normal bottom view (with enhanced contrast levels) of a similar void. The faint outline of the silica shield is discernible in this image,

[1] The cavity Q of the resonator with an aluminum coating ($\epsilon = -238.5 + 44.7i$ [96]) is 1,004, which compares with 1,030 for gold.

verifying the 200 nm thickness of the shield. (Further details of the fabrication process are presented in the Section **??**.)

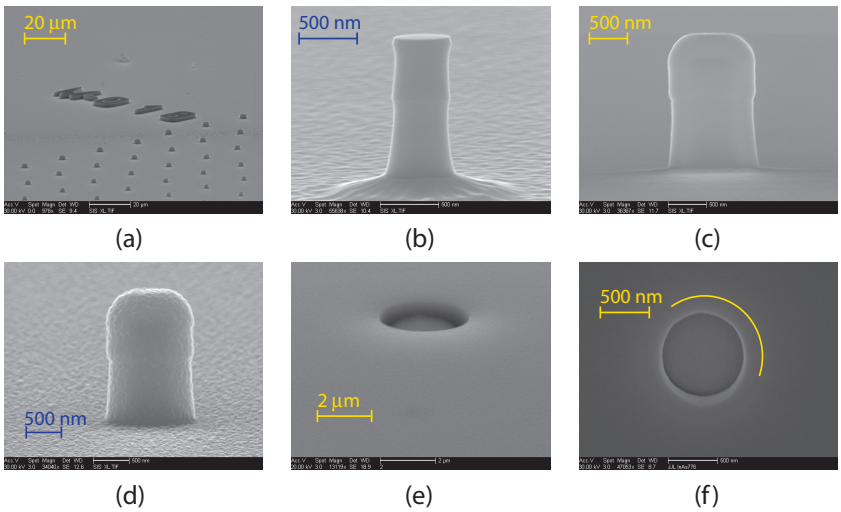

Figure 3.3: **(a)** Array of electron-beam patterned HSQ resist dots. **(b)** RIE etched pillar after oxygen plasma and buffered oxide etch cleaning. The faint bump in the middle indicates the boundary between the InGaAsP and InP layers. **(c)** Etched pillar after PECVD of silica. The outline of the semiconductor pillar can be seen through the silica layer. **(d)** Silica-covered pillar after undergoing aluminium sputtering (70nm). **(e)** Tilted bottom view of one of the samples after a selective InP etch with HCl. The surface is composed of PECVD deposited silica. The hole corresponds to the air hole shown in the diagram of Figure 3.2d. **(f)** Contrast-enhanced normal bottom view of a cavity. The circular outline around the air hole is due to the dielectric shield and agrees well with the target dielectric shield thickness of 200 nm.

3.5 Characterization

For optical pumping we used a 1,064 nm pulsed fibre laser operating at a repetition rate of 300 kHz and a pulse width of 12 ns. The pump beam was delivered to the samples using a ×20 or ×50 long-working-distance objective, which also collected the emitted light. To estimate the amount of pump power absorbed by the core, a full three-dimensional finite-element analysis was carried out over a range of core sizes (see Appendix B for details of calculations). Using a double 4–f imaging system in conjunction with a pump filter (Semrock RazorEdge long wavelength

pass), the samples were imaged onto either an IR InGaAs camera (Indigo Alpha NIR) or a monochromator (Spectral Products DK480) with a resolution of 0.35 nm and equipped with a cooled InGaAs detector in a lock-in detection configuration. Owing to the electron-beam writing process, the samples were slightly elliptical. The major and minor diameters of the gain core for the particular sample under test were measured to be 490 and 420 nm, respectively.

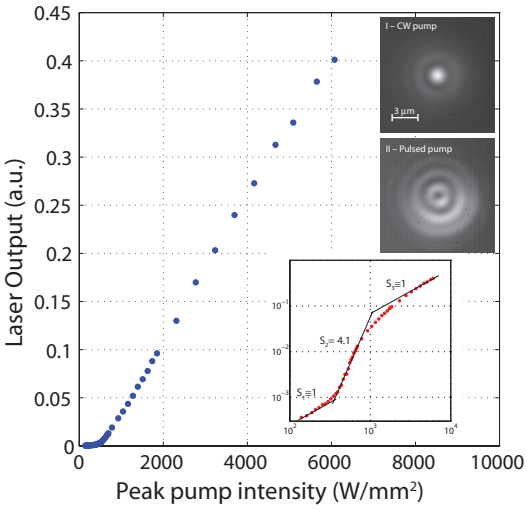

Figure 3.4: Light–light curve for a nanolaser with major and minor core diameters of 490 nm and 420 nm (blue dots), respectively. The same data set is shown as a log–log plot (bottom inset, red symbols) together with the slopes for the PL, ASE and lasing regions. Also shown are the images of the defocused emitted beam cross-section (taken $\sim$ 10 µm away from the nanolaser exit aperture) for (I) c.w. pumping and (II) pulsed pumping. The appearance of the higher-contrast fringes indicates increased coherence due to lasing.

In Figure 3.4 the light–light curve corresponding to a laser emitting at 1,430 nm is presented (blue symbols), which shows a slope change indicating the onset of lasing at an external threshold pump intensity of $\sim$ 700 W/mm^2. The same data set is shown in a log–log plot (Figure 3.4, red inset graph), with the slopes of different regions of operation indicated on the plot. The S-shaped curve clearly shows the transition from photoluminescence (PL) to amplified spontaneous emission (ASE) and finally into the lasing regime. Also shown in Figure 3.4 are the emission patterns of the defocused laser image captured with the IR camera, cor-

responding to continuous-wave (3.4, inset (I)) and pulsed (3.4, inset (II)) pumping situations. The average pump intensity in each case was approximately equal to $8\,\mathrm{W/mm^2}$. In the c.w. case, only broad PL emission occurs, owing to the low peak intensity. However, when the pump is switched to pulsed mode, lasing is achieved due to the 278-fold increase in peak power. At the same time, the defocused image forms a distinct spatial mode with increased fringe contrast, which is an indication of increased spatial coherence and is further evidence of lasing. The polarization of the emission has a strong linear component, which is due to the slight ellipticity of the gain core (see Appendix E for more details).

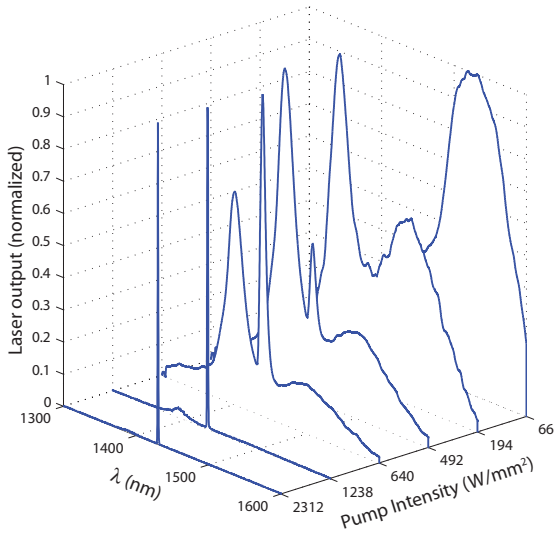

Figure 3.5: Evolution of the emission spectra from PL over ASE to lasing.

Figure 3.5 shows the evolution of the emission, from a broad PL spectrum to a pair of competing ASE peaks and finally into a narrow lasing line at 1,430 nm. The measured linewidth of this particular laser was 0.9 nm; however linewidths as small as 0.5 nm were measured for other samples in the same size range.

Another way to verify the soundness and accuracy of the design and fabrication processes is to match the lasing wavelength with the target resonance of the cavity. However, owing to the high pump intensity, the refractive index of the gain core can vary substantially from its quiescent value and this can considerably shift the lasing line from its target wavelength. Using the measured results from an

array of lasers with slightly different sizes (which were measured individually using a scanning electron microscope, SEM) and exact three-dimensional finite-element modelling of each of the gain cores, the refractive index of the gain medium under pumping conditions was estimated at each lasing point (Figure 3.6, green symbols and error bars).

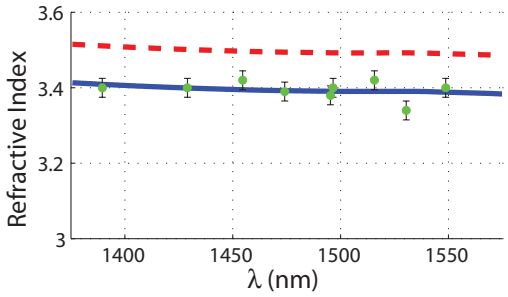

Figure 3.6: Effective refractive indices (green symbols) of the pumped MQW gain medium at lasing wavelengths, back-calculated from lasing spectra obtained from an array of nanolasers. Error bars were calculated assuming $\pm 5\,\mathrm{nm}$ error in measuring the disk diameters from the SEM images. The dashed red curve shows the effective refractive index of the unpumped MQW layer, as measured by a Filmetrics interferometric analyzer. The blue curve is offset from the red by a constant amount (0.102 RIU), which was chosen for best fit to the lasing data. The index reduction is consistent with the estimated free-carrier effects.

Assuming a uniform drop over the spectrum of interest and using a least-squares fit of these data points, the estimated refractive index drop is ~ 0.102 refractive index units (RIU) (least-squares fit) lower than that reported by interferometric multilayer measurements of the unpatterned wafers under low illumination intensity (Figure 3.6, red dashed line). We attribute this shift to be mainly due to free carrier effects (a combination of bandfilling, bandgap shrinkage and free carrier absorption), for which the net effect at the estimated carrier density ($\sim 1.2 \times 10^{19}\,\mathrm{cm}^{-3}$ for a 520 nm diameter core) is expected to cause a refractive index drop of $\sim 0.1\,\mathrm{RIU}$ [97] (see Appendix B for details of carrier density estimation). Also, a slight additional contribution (at most $-0.004\,\mathrm{RIU}$) may also be present due to compressive pressure on the gain cores, which is exerted by the thermal shrinkage of the aluminium layer after deposition in the sputtering chamber (see Appendix B).

3.6 Conclusion

In conclusion, we have demonstrated room-temperature lasing from sub-wavelength metallo-dielectric resonators. In addition to reducing the size below the emission wavelength in all three dimensions, the metal layer isolates the cavity from its outer environment. Extending the current design approach to an electrically pumped structure may have practical applications such as dense optical interconnects [98] and laser arrays for optical trapping and manipulation of particles [99], both of which are currently limited by the larger size and lateral coupling effects in vertical-cavity surface-emitting laser (VCSEL) arrays. It should be noted that a characteristic of this laser design is that it allows the placement of two coherent sources in very close proximity while allowing them to operate independently with no cross-coupling. According to the Rayleigh criterion, two point sources that are placed closer than 0.61 (λ/NA) cannot be resolved into separate spots in the image plane (where λ and NA are the wavelength and numerical aperture of the imaging system, respectively). This places an upper bound on the maximum packing density of a free-space optical interconnect system. For an imaging system with NA= 0.8 and operating at 1.55 µm, the Rayleigh distance is $\sim$ 1.2 µm, which is slightly larger than the minimum spacing achievable with this nanolaser ($\sim$ 1.1 µm). Crossing the Rayleigh limit implies that arrays of this type of nanolaser can potentially reach the diffraction-imposed maximum bound on interconnect density. It should be stressed that passing this limit might also be advantageous for potential near-field applications that may benefit from further reduction in the nanolaser size. However, it should also be noted that, due to the physical limits imposed on the size of resonators incorporating conventional reflective resonances (such as the current nanolaser design), using this approach to reduce the resonator dimensions to sizes far below $\lambda_0/2n$ ($\sim$ 200 nm, assuming λ_0=1,550 nm and n=3.4) is not feasible and the solution will most probably lie in the realm of plasmonic resonant devices [15], assuming that the high room-temperature loss in such cavities can be efficiently surmounted.

The small size of the cavity may also enable the implementation of high-speed directly modulated lasers through spontaneous emission enhancement by

means of the Purcell effect [100]. The estimated Purcell factor for the current design lies between 19 and 41 (see Appendix C). Using silver instead of aluminium is expected to improve the threshold characteristics of these lasers because of its superior optical properties. With a silver shield, the estimated Q-factor for the same cavity at room temperature is $\sim$ 3,350, the gain threshold is only $\sim 50\,\mathrm{cm}^{-1}$ and the estimated Purcell factor range lies between 62 and 137. Furthermore, given that the current resonator design is readily scalable to longer wavelengths (due to the improved optical properties of metals in the infrared), it may also be applied to develop planar arrays of metallo-dielectric quantum-cascade lasers that are integrated with metallic beam-forming elements [101] and can be used for high-resolution imaging in the mid- and far-infrared regions of the spectrum.

Chapter 3, in full, is a reprint of the material as it appears in "Room-temperature subwavelength metallo-dielectric lasers," M. Nezhad, A. Simic, O. Bondarenko, B. Slutsky, A. Mizrahi, L. Feng, V. Lomakin, and Y. Fainman, *Nature Photonics*, vol. 4, no. 6, pp. 395–399, 2010. The dissertation author was the primary co-investigator and coauthor of this paper.

Chapter 4

Wafer bonded subwavelength metallo-dielectric laser

4.1 Introduction

Realization of silicon compatible active optical components is critical for creating integrated silicon photonic circuits, and a major step towards integration with CMOS-compatible platforms. Silicon has good thermoconductive properties, high quality oxide, low cost, and is available in high quality wafers, making it invaluable for integrated electrical circuits and waveguides. Unfortunately, the indirect bandgap of silicon poses a fundamental barrier to enabling light amplification and stimulated emission in this material. Successful advances toward overcoming this limitation include demonstration of silicon Raman lasers [102] and light emission in silicon-based nanoengineered materials [103]. However, Raman laser operation is based on optical scattering, which makes it essentially limited to operation under external optical pumping. Silicon nanostructures, in turn, suffer from low gain, and therefore, low efficiency.

An alternative solution is to build hybrid optical devices through integration of III-V gain with silicon [104] using wafer bonding. III-V semiconductor compounds offer the benefits of a direct energy bandgap with wide achievable range, and high carrier mobility. This makes the III-V material system optimal for

active optical elements and logical devices such as lasers, switches, and modulators. In addition to integration with silicon, another major goal of current photonics research is to reduce device footprints. Miniaturization is of great importance for the realization of compact photonic circuits for optical interconnects on-chip optical communication and sensing. Many applications often require high density packaging of laser structures, and therefore three dimensional minimization of the lasers is ultimately desired. To date, several different subwavelength lasing structures were reported by a few research groups [15,16,92,105–107], but integration of subwavelength lasers with passive silicon photonics still remains a challenge. Earlier we demonstrated room-temperature operation in sub-wavelength metallo-dielectric lasers [20,106], where the dielectric shield between metal cavity and InGaAsP gain core allows us to achieve lasing at room temperature through metal loss reduction [20]. However, building a practical ultra-compact on-chip device prompts us to address a few issues that include integration of the optical gain material with a silicon-on-insulator (SOI) wafer, assembly of an electrically injected laser cavity and laser-to-waveguide mode coupling. In the original design, the nanolaser is optically pumped and mounted on a glass slide with the output light propagating in free space (Figure 4.1a). The wafer bonding approach offers a path to realization of an electrically pumped sub-wavelength laser with vertical mode coupling to a silicon photonic waveguide by means of a slanted mirror, for example [108].

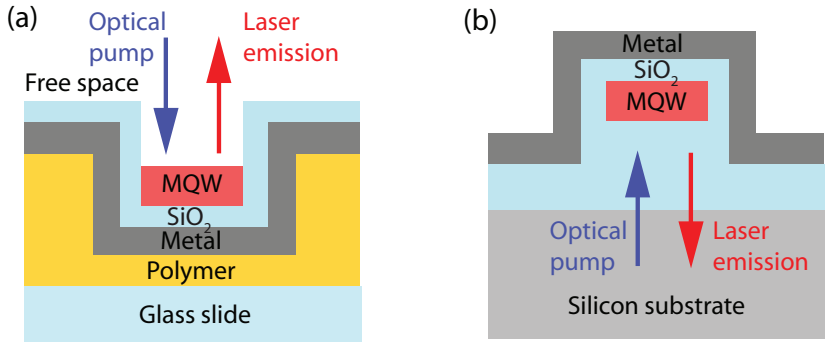

Figure 4.1: **(a)** Scheme of the original sub-wavelength metallo-dielectric laser setup as from [106]; **(b)** Scheme of a wafer bonded metallo-dielectric laser to be reported in this paper.

In order to exclusively investigate wafer bonding problems, we choose to

keep the original cavity mode of the optically pumped nanolaser [106] intact. Thus, the III-V-to-silicon wafer bonding has to be mediated by low refractive index material, such as SiO_2, to achieve vertical mode confinement (Figure 4.1b). The mediator layer has to be thick enough to reproduce the 500 nm air plug in the original design. Next, we need to select a reliable and versatile wafer bonding method, which could be used for both III-V-to-Si and III-V-to-SiO_2/Si integration. The wide variety of available wafer bonding techniques includes fusion bonding, anodic bonding, solder bonding, eutectic bonding, thermocompression bonding, direct metal-to-metal bonding, ultrasonic bonding, low-temperature melting glass bonding, and adhesive bonding [73]. Our choice was determined by the cavity design, which required a direct low temperature (below 400 °C) bond of an InGaAsP multiple quantum well (MQW) active layer to a silicon base. Conventional high temperature direct wafer bonding (fusion bonding) is known to have an adverse effect on the III-V layer quality due to a thermal expansion constant mismatch of the bonded materials. Some of the available low temperature wafer bonding methods may be useful, but would require additional studies of the bonding mediator's optical and material properties (adhesive wafer bonding), its possible chemical interaction with the gain layer (anodic wafer bonding) and incorporation of these new layers into the original nanolaser model. Recently, Liang et al reported a plasma assisted wafer bonding method [109, 110], which they successfully used for realization SOI-compatible optoelectronic devices [104]. Hence, in this work we demonstrate a silicon-compatible metallo-dielectric nanolaser and investigate the feasibility of this fabrication approach for integration of the device with silicon photonics platform.

4.2 Design and Simulations

Microdisk resonators with conventional whispering gallery mode (WGM) designs can be reduced to subwavelength scale [88], but the corresponding mode for the small structure is loosely bound, such that its evanescent tail is spread far beyond the physical resonator boundaries. This creates two problems. First,

it increases the threshold requirements since the mode/gain overlap is reduced. Second, coupling between the modes of neighboring resonators makes the WGM resonators unsuitable for densely packed laser arrays. These issues can be solved by enclosing the semiconductor resonator in a metal cavity [92]. While the metal cavity introduces strong mode confinement and thereby increases the mode-gain overlap, it also introduces high Ohmic losses. The last circumstance poses a difficulty on the way to room temperature lasing in subwavelength metallic resonators. Our approach to overcoming the metal losses is to incorporate a dielectric shield layer between the metal and semiconductor [20]. The shield thickness can be optimized for a fixed outer diameter of the laser. For an optimum shield thickness the losses reduce such that threshold gain is small enough for room temperature operation. In this case, we are still benefiting from the metal confinement, but the dielectric shield separates the largest portion of the mode, concentrated in the high index gain core (~ 3.5 for bulk InGaAsP), from direct interaction with the metal. Excessive shield thickness is detrimental, because the dielectric layer takes space that could otherwise be filled with the gain medium. Here we attempt to adapt this approach for an InGaAsP MQW gain layer, wafer bonded to SiO_2/Si (silicon wafer with thermally grown silicon dioxide layer), using our original design for the InGaAsP/InP material system. Figure 4.2a shows a schematic of a sample metallo-dielectric nanolaser, optimized for minimum lasing threshold at a nominal wavelength of 1,550 nm and outer radius of the resonator $R_{out} = 460$ nm. For a structure of these dimensions, the optimal shield thickness (Δ) and gain core radius (R_{core}) are 200 nm and 250 nm, respectively [20]. The gain core of the laser consists of InGaAsP with MQW (the actual composition of the gain layer is summarized in Table 4.1. A layer of metal (silver) confines the electromagnetic fields within the cavity. The gain is separated from the metal by a shield layer of low-index dielectric (SiO_2). The dielectric regions with low effective index above and below the gain cylinder ("plugs") provide vertical confinement of the resonator mode, as the lasing mode is in cutoff there. The lower plug is comprised of thermal SiO_2, in contrast to the original air plug from our previous work. This setup does not introduce any significant changes in the design, since the refractive index of SiO_2

is only slightly higher (1.46 versus unity for air). Finite element method (FEM) simulation of the laser resonator is shown in Figure 4.2b. The dielectric layer has been optimized for the TE_{012} mode, which has higher wavelength cutoff compared to the other lower order modes, but has the lowest achievable threshold gain of $36\,cm^{-1}$ for the designed structure [20].

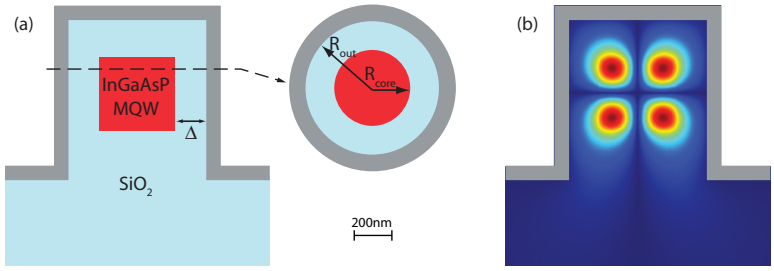

Figure 4.2: **(a)** Schematic drawing of the wafer bonded metallo-dielectric resonator design; **(b)** FEM simulation of TE_{012} mode in metallo-dielectric resonator with $R_{out} = 460\,nm$, optimized for 1,550 nm wavelength.

4.3 Fabrication

The wafer bonded sub-wavelength metallo-dielectric structures are fabricated from an InGaAsP multiple quantum well gain layer, bonded to a silicon wafer with a SiO_2 layer on top. The complete fabrication scheme is outlined in Figure 4.3. The silicon wafers have a 6 µm thermally grown oxide layer on the surface. The MQW InGaAsP/InP wafer was ordered from OEpic Semiconductor, Inc. This gain layer is comprised of 16, 10 nm thick, wells ($In_{x=0.560}Ga_{1-x}As_{y=0.938}P_{1-y}$) embedded in 17, 20nm thick, barriers ($In_{x=0.734}Ga_{1-x}As_{y=0.571}P_{1-y}$), epitaxially grown on an InP substrate, $\sim$ 500 nm thickness in total (Table 4.1). InGaAsP MQW active layer bonding to the SiO_2/Si was accomplished through low temperature plasma assisted wafer bonding (Figure 4.3a – c). The process is adapted from the III-V-to-Si bonding procedure recently developed by Liang et al. [109, 110] and is described below.

The wafer bonding is performed for an InGaAsP/InP chip of $\sim 1\,cm^2$ area and a SiO_2/Si chip of $\sim 2\,cm^2$ area. The low temperature bonding starts with

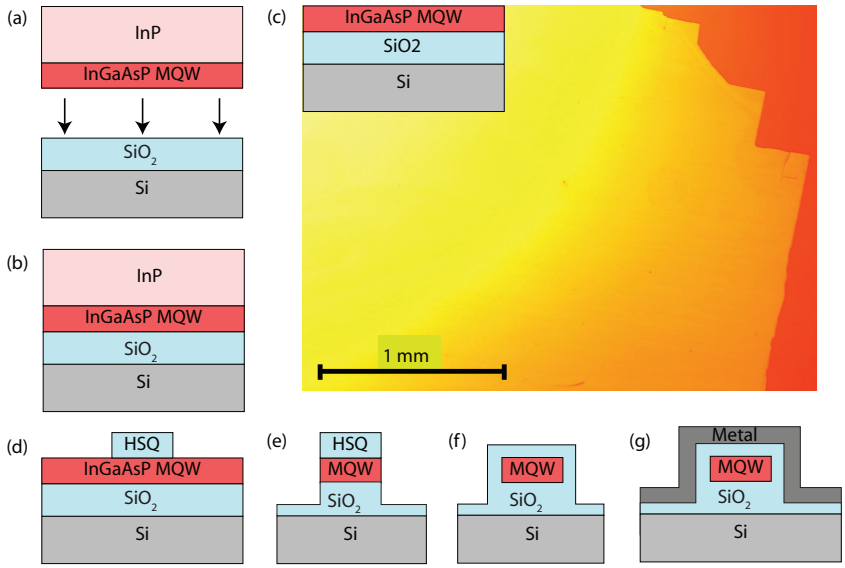

Figure 4.3: Fabrication steps of a wafer bonded metallo-dielectric laser: **(a)** wafer bonding of InGaAsP to SiO_2/SI, **(b)** resultant InP/InGaAsP/SiO_2/Si structure, **(c)** wet etching of InP substrate and the optical microscope image of 500 nm InGaAsP MQW layer bonded to SiO_2/Si chip; **(d)** e-beam lithography patterning; **(e)** laser pillar after two step RIE of InGaAsP and SiO_2 ; **(f)** PECVD of SiO_2 shield; **(g)** metal sputtering (silver)

Table 4.1: Multiple quantum well InGaAsP/InP epitaxial structure

Name	Material	Thickness (Å)	Number of layers
Capping layer	InP	100	1
Active region	$In_{x=0.734}Ga_{1-x}As_{y=0.571}P_{1-y}$	200	16
	$In_{x=0.560}Ga_{1-x}As_{y=0.938}P_{1-y}$	100	16
	$In_{x=0.734}Ga_{1-x}As_{y=0.571}P_{1-y}$	200	1
Substrate	InP	$\sim$ 325 µm	1

ultrasonication of the cleaved wafers in solvents to remove all particles that would inhibit interaction between the surfaces. InGaAsP/InP is dipped in HCl for 10 s prior to the wafer bonding to remove the InP capping layer. Ultrasonication in acetone and isopropanol (IPA), followed by thorough DI water rinse are necessary to eliminate particles from the bonding surfaces. This is a crucial step, since a single 1 µm size particle results in an unbonded area of 1 cm^2 [111]. Next, the surfaces are to be stripped of native oxides, organic, and ionic contaminations. The chemical

treatment is performed using standard RCA clean (NH_4OH:H_2O_2:H_2O=1:2:10) for 10 minutes at $65-75\,^{\circ}C$ on the InGaAsP/InP chip, and modified RCA clean (HCl:H_2O_2:H_2O =0.2:1:5) for 10 minutes at $80\,^{\circ}C$ on the SiO_2/Si chip. Then, the InGaAsP/InP chip is immersed into NH_4OH to remove any native oxides and small contaminations left from the previous step, while SiO_2/Si is treated in H_2SO_4:H_2O (3:1) for 10 minutes to strip any traces of organic contaminants. The chemical clean is followed by ultrasonication in acetone, IPA, careful DI water rinse and drying in N_2 flow. After cleaning, both chips undergo O_2 plasma surface activation in a Trion reactive ion etch (RIE) chamber with 20 mTorr pressure, 30 sccm O_2 flux and 50 W RF power for 45 seconds. The oxygen plasma treatment is immediately followed by a brief rinse in DI water to passivate the active surfaces with hydroxyl (–OH) groups. The water flow also takes away any new particles that may have accumulated during the plasma activation. Next, nitrogen flow-dried chips are manually mated. The Van der Waals force between the –OH groups promotes spontaneous mating of activated surfaces. The pair is annealed for 17 hours at $300\,^{\circ}C$ in an oven to form strong covalent bonding and encourage out-diffusion of the H_2O and H_2 byproducts through the thick SiO_2 layer from the InGaAsP/SiO_2 interface. Lastly, the InP carrier substrate is selectively etched by HCl from the bonded sample to obtain the composite InGaAs/SiO_2/Si structure (Figure 4.3c).

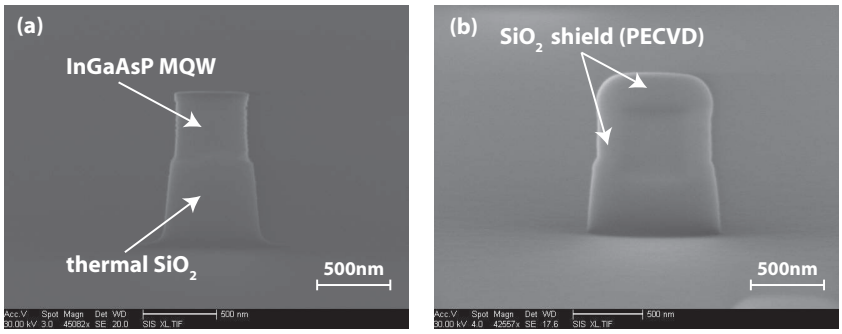

Figure 4.4: SEM micrographs of: **(a)** a laser pillar after two step RIE, and **(b)** the same pillar after PECVD of 200 nm thick SiO_2 layer.

The next step is to perform a double step reactive ion etch (RIE), which has to be carried out on the gain layer and SiO_2 using appropriate etching chemistry for each of the two materials. E-beam lithographic processing was performed on

hydrogen silsesquioxane (HSQ) negative resist to create a mask (Figure 4.3d). This is followed by the two-step RIE to form the cylindrical gain core and bottom SiO_2 plug. First, the 500 nm thick InGaAsP MQW layer is dry etched in CH_4:H_2:Ar (4:40:20 sccm) chemistry. Then the SiO_2 layer undergoes CHF_3/Ar (25/25 sccm) RIE to obtain a 500 nm tall SiO_2 post (Figure 4.33e depicts a schematic drawing of the structure after both these steps are performed). The HSQ mask is removed during the last fabrication step along with SiO_2, since its chemical composition is quite similar to that of SiO_2. Next the sample is treated in microwave oxygen plasma (Tepla 100) to eliminate polymer buildup. An SEM image of a sample laser after the cleaning is presented in Figure 4.4a. Next, PECVD of 200 nm thick SiO_2 is carried out to form the low index shield around the InGaAsP core (Figure 4.3f). Corresponding SEM image is shown in Figure 4.4b. In the final step we sputtered silver using a Denton Discovery 18 sputterer on the sample to complete a laser cavity (Figure 4.3g).

4.4 Measurements

We use a standard micro-photoluminescence setup for optical characterization of the wafer bonded nanolasers [106]. For optical pumping we employ 1,064 nm pulsed fiber laser which has a repetition rate of 300 kHz and 12 ns pulse width. The pump beam was focused down to an approximately 8 µm diameter spot size (FWHM), at the sample aperture plane, using 20× microscope objective. The beam intensity profile was observed using an IR InGaAs camera (Indigo Alpha NIR). The profile, together with the measured pump power, allowed us to estimate the peak pump intensity. The light emitted by a nanolaser is collected with the same objective and passed to the detection system. Using a double 4-f imaging system in conjunction with a pump filter (Semrock RazorEdge long wavelength pass), the samples are imaged onto either the IR camera, an electrically cooled InGaAs detector, or a monochromator (Spectral Products DK480) with a resolution of 0.35 nm, equipped with a cooled InGaAs detector in a lock-in detection configuration. Total power measurements for the light-light curves are performed using

an InGaAs detector. The monochromator is utilized for high resolution measurements in lasing mode to obtain the stimulated emission peak linewidth. Optical measurements at 77 K are performed using a Janis ST-500 cryogenic chamber.

The resonant modes of the structures were found to deviate from the design 1,550 nm wavelength by over 100 nm due to a variety of fabrication factors including slight ellipticity, deviation from nominal size, sidewall curvature, etc. For characterization, we selected devices with resonant modes close 1,550 nm where the InGaAsP MQW material has maximum gain, since these devices may be expected to perform best. Permanent performance degradation has been observed in most devices after prolonged exposure to high pump powers. We speculate that high pump powers cause damage to the gain core. Since the light-light curves provide more conclusive evidence of lasing than linewidth measurements, we have carried out light-light measurement first. This made subsequent linewidth measurements unreliable in some cases, particularly for smaller devices.

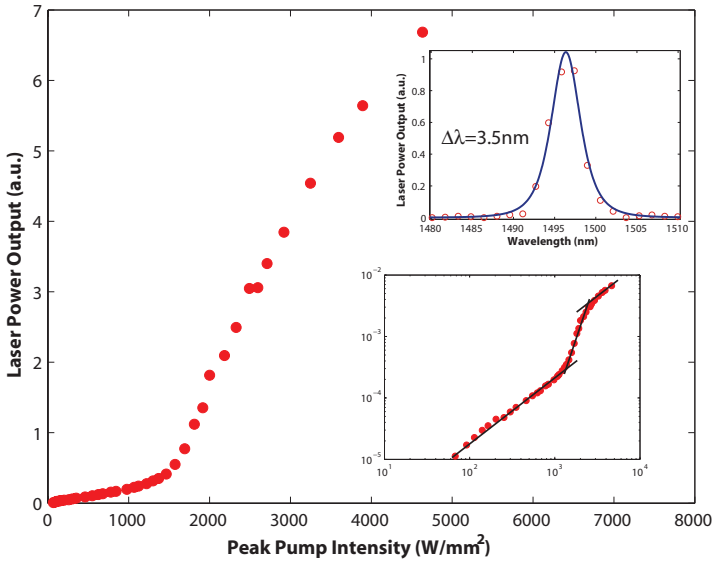

Figure 4.5: Room temperature light-light curve for a nanolaser with gain core radius of $R_{core} = 450$ nm. The same data set is shown in the bottom inset as a log-log plot. The upper inset is the lasing spectrum taken with spectrometer; measured linewidth is 3.5 nm

We observed room temperature lasing from a sample with approximate gain

core radius $R_{core} \approx 450\,\text{nm}$ and peak wavelength of 1,496 nm. A kink in the linear scale light-light curve (Figure 4.5) indicates the onset of lasing at the external threshold pump intensity of 1,100 W/mm^2. The same data set is shown in a log-log plot in the inset graph. For an ideal laser the S-shaped curve represents the transition from photoluminescence (PL) mode (the lower linear section with slope 1) through amplified spontaneous emission (ASE) mode (linear section with a slope steeper than 1) into stimulated emission mode (also slope 1). The unity slope indicates a linear dependence of output power on input pump power. The stimulated emission spectrum (the upper inset in Figure 4.5) has been measured after the light-light curve, and is probably affected by material degradation discussed earlier. Other similar sized devices exhibited RT linewidths between $\sim$ 1.5 and 5 nm.

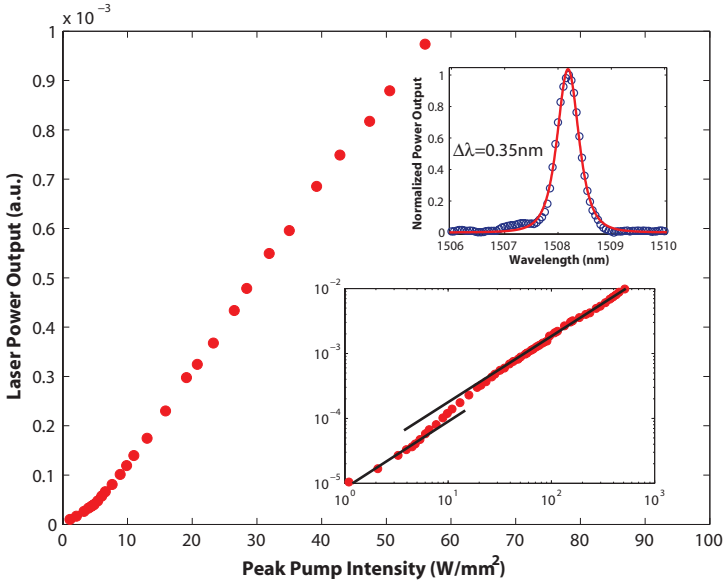

Figure 4.6: The light-light curve for a nanolaser with gain core radius of $R_{core} =$ 450 nm at 77 K. The same data set is shown in the bottom inset graph as a log-log plot. The upper inset is the lasing spectrum taken with monochromator; measured linewidth is 0.35 nm

Room temperature lasing from smaller samples ($R_{core} \approx 250\,\text{nm}$) exhibited severe drop of the stimulated emission peak intensity over time, especially after the samples had been subjected to high pump powers. That prevented reliable light-

light curve measurements of small (sub-wavelength) samples. To achieve lasing at lower pumping levels, we also performed optical measurements at 77 K, with samples placed in a cryogenic chamber. The light-light curves for both $R_{core} \approx$ 450 nm (Figure 4.6) and 250 nm (Figure 4.7) are presented, with the corresponding log-log curves on the inset graphs.

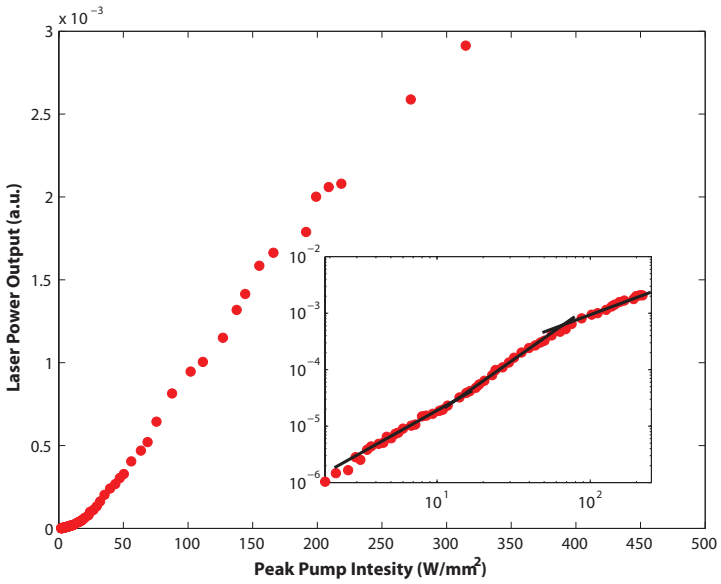

Figure 4.7: The light-light curve for a nanolaser with gain core radius of $R_{core} \approx$ 250 nm at 77 K with the corresponding log-log plot in the inset graph.

For the nanolaser with $R_{core} \approx 450$ nm and peak wavelength of 1,508 nm, the threshold at 77 K is reduced to 100 W/mm^2, which is approximately 10 times lower compared to the RT results for a sample of the same geometry. The linewidth is measured to be 0.35 nm, from the high-resolution spectrum shown on the upper inset of Figure 4.6. The significant linewidth narrowing at 77 K compared to the room temperature width is an expected phenomenon, which originates from reduced cavity losses, increased output power [112] and smaller linewidth enhancement factor [113]. The smooth ASE transition region and reduced threshold pump density of the S-curve at 77 K result from increased material gain, suppressed spectral broadening, enhanced cavity Q and much lower non-radiative recombination rates at cryogenic temperatures [112, 114].

For the 250 nm sample the lasing wavelength at 77 K is 1,527 nm and the

threshold is about $12\,\mathrm{W/mm^2}$, as shown in Figure 4.7. The emission spectrum of this sample, measured after the light-light curve, was severely affected by material degradation and is not shown. The slope of the PL-related linear part of the log-log curve (inset of Figure 4.7) is around 1.2, in contrast to the samples with $R_{core} \approx 450\,\mathrm{nm}$ for which the slope is close to unity. The PL region slope larger than unity indicates that a significant fraction of recombination events is caused by single-particle non-radiative processes, such as surface recombination [115]. In the smaller nanolasers, surface recombination is likely to be responsible for the high PL slope, since the ratio of the gain core surface area to its volume for the sample with $R_{core} \approx 250\,\mathrm{nm}$ is much greater than the surface/volume ratio for the sample with $R_{core} \approx 450\,\mathrm{nm}$ and thereby, must introduce many more non-radiative recombination centers. Along with the problem of dramatic drop in stimulated emission intensity under optical pumping at room temperature, this is an interesting issue to be further investigated.

4.5 Conclusion

In this paper we demonstrate a wafer bonded subwavelength scale laser that can be integrated onto a silicon platform. We observe room temperature lasing from near-subwavelength structures with gain core radius $R_{core} \approx 450\,\mathrm{nm}$ and cryogenic temperature operation for sub-wavelength structures with $R_{core} \approx 250\,\mathrm{nm}$. The results for the optically pumped lasers are expected to improve through further optimization of the fabrication process. We believe that our approach to realization of subwavelength scale coherent sources, combined with the latest III-V-to-Si wafer bonding solutions, is a promising path for the realization of highly integrated and miniaturized room temperature silicon photonic devices. In addition, our unique metal-dielectric resonator design is of interest for a number of applications, such as on-chip communication, optical interconnects, sensing and storage.

Chapter 4, in full, is a reprint of the material as it appears in "Wafer bonded subwavelength metallo-dielectric laser," O. Bondarenko, A. Simic, Q. Gu, J. H. Lee,

B. Slutsky, M. P. Nezhad, and Y. Fainman, *IEEE Photonics Journal*, vol. 3, no. 3, pp. 608–616, 2011. The dissertation author was the primary co-investigator and coauthor of this paper.

Chapter 5

Optical mode propagation in passive waveguide gratings

5.1 Introduction

Wave propagation in periodic structures has been studied for many decades in optics, crystallography and solid state physics. All physical entities with wave properties (electron, phonon, photon) exhibit diffractive, reflective and resonant behaviors when they travel in periodic structures with the period dimensions on the wavelength scale. Examples include, amongst others, electronic movement in atomic lattices and semiconductor stacks; natural and artificial photonic crystals, and x-ray diffraction in crystals. Today we can purposefully engineer such phenomena in materials for practical use, including semiconductor superlattices for electron tunneling, anti-reflection coating operating in virtually any spectrum range, photonic crystal cavities and waveguides for signal amplification, routing, filtering and more.

In this chapter we examine transmission and reflection of electromagnetic wave in waveguide gratings, a type of optical periodic structures. To understand the wave propagation phenomena, we will analyze interactions between multiple optical modes, existing in the structures. The modes in the system are described by solutions to wave and Maxwell's equations. However, the exact analytical solu-

tions rarely can be obtained, and especially so for dielectric waveguides. Hence, we will use a perturbative approach to solving these equations approximately. Coupled mode theory (CMT) is a traditionally favored theoretical treatment for these structures and particularly useful for intuitive understanding of wave propagation in periodic waveguides [116].

We will start with brief review of Maxwell's equations, than we will discuss the full formulation of CMT for perturbed waveguides and finally will cover the treatment specifics for waveguide gratings with sub-micron cross-section and sidewall modulation [117].

5.2 Maxwell's equations

Maxwell's equations for time-dependant electromagnetic field in absence of sources are:

$$\begin{aligned} \nabla \times \mathbf{E} &= i\omega\epsilon\mathbf{B} \\ \nabla \times \mathbf{H} &= \mathbf{J} - i\omega\epsilon\mathbf{D} \\ \nabla \cdot \mathbf{D} &= \rho \\ \nabla \cdot \mathbf{B} &= 0 \end{aligned} \tag{5.1}$$

where $\nabla = (d/dx, d/dy, d/dz)$, ω is the angular frequency, $\mathbf{E}$ and $\mathbf{H}$ are electric and magnetic field vectors with units of V/m and A/m, respectively; $\mathbf{D}$ and $\mathbf{B}$ are the electric displacement and magnetic induction with units of C/m^2 and Wb/m^2, respectively. The entities ρ and $\mathbf{J}$ are the electric charge density and electric current density with units of C/m^3 and A/m^3, respectively. The electric displacement $\mathbf{D}$ and magnetic induction $\mathbf{B}$ describe the interaction between the electromagnetic wave with the matter in which it propagates. In turn, the electric charge density ρ and the electric current density $\mathbf{J}$ represent sources of electromagnetic fields, if any, present in the system.

In order to uniquely define the electric and magnetic field vectors in a particular medium, Maxwell's equations must be supplemented with the complimentary

material equations:

$$\begin{aligned} \mathbf{D} &= \epsilon\mathbf{E} = \epsilon_0\mathbf{E} + \mathbf{P} \\ \mathbf{B} &= \mu\mathbf{H} = \mu_0(\mathbf{H} + \mathbf{M}) \end{aligned} \tag{5.2}$$

where ϵ is a dielectric permittivity tensor, μ is a permeability tensor. $\mathbf{P}$ and $\mathbf{M}$ are the electric and magnetic polarizations of the medium. These two equations define the material response to the present electromagnetic field and vice versa. Constants ϵ_0 and μ_0 are the vacuum permittivity and permeability with values of 8.854×10^{-12} F/m and $4\pi \times 10^{-7}$ H/m, correspondingly. Under the influence of an electromagnetic field, charged particles may alter their distribution and motion patterns, in turn causing a response of the electromagnetic field. Thus, the original electromagnetic field will also change according to the electromagnetic response of the medium. Eqs.5.2 allow to redefine Maxwell's equations in terms of complex

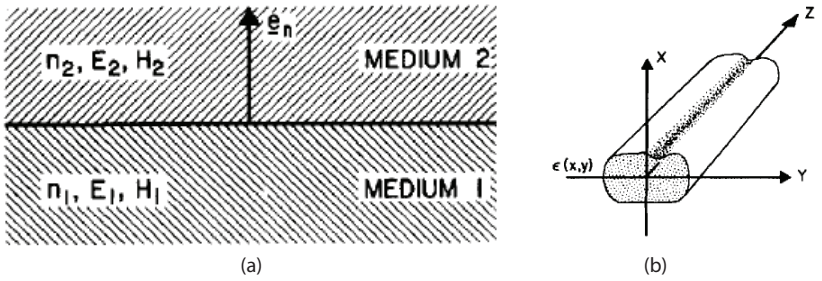

Figure 5.1: (a) Boundary between two media of indices n_1 and n_2. The vector e_n is the normal to the surface; (b) Sketch of a dielectric waveguide and the choice of the coordinate system. The guide axis coincides with the z-axis [Reprinted from [116]].

field amplitudes:

$$\begin{aligned} \nabla \times \mathbf{E} &= -i\omega\mu\mathbf{H}, \\ \nabla \times \mathbf{H} &= \mu\mathbf{H} = i\omega\epsilon\mathbf{E} \end{aligned} \tag{5.3}$$

Often, physical properties of the medium, characterized by ϵ and μ, undergo an abrupt change at surfaces and other material boundaries (Figure 5.1). Mathemat-

ically, these material discontinuities are defined by the boundary conditions:

$$\begin{aligned} e_n \cdot (\mathbf{B_1} - \mathbf{B_2}) &= 0, \\ e_n \cdot (\mathbf{E_1} - \mathbf{E_2}) &= 0, \\ e_n \cdot (\mathbf{D_1} - \mathbf{D_2}) &= \sigma, \\ e_n \cdot (\mathbf{H_1} - \mathbf{H_2}) &= \mathbf{K}. \end{aligned} \tag{5.4}$$

where $\mathbf{E_1}$, $\mathbf{E_2}$, etc., are the fields in the immediate vicinity of the boundary, σ is the surface charge density ($\mathrm{C/m^2}$) and $\mathbf{K}$ is the surface current density ($\mathrm{A/m^2}$). In the absence of sources, i.e., when there is no charges or currents and hence $\sigma = 0$ and $\mathbf{K} = 0$, these boundary conditions become:

$$\begin{aligned} e_n \cdot (\mathbf{B_1} - \mathbf{B_2}) &= 0, \\ e_n \cdot (\mathbf{E_1} - \mathbf{E_2}) &= 0, \\ e_n \cdot (\mathbf{D_1} - \mathbf{D_2}) &= 0, \\ e_n \cdot (\mathbf{H_1} - \mathbf{H_2}) &= 0. \end{aligned} \tag{5.5}$$

It is convenient to separate fields into their transverse components, $\mathbf{E_t}$ and $\mathbf{H_t}$, and longitudinal components, $\mathbf{E_z}$ and $\mathbf{H_z}$, so that

$$\begin{aligned} \mathbf{E} &= \mathbf{E_t} + \mathbf{E_z}, \\ \mathbf{H} &= \mathbf{H_t} + \mathbf{H_z} \end{aligned} \tag{5.6}$$

We can obtain separate transverse and longitudinal components by modifying Maxwell's equations further:

$$\begin{aligned} \nabla_\mathbf{t} \times \mathbf{E_t} &= -i\omega\mu\mathbf{H_z} \\ \nabla_\mathbf{t} \times \mathbf{H_t} &= i\omega\epsilon\mathbf{E_z} \\ \nabla_\mathbf{t} \times \mathbf{E_z} + e_z \times \frac{\partial \mathbf{E_t}}{\partial z} &= i\omega\mu\mathbf{H_t} \\ \nabla_\mathbf{t} \times \mathbf{H_z} + e_z \times \frac{\partial \mathbf{H_t}}{\partial z} &= i\omega\epsilon\mathbf{E_t} \end{aligned} \tag{5.7}$$

where $\nabla_\mathbf{t} = (d/dx, d/dy, 0)$ and e_z is a unit vector pointing in the wave propagation direction z. When dealing with electromagnetic field propagation in waveguides, it is sufficient to solve exclusively for transverse field components, $\mathbf{E_t}$ and $\mathbf{H_t}$, since the longitudinal components will follow from Maxwell's equations, once the tangential components are solved by means of the wave equation, as discussed in Section 5.3).

5.3 Wave equation

Solutions of Maxwell's equations describe electromagnetic field propagation in a medium with certain properties. In general, time harmonic propagation of electric field in homogeneous, source-free ($\nabla \cdot \mathbf{E} = 0$) and lossless media must satisfy the vector equation:

$$\nabla^2 \mathbf{E} + {k_0}^2 n^2 \mathbf{E} = 0 \tag{5.8}$$

The solution to this equation for an ideal (i. e., straight and unperturbed) waveguide stretched along the z-axis, whether it is a slab, rectangular or cylindrical waveguide, is the following wave equation:

$$\mathbf{E}(x, y, z, t) = \mathbf{E}_m(x, y) e^{i(\omega t - \beta_m t)} \tag{5.9}$$

In reality, some waveguide perturbation always exists. For example, a slight dielectric permittivity perturbation along the z-axis due to imperfect fabrication techniques, will make Eq. 5.9 no longer valid for such waveguide. A perturbative approach is typically applied to overcome this limitation and find the eigenmodes in a perturbed waveguide. The perturbed waveguide eigenmodes can be represented as a superposition of an ideal waveguide eigenmodes (see Appendix H).

5.4 Mode excitation in waveguides

In presence of sources a new term appears in Maxwell's equation for the magnetic field, and the equation system 5.1 takes the following form:

$$\nabla \times \mathbf{H} = i\omega\epsilon\mathbf{E} \tag{5.10a}$$

$$\nabla \times \mathbf{H} = i\omega\epsilon\mathbf{E} + j\omega\mathbf{P} \tag{5.10b}$$

where the second term on the right side of Eq. 5.10b represents a distribution of sources, which excite various waveguide modes through the induced polarization vector $\mathbf{P}(x, y, z)$. In his coupled mode theory, Kogelnik [116] employs mode expansion of the wave equation to solve these Maxwell's equations and applies orthogonality relations to obtain formulas for mode amplitudes in presence of sources. The

change in the amplitudes of forward (A'_μ) and backward (B'_μ) propagating modes, with primes referring to differentiation with respect to z, due to the field sources ($\mathbf{P}(x,y,z)$) can be written as:

$$\begin{aligned} A'_\mu &= -j\omega \iint_{\infty}^{\infty} \mathbf{P} \cdot \mathbf{E^*}_\mu e^{j\beta_\mu z}\, \mathrm{d}x\, \mathrm{d}y \\ B'_\mu &= j\omega \iint_{\infty}^{\infty} \mathbf{P} \cdot \mathbf{E^*}_{-\mu} e^{-j\beta_\mu z}\, \mathrm{d}x\, \mathrm{d}y \end{aligned} \tag{5.11}$$

Note, that the amplitudes will stay constant in absence of sources, i.e., when induced polarization $\mathbf{P}(x,y,z) = 0$.

This description is very general, since it carries no assumptions. As such, it can be applied to lossy or lossless, homogeneous or nonhomogeneous media, since the permittivity value can be real, imaginary, complex or tensorial, as relevant to each case.

Let us consider a non-ideal waveguide with some distribution in permittivity $\epsilon(x,y,z)$ due to geometrical variations. This deformation can be expressed as a deviation $\Delta\epsilon(x,y,z)$ from the nominal permittivity distribution in an ideal waveguide $\epsilon(x,y)$. This deviation (or perturbation of permittivity) will result in an induced polarization, proportional to the electric field in the guide.

Upon substituting the expanded electric field in Eqs. 5.11, we obtain:

$$\mathbf{P_t} = \Delta\epsilon \mathbf{E_t} = \Delta\epsilon \sum (a_\nu + b_\nu) \mathbf{E_{t\nu}} \tag{5.12}$$

Variation in amplitudes can be expressed through permittivity variations, as well as the transverse and tangential components of the electric field:

$$\begin{aligned} A'_\mu &= -j\omega \iint_{\infty}^{\infty} \sum [(a_\nu + b_\nu)\Delta\epsilon \mathbf{E}_{t\nu} \cdot \mathbf{E^*}_{t\mu} + (a_\nu - b_\nu) \frac{\Delta\epsilon \cdot \epsilon}{\epsilon + \Delta\epsilon} \mathbf{E_{z\nu}} \cdot \mathbf{E^*}_{\mathbf{z}\mu}] e^{j\beta_\mu z}\, \mathrm{d}x\, \mathrm{d}y \\ B'_\mu &= j\omega \iint_{\infty}^{\infty} \sum [(a_\nu + b_\nu)\Delta\epsilon \mathbf{E}_{t\mu} \cdot \mathbf{E^*}_{t\mu} - (a_\nu - b_\nu) \frac{\Delta\epsilon \cdot \epsilon}{\epsilon + \Delta\epsilon} \mathbf{E_{z\nu}} \cdot \mathbf{E^*}_{\mathbf{z}\mu}] e^{j\beta_\mu z}\, \mathrm{d}x\, \mathrm{d}y \end{aligned} \tag{5.13}$$

where we have used symmetry relations to express the mode distribution $\mathbf{E}_{-\mu}(x,y)$ in terms of the component of the field $\mathbf{E}_\mu(x,y)$ of the corresponding forward propagating mode. To write these expressions in a more compact form, we introduce

tangential and longitudinal coupling coefficients $\mathbf{K^t}_{\nu\mu}(z)$ and $\mathbf{K^z}_{\nu\mu}(z)$:

$$\begin{aligned}\mathbf{K^t}_{\nu\mu} &= \omega \iint_{-\infty}^{\infty} \Delta\epsilon \mathbf{E}_{t\nu} \cdot \mathbf{E^*}_{t\mu}\, \mathrm{d}x\, \mathrm{d}y \\ \mathbf{K^z}_{\nu\mu} &= \omega \iint_{-\infty}^{\infty} \frac{\Delta\epsilon \cdot \epsilon}{\epsilon + \Delta\epsilon} \mathbf{E}_{z\nu} \cdot \mathbf{E^*}_{z\mu}\, \mathrm{d}x\, \mathrm{d}y\end{aligned} \tag{5.14}$$

The equations for mode amplitudes can now be expressed as:

$$\begin{aligned}A'_\mu = &- j\omega \iint_{\infty}^{\infty} \sum \{A_\nu(\mathbf{K^t}_{\nu\mu} + \mathbf{K^z}_{\nu\mu}) \exp[-j(\beta_\mu - \beta_\nu)z] \\ &+ B_\nu(\mathbf{K^t}_{\nu\mu} - \mathbf{K^z}_{\nu\mu}) \exp[j(\beta_\nu + \beta_\mu)z]\}\, \mathrm{d}x\, \mathrm{d}y\end{aligned} \tag{5.15}$$

$$\begin{aligned}B'_\mu = &j\omega \iint_{\infty}^{\infty} \sum \{A_\nu(\mathbf{K^t}_{\nu\mu} - \mathbf{K^z}_{\nu\mu}) \exp[-j(\beta_\mu + \beta_\nu)z] \\ &+ B_\nu(\mathbf{K^t}_{\nu\mu} + \mathbf{K^z}_{\nu\mu}) \exp[j(\beta_\nu - \beta_\mu)z]\}\, \mathrm{d}x\, \mathrm{d}y\end{aligned} \tag{5.16}$$

First, we would like to emphasize that the definition of coupling coefficient (Eq. 5.14) is central to CMT. It quantifies strength of interaction (or coupling) between forward and backward propagating modes due to variations in dielectric permittivity. In most cases we can safely neglect the longitudinal component of coupling coefficient, $\mathbf{K^z}_{\nu\mu}$, because the tangential component of electric field $\mathbf{E_z}$ contributing to its value, is very small compared to its transverse component $\mathbf{E_t}$ (see Eq. 5.14). The Eq. 5.14 and Eq. 5.16 show that co- and contra-directional coupling are different in presence of E_z components. Co-directional coupling is always stronger than contra-directional, since the forward and backward fields have the E_t components of the same sign and E_z components of the opposite sign.

Second, Eqs. 5.16 point to dependence of each individual mode amplitudes on the perturbation strength of waveguide dielectric permittivity $\Delta\epsilon$, modal field distribution and amplitudes of all other modes present in the guide.

5.5 Coupled mode analysis of contra-propagating waves

The simplest example of a periodic medium is a stack of alternating layers of two materials with dissimilar dielectric permittivity ϵ (Figure 5.2, a). This layer

arrangement introduces periodic modulation of the dielectric permittivity along the z-axis. Alternatively, such perturbation can be can be created in a waveguide of the same material by varying its geometry along the z-axis (Figure 5.2, b). Both of these approaches will result in a Bragg reflector with maximum reflectivity in a desired part of the spectrum, provided the grating period is appropriately chosen. The latter approach is very common to the field of nanophotonics, due to the ease of implementation. In this work we are also interested in reflective gratings with geometrically modulated dielectric permittivity. Let us consider wave propagation

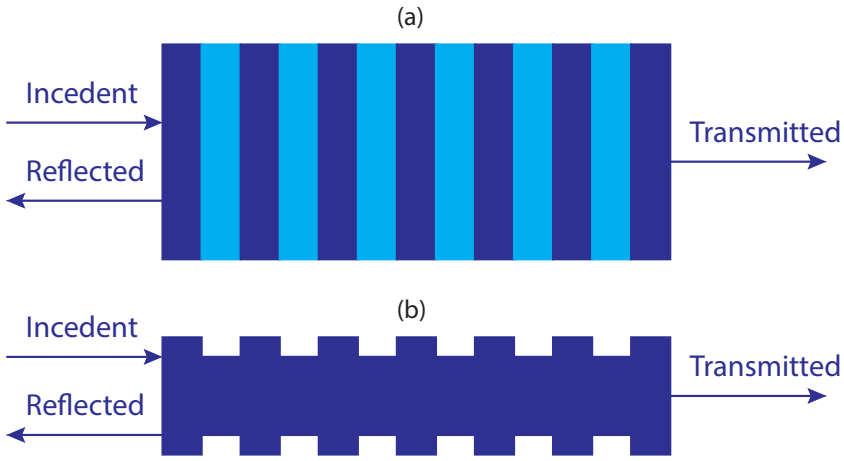

Figure 5.2: Passive grating with index modulation achieved via (a) alternating dissimilar materials (b) changing the waveguide width in the wave propagation direction.

in a slab waveguide with corrugation grating [116] under two assumptions: (1) all modes can be neglected, except for two guided modes (forward and backward propagating); (2) $\Delta\epsilon$ is a very small perturbation. As long as both assumptions are valid, purposeful periodic permittivity modulation in waveguide can be described the same way as the natural imperfections, discussed earlier in this chapter, i. e. in terms of ideal waveguide modes.

We will start by formulating a forward propagating mode with an amplitude A and a backward propagating mode with an amplitude B:

$$\begin{aligned} A' &= -j\kappa B \exp(-2j\delta z), \\ B' &= j\kappa A \exp(2j\delta z), \end{aligned} \tag{5.17}$$

where κ is a coupling coefficient and δ is a normalized frequency, which measures asynchronism. When modes are synchronous it equals 0. In this case, coupling coefficient κ is real and z-independent constant value. We will substitute

$$\begin{aligned} A &= R\exp(j\delta z) \\ B &= S\exp(-j\delta z) \end{aligned} \tag{5.18}$$

into Eqs. 5.17 and get the following coupled-wave equations:

$$\begin{aligned} R' + j\delta R &= -j\kappa S \\ S' - j\delta S &= j\kappa R \end{aligned} \tag{5.19}$$

The boundary conditions for the contra-propagating waves are set as $z = 0$ for the forward wave at the beginning of the region at hand; for the backward propagating wave S, $z = L$, where L is a total propagation length. For $R(0) = 1$ and $S(L) = 0$. Than, the solutions are:

$$\begin{aligned} S(0) &= \frac{-j\kappa}{\sqrt{\kappa^2 - \delta^2}\coth(L\cdot\sqrt{\kappa^2 - \delta^2}) + j\delta} \\ R(L) &= \frac{\sqrt{\kappa^2 - \delta^2}}{\sqrt{\kappa^2 - \delta^2}\cosh(L\cdot\sqrt{\kappa^2 - \delta^2}) + j\delta\sinh(L\cdot\sqrt{\kappa^2 - \delta^2})} \end{aligned} \tag{5.20}$$

where $S(0)$ is the amplitude of light reflected as a function of frequency δ and $R(L)$ is the amplitude of transmitted light. In order to calculate the reflection/transmission spectrum of a modulated waveguide, it is important to know the coupling coefficient specific to the geometry of the waveguide.

5.6 Calculation of the coupling coefficient in waveguides

Consider a dielectric waveguide with a geometry such as the one depicted in Figure 5.3(a) with small periodic perturbation of dielectric permittivity along z direction

$$\Delta\epsilon(x, y, z) = \epsilon_a(x, y) + \Delta\epsilon(x, y, z) \tag{5.21}$$

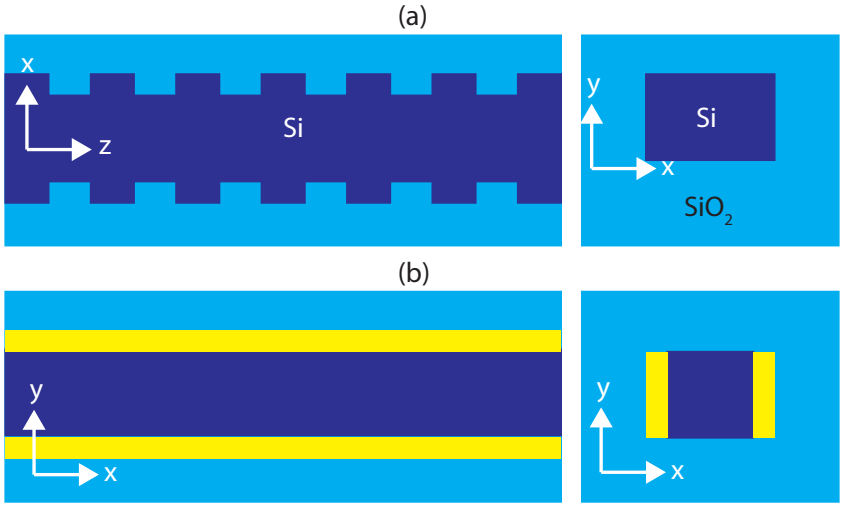

Figure 5.3: (a) Schematic top down (left) and cross-sectional (right) view of a real sidewall modulated silicon waveguide geometry, (b) the same waveguide, represented as a hypothetical "average" guide with modulated waveguide section displayed in yellow color. The permittivity in this section is calculated as $\epsilon = (\epsilon_{Si} + \epsilon_{SiO_2})/2$.

Recall, that $\Delta\epsilon$ is inside the integral in Eq 5.14. We can simplify Eq 5.14 by applying the Fourier expansion to the small dielectric perturbation $\Delta\epsilon$:

$$\Delta\epsilon(x, y, z) = \sum_{m \neq 0} \epsilon_m(x, y) e^{-im\frac{2\pi}{\Lambda}z} \tag{5.22}$$

where the summation is over all integers m, except $m = 0$. Note, that $\Delta\epsilon(x, y)$ no longer depends on z, which means that we can now treat it as a constant and take it out of the integral.

For the case of square-wave waveguide corrugation, we can rewrite the dielectric perturbation as

$$\Delta\epsilon(\mathbf{r}) = \begin{cases} \epsilon_0(\epsilon_1 - \epsilon_2) \sum\limits_{m=-\infty}^{\infty} b_m e^{-jm\frac{2\pi}{\Lambda}z} & \text{if } x \in [a + \delta a, -a - \delta a] \\ 0, & \text{otherwise.} \end{cases} \tag{5.23}$$

where b_m are the Fourier expansion coefficients. For the case at hand, a square wave modulation, these coefficients are [118]:

$$b_m = e^{jm\pi/2} \frac{\sin m\pi/2}{m\pi} \tag{5.24}$$

We will neglect all the Fourier terms except for the first one, $m = 1$, for which the Fourier coefficient is $b_m = \frac{j}{\pi}$. After we substitute the Fourier coefficient into the expressions for the coupling coefficient, Eq. 5.14, we obtain the coupling coefficients for a waveguide with a square wave modulation:

$$\begin{aligned} \mathbf{K^t}_{\nu\mu} &= \frac{\omega b_m}{4}\epsilon_0(\epsilon_1 - \epsilon_2)\iint\limits_{A_{mod}} \mathbf{E}_{t\nu} \cdot \mathbf{E^*}_{t\mu}\,\mathrm{d}x\,\mathrm{d}y \\ \mathbf{K^z}_{\nu\mu} &= \frac{\omega b_m}{4}\epsilon_0(\frac{\epsilon_1}{\epsilon_1 + \epsilon_0} - \frac{\epsilon_2}{\epsilon_2 + \epsilon_0})\iint\limits_{A_{mod}} \mathbf{E}_{z\nu} \cdot \mathbf{E^*}_{z\mu}\,\mathrm{d}x\,\mathrm{d}y \end{aligned} \tag{5.25}$$

where A_{mod} is the area of modulated region in $x, y-$plane and labeled yellow in Figure 5.3.

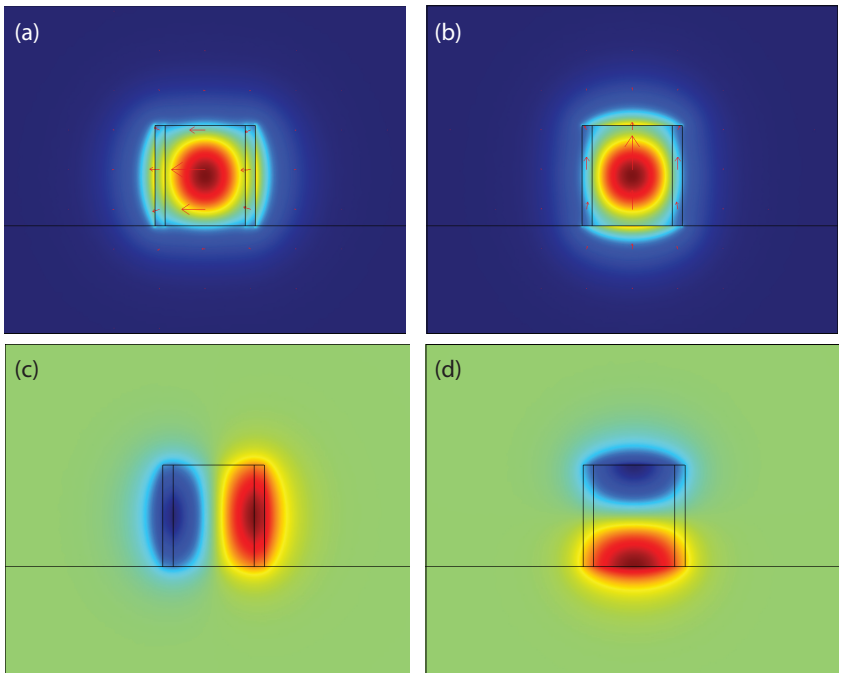

Figure 5.4: COMSOL simulations of fundamental propagating modes in a silicon waveguide. Normal electric field distribution in (a)TE-like mode and (b) TM-like mode. Tangential electric field, E_z component, in (c)TE-like mode and (d) TM-like mode.

Now only the electric field is left inside the integral. This integral defines the mode overlap within the grating. As such, it carries information about the power exchange between the optical fields in different waveguide modes μ and ν.

Next, we will consider a silicon waveguide, embedded into SiO_2 cladding, and a square cross-section of $500\times500\,\mathrm{nm}^2$. The top-down view and cross-section of the waveguide are schematically depicted in Figure 5.3 (a). The dielectric permittivity values at 1,550 nm wavelength for silicon and silicon dioxide are ϵ_1=12.11 and ϵ_2=2.16, respectively. We will exclusively cnsider the fundamental TE-like and TM-like modes (Figure 5.4). Normal and tangential field distributions for these two modes are simulated in COMSOL and shown in Figure 5.4 (a-d). Using the simplified formulation for coupling coefficients (Eq. 5.25), we obtain $K^t(TE)$=300 cm^{-1} and $K^z(TE)$=187 cm^{-1}; $K^t(TM)$=398 cm^{-1} and $K^z(TM)$=31 cm^{-1}. Thus, the total coupling coefficient, $K^t - K^z$, for a TM-like mode is higher (367 cm^{-1}) than for a TE-like mode (113 cm^{-1}) in this structure.

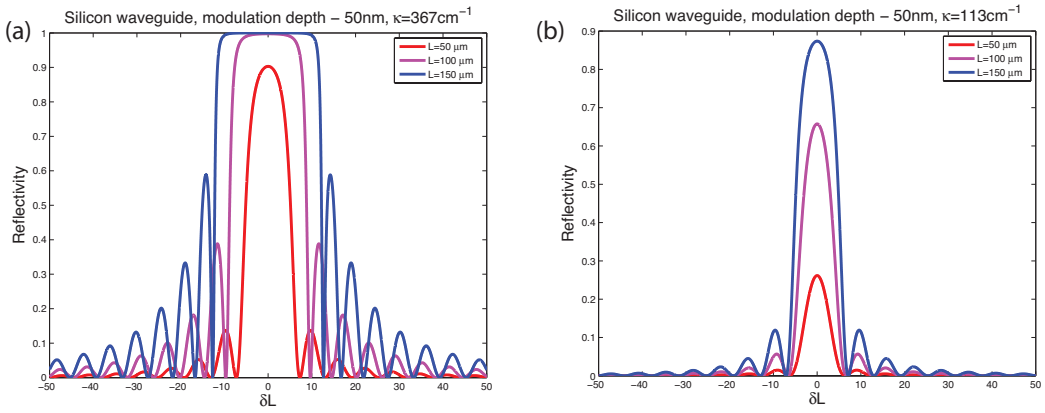

Figure 5.5: Reflectivity spectra for (a) TM-like and (b) TE-like modes in gratings with varying length (50 μm, 100 μm, 150 μm).

This difference in coupling strength can easily be explained by the fact that the longitudinal component of TE-like mode, $\mathbf{E_z}$, strongly overlaps with the modulated area, whereas for the TM-like mode, $\mathbf{E_z}$ is concentrated along the unmodulated edges of the waveguide (Figure 5.4, c,d). Figure 5.5 shows the calculated reflectivity spectra of waveguide gratings of different lengths. Evidently, the difference in reflectivity for the TE-like and TM-like modes of the same gratings is very significant. Reflectivity spectra of TM-like modes (Figure 5.5 (a)) are much wider and taller for the same grating lengths than the reflectivity spectra of TE-like modes in the same waveguide (Figure 5.5 (b)). This result suggests that TE-like

and TM-like modes will experience dramatically different dispersive behavior in the sidewall modulated waveguide gratings.

Chapter 6

Optical mode propagation in waveguide gratings with gain

6.1 Distributed feedback lasers

A distributed feedback laser (DFB) is a laser with a Bragg grating resonator acting as a distributed reflector within the gain medium. Light amplification and lasing in periodic structures with gain occurs due to their dispersive properties, i.e. varying amount of reflection, transmission and loss, experienced by each propagating mode. As we know from the previous chapter, these properties can be purposefully engineered to make the grating reflective in a particular part of spectrum.

A simplistic explanation of the operation principle of a DFB with geometrically modulated grating is schematically depicted in Figure 6.1. Consider a mode with frequency near the transmission maximum. As it propagates through the grating without any reflections, it does not spend enough time in the gain medium to get amplified (Figure 6.1, Case 1). Another mode with frequency near the reflection maximum is entirely reflected off grating almost as soon as it starts travelling through it (Figure 6.1, Case 2). However, when the mode is partially reflected and partially transmitted on each interface of the periodic structure, the optical field of the mode is effectively trapped inside the gain medium. As a result, this

mode may experience sufficiently long interaction with the gain to be amplified by it and, eventually, reach stimulated emission (Figure 6.1, Case 3).

Couple mode theory, introduced in the previous chapter, is a simple, accurate and intuitive method of determining the lasing threshold in distributed feedback lasers. Before we move to the chapter on experimental demonstration of the wafer bonded DFB (Chapter 7), we want to gain an insight into the general DFB operation principles and lasing threshold analysis using CMT [119].

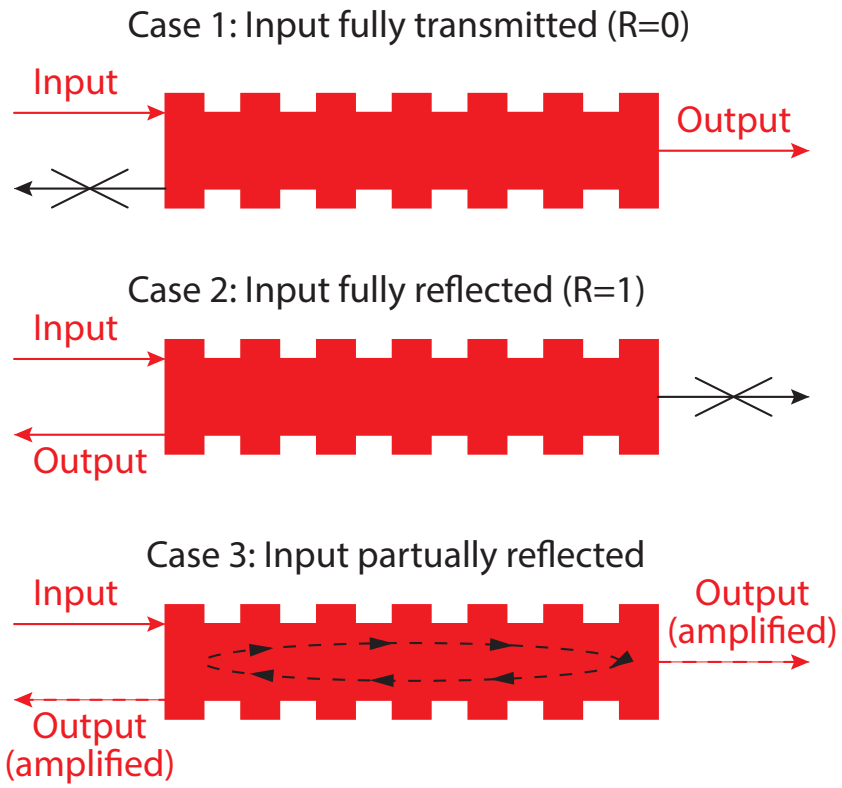

Figure 6.1: Schematic demonstration of a simple distributed feedback laser operation principle. A simple DFB cavity is comprised of a single section grating, embedded in material with a non-zero optical gain coefficient.

Note that CMT is not valid for systems below or above threshold, as it doesn't account for nonlinear effects in gain media, such as gain saturation or spectral hole burning. Analysis of these dynamic effects must be carried out using rate equation theory [39], which is outside the scope of this dissertation.

We will use several assumptions in our CMT treatment of DFB lasers: (1) the laser oscillating frequency is near Bragg frequency ($\omega \approx \omega_0$), (2) the gain is low

over distances on the order of the wavelength ($\alpha \ll \beta_0 \equiv 2\pi n/\lambda_0$), (3) the system is subjected to only a small perturbation of refractive index and gain. Building on the assumption (1) we can safely neglect higher orders of the grating and only consider the two fundamental modes: forward and backward propagating, but otherwise identical. These modes will be further denoted as propagating (R) and contra-propagating (S) modes. Kogelnik et al. [119] arrived to a pair of coupled equations that describe the modes' complex amplitudes across the grating:

$$\begin{aligned} -R' + (\alpha - j\delta)R &= j\kappa S \\ S' + (\alpha - j\delta)S &= jkR \end{aligned} \tag{6.1}$$

where α is the gain constant, κ is a coupling coefficient (constant), and δ is a normalized frequency:

$$\delta \equiv \frac{\beta^2 - {\beta_0}^2}{2\beta} \sim \beta - \beta_0 = n(\omega - \omega_0)/c \tag{6.2}$$

where n is the average refractive index of the medium and c is the speed of light in vacuum. The parameter δ quantifies the deviation of the oscillation frequency from the Bragg frequency ω_0. When the oscillation frequency coincides with Bragg frequency, $\delta = 0$.

In the original presentation of CMT, the coupling coefficient was defined as

$$\kappa = \frac{\pi n_1}{\lambda_0} + \frac{1}{2} j\alpha_1 \tag{6.3}$$

where n_1 and α_1 are the amplitudes of refractive index and gain modulation in the periodic structure.

Let us now consider a periodic structure of length L with no incident optical field and internal fields starting at zero amplitude at the boundaries of this structure. The boundary conditions for the described periodic structures are:

$$R(-\frac{L}{2}) = S(\frac{L}{2}) = 0 \tag{6.4}$$

The coupled-wave equation 6.1 together with the boundary conditions 6.4 yields a set of discrete oscillating states, or existing longitudinal modes in the periodic structure with corresponding values of threshold gain. Each of these

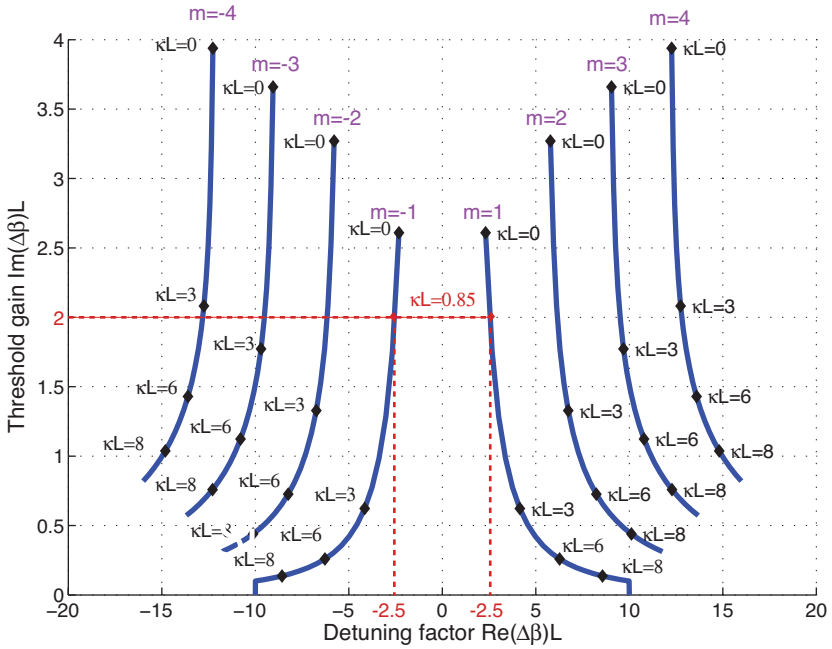

Figure 6.2: Complex space of resonant condition solutions for four forward and four backward propagating longitudinal modes. The solutions represent lasing threshold for single section DFB lasers without facet reflections.

modes has a complex detuning parameter $\delta = Re(\delta) + i\,Im(\delta)$, associated with it, where the real part corresponds to the detuning from Bragg frequency and the imaginary part corresponds to the loss this frequency sustains in the grating. This solutions can be plotted on a compex plane with normalized real part of detuning parameter δL on x-axis and normalized imaginary part on y-axis (see Figure 6.2). The solution only gives a relative value of threshold gain for each mode, compared to all the other modes. However, the actual gain value required to reach threshold can be calculated if the grating length, modal loss and the gain/mode overlap are known [120].

The general solution to the equation system 6.1 takes the following form:

$$\begin{aligned} R &= r_1 e^{\gamma z} + r_2 e^{-\gamma z} \\ S &= s_1 e^{\gamma z} + s_2 e^{-\gamma z} \end{aligned} \tag{6.5}$$

where the complex propagation constant satisfies the dispersion relation:

$$\gamma^2 = \kappa^2 + (\alpha - j\delta) \tag{6.6}$$

The symmetricity of the grating yields two sets of solutions for the optical field: symmetric, i. e. when $E(-z) = E(z)$, and antisymmetric, with $E(-z) = -E(z)$. This assumption of symmetricity entails the following relation between r_1 and s_1:

$$\begin{aligned} r_1 &= \pm s_2 \\ r_2 &= \pm s_1 \end{aligned} \tag{6.7}$$

Recalling the previously defined boundary conditions 6.4, we arrive to another useful relation between these coefficients:

$$\frac{r_1}{r_2} = \frac{s_2}{s_1} = -e^{\gamma L} \tag{6.8}$$

These results help us to find concise expressions for the optical field along the grating:

$$\begin{aligned} R &= \sinh \gamma (z + \frac{1}{2}L), \\ S &= \pm \sinh \gamma (z - \frac{1}{2}L) \end{aligned} \tag{6.9}$$

After some manipulations [119] we arrive to a transcendental equation for the eigenvalues γ of the DFB structure and their respective resonant frequencies δ and threhold gain coefficients α:

$$\begin{aligned} \kappa &= \pm \frac{j\gamma}{\sinh \gamma L} \\ \alpha - j\delta &= \pm \kappa \cosh \gamma L = \gamma \coth \gamma L \end{aligned} \tag{6.10}$$

In general, each of the parameters (γ, δ, α) are complex. Their real parts are associated with the physical frequency of the mode and their imaginary parts are associated with gain or loss, experienced by this frequency. These equations can be solved for a complex $\beta = \delta + j\alpha$ exactly through iterative algorithms, such as the Newton-Raphson solver in Matlab.

6.2 Gain and index coupled DFB lasers

The coupling coefficient κ is a central parameter of CMT. It describes the coupling strength between a propagating mode and any number of other co- and

contra-propagating modes in the waveguide. However, we assumed that only coupling of the first order propagating mode into the identical contra-propagating mode is sufficiently strong to be considered in the analysis. Generally, κ is a complex number, with its real part associated with modulation of the refractive index in the system. Its imaginary part, on the other hand, is associated with modulation of gain or loss. This notion suggests that mode-to-mode coupling can be achieved not only through refractive index (or dielectric permittivity) modulation, as was emphasized in Chapter 5, but also through modulation of gain or loss. Based on the type of modulation, DFB lasers are classified into index-coupled and gain-coupled. However, it is very common to have mixed, index/gain coupling, which is likely to be the case for our DFB. Let us consider a purely index-coupled

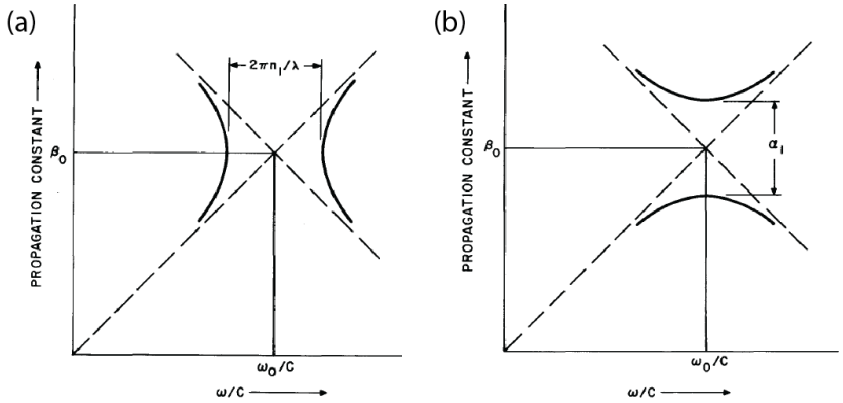

Figure 6.3: (a) Dispersion diagram for index modulation with no loss or gain. (b) Dispersion diagram for gain modulations with average loss or gain. Reprinted from [119].

DFB. The dispersion curves, solutions to Eq. 6.6 for a gain-free ($\alpha = 0$) structure with a real κ, are shown in Figure 6.3. The stop band of width 2κ is centered at the Bragg frequency ω_0, where the wave propagation is forbidden. However, γ is real and points to existing evanescent waves at the Bragg frequency.

In case of a DFB structure with non zero gain ($\alpha > 0$, κ real), the dispersion curve evolves from the original pattern with 2κ-wide stop band (Figure 6.3, a) to a progressively narrower stop band, and eventually, an X shape pattern (Figure 6.4, a), where $Im(\gamma)\kappa$ is plotted as a function of δ/κ for various values of the parameter α/κ.

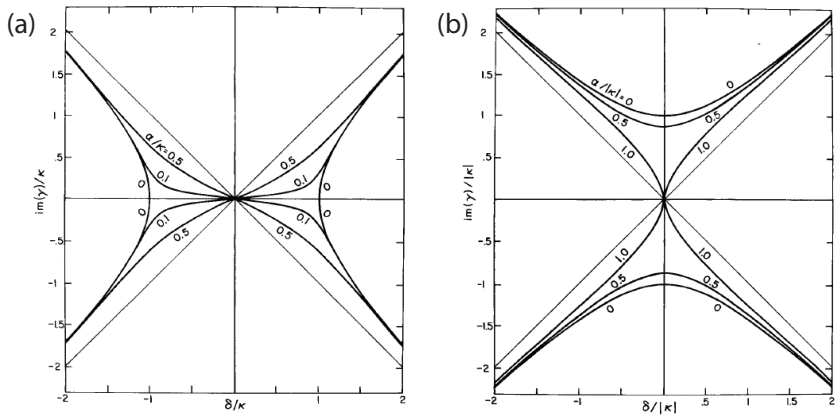

Figure 6.4: (a) Dispersion diagram for index modulation for various gain to coupling parameter ratios. (b) Dispersion diagram for gain modulation for various gain to coupling parameter ratios. Reprinted from [119].

Finally, let us examine the dispersive behavior of a purely gain-coupled DFB structure (κ is imaginary) with zero average gain ($\alpha = 0$) shown in Figure 6.3, b. In contrast with purely index coupled DFB case, there is no frequency stop band. Instead, there is a propagation constant stop band, still centered at the Bragg frequency. Figure 6.4, b shows the gradual evolution of the dispersion curve into an X shaped dispersion curve as the average gain increases.

6.3 Lasing threshold calculation

We used CMT to design the hybrid III-V/Si DFB and estimate the resonant frequency and associated threshold gain. The schematic drawing of the hybrid III-V/Si DFB structure, cross-section and transverse modes, simulated in COMSOL, are shown in Figure6.5 .

First, we calculated the coupling coefficient for this DFB, using the method described in Chapter 5. The κ values are $280\,\mathrm{cm}^{-1}$ and $80\,\mathrm{cm}^{-1}$ for TM-like and TE-like modes, respectively. In Chapter 5 we also showed that significant overlap of E_z optical field component with the corrugated portion of the guide plays an important role in dispersive characteristics of the waveguide. The permittivity distribution in the real waveguide cross-section (Figure 6.5, e,f) and the hypothetic average waveguide cross-section are shown in Figure 6.5, d. To perform this cal-

culation we ignored refractive index change due to the variation in the injected carrier concentration, since CMT threshold analysis is valid only at transparency, as we have mentioned at the beginning of current chapter. Now we know the

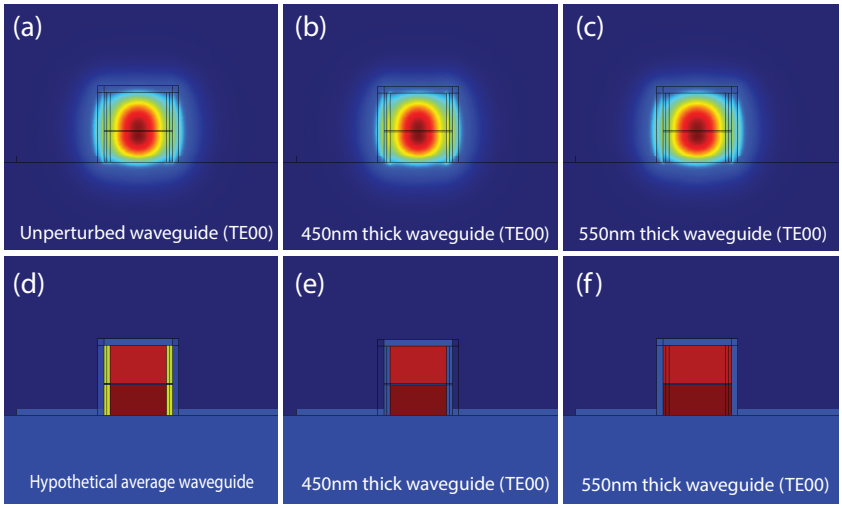

Figure 6.5: (a) Unperturbed average guide, TE-like mode; (b) TE-like mode of a 450 nm wide waveguide, corresponding to the narrow section of the grating; (c) TE-like mode of a 550 nm wide waveguide, corresponding to the wide section of the grating; (d) permittivity distribution of the hypothetical average waveguide (e) permittivity distribution in the narrow section of the grating; (f) permittivity distribution in the wide section of the grating.

coupling coefficient κ, grating length and complex $\Delta\beta$ values for longitudinal modes existing in the structure depicted in Figure 6.6, a. Thus, we can find the normalized threshold gain $\mathrm{Im}(\Delta\beta L)$ for various propagating modes (see Figure 6.2). Note, that threshold gain value is different tor TE and TM modes, because their normalized coupling coefficient κL is different while the rest of the parameters are the same. This is because, while their transverse E_{xy} fields yield the same transverse coupling coefficeint component, the longitudinal field components E_z are distributed very differently in case of TE-like (Figure 6.6, c) and TM-like (Figure 6.6, d) modes, as we mentioned in the previous chapter. To estimate the modal gain, i. e., material gain required for the mode to overcome optical losses in the grating and reach threshold, we use the following relationship between the

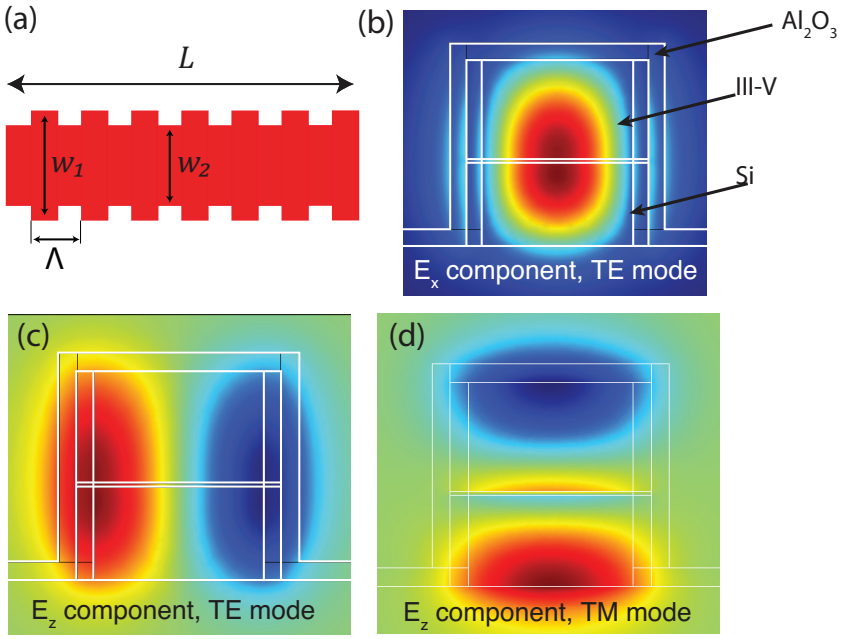

Figure 6.6: (a) Schematic of a sidewall modulated DFB laser, top view, where Λ is the grating period, ω_1 and ω_2 are the different waveguide widths; (b) Simulated E_x component of a TE-like mode; Simulated E_z component of a fundamental TE-like mode (c) and TM-like mode (d) in a 500 nm wide and 550 nm tall III-V/Si waveguide with 250 nm silicon layer, 300 nm bulk InGaAsP layer.

normalized gain and modal gain:

$$\Gamma g - \alpha_{int} \propto Im(\Delta\beta_m) \tag{6.11}$$

where α_{int} are internal losses, g is the material gain coefficient and Γ is the mode confinement factor in the gain (or gain/mode overlap). Gain/mode overlap Γ in our DFB structure (Figure 6.6, b) is close to 0.5 for bulk InGaAsP gain and 0.2 for multiple quantum well (MQW) InGaAsP gain. If we neglect losses, the material gain required to reach lasing threshold in 100 µm long grating is estimated to be 400 cm^{-1} for bulk InGaAsP and 1000 cm^{-1} for MQW InGaAsP. Both of these values are realistic, since gain in bulk and MQW III-V compounds is known to be as high as thousands of cm^{-1} [39, 121, 122].

Chapter 7

Wafer bonded distributed feedback laser with sidewall modulated Bragg gratings

Modern communication systems place rapidly growing requirements on information processing speed, as well as on the manufacturing and operation cost of their components and networks. One way to meet these needs is to supplement electronic circuits with photonic integrated circuits (PICs). Currently, silicon serves not only as a foundation for CMOS technology, but also as a primary material for passive photonics, due to its numerous advantages for on-chip light transport. However, enabling the full range of functionalities (e.g., switching, routing, lasing, modulation, and detection) on a single module requires the use of other materials [123–125]. In particular, III-V compound semiconductors are advantageous for construction of active optical elements and logic devices, owing to their direct, widely ranging energy bandgap and high carrier mobility.

Today most photonic circuits with active components are implemented via flip-chip bonding of independently fabricated active components to a silicon-based passive photonic circuit. This approach is complex, time consuming, and has tight alignment tolerances (< 0.5) for a minimal ($\approx 1\,\mathrm{dB}$ per link) coupling loss for microscale components [126–129]; for nanoscale components, the alignment restriction becomes impractical. An alternative way to integrate dissimilar material

systems is their monolithic integration through epitaxial growth or wafer bonding prior to the PIC nanofabrication. Despite the remarkable progress with growing epitaxial III-V semiconductor layers on silicon [9, 46, 130], the dissimilar crystal structures of these materials make it extremely challenging to grow sufficiently large areas of III-V on Si for PIC manufacturing [45]. This makes a second alternative approach, wafer bonding, the most amenable for dense, large-scale monolithic integration at present.

Compared to a number of existing wafer bonding techniques [73], plasma assisted wafer bonding [67] has advantages of scalability, low temperature and directness. Furthermore, it has already been successfully used to demonstrate a variety of SOI-compatible evanescent optoelectronic devices [131]. We combine plasma-assisted wafer bonding with a self-aligned fabrication approach [65], which requires a single resist mask to etch both III-V and silicon layers and offers the benefit of simple, alignment-free fabrication. The latter is very important when device dimensions approach the alignment resolution limit of commercial mask aligners.

In this work, we use self aligned sidewall modulated Bragg gratings [117] for optical feedback in a compact III-V/Si distributed feedback laser (Figure 7.1(a,c)). High mode confinement factor in the gain layer of sub-micron cross-section waveguide is a potential way to reduce the threshold and enable lasing in hybrid III-V/Si lasers [56, 132, 133]. We show the high degree of compactness enabled by our design and fabrication approach by demonstrating lasing in a 100 µm long optically pumped wafer bonded distributed feedback (DFB) laser.

A schematic drawing of the designed optically pumped laser structure is presented in Figure 7.1(a, c). The TE-like transverse optical mode of the composite waveguide is evenly distributed between the silicon and III-V layers (Figure 7.1(b)). By choosing the III-V/Si layer thickness ratio, we can control the gain-mode overlap, thus providing more effective interaction of the mode with the gain material. With the ability to produce high gain-mode overlap, stimulated emission can be reached either at reduced threshold or with smaller device footprints, depending on the design.

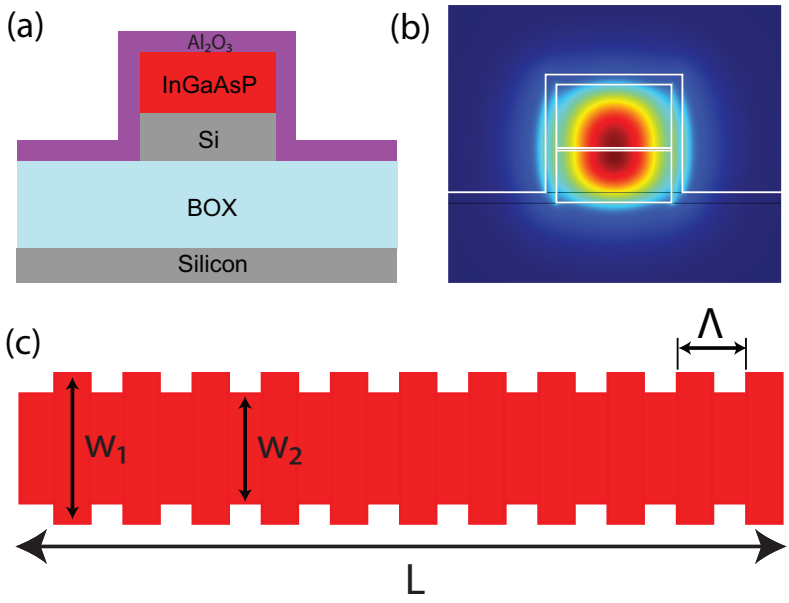

Figure 7.1: III-V/Si hybrid DFB laser design: schematic drawing of a III-V/Si DFB laser resonator with vertical sidewall modulated Bragg gratings – cross-section (a) and top view (c); (b) finite element simulation (COMSOL) of a fundamental TE-like mode for a 500 nm wide and 550 nm tall III-V/Si waveguide with 250 nm silicon layer, 300 nm InGaAsP MQW layer and 50 nm Al_2O_3 cladding.

We use coupled mode theory [119] to estimate locations of the stop band of the grating and its adjacent minima, where the lasing is likely to occur. Here we neglect the gain coefficient of the III-V layer and assume a passive Bragg grating with effective indices extracted from cross-sectional finite element simulations in COMSOL (Figure 7.1(b)). This simple model is sufficient for initial estimation of the grating behavior. The reflectivity of a passive Bragg grating can be expressed as follows [118]:

$$R = \frac{\kappa^* \kappa \sinh^2 sL}{s^2 \cosh^2 sL + (\Delta\beta/2)^2 \sinh^2 sL} \tag{7.1}$$

where $s = \sqrt{|\kappa|^2 - (\Delta\beta/2)^2}$, L is the grating length and $\Delta\beta$ is the detuning of the propagation constant from the stop band center (Bragg wavelength). The coupling coefficient κ for the fundamental TE mode of an unperturbed waveguide is defined by

$$\kappa = \frac{\pi}{2\lambda_0} c \int \mathbf{E_1}^* \Delta\varepsilon \mathbf{E_2} dx dy \tag{7.2}$$

The electric fields $\mathbf{E_1}$ and $\mathbf{E_2}$, as well as the first order dielectric perturbation tensor $\Delta\varepsilon$ were extracted from COMSOL simulations. We calculate the κ for $\lambda_0 = 1,550\,\text{nm}$ and the reflectivity for a range of $\Delta\beta$ values between approximately -7×10^5 and $8 \times 10^5\,\text{m}^{-1}$.

The fundamental TE mode of a composite waveguide is shown in Figure 7.1(b). The estimated value of the coupling coefficient for a 100 µm long Bragg grating with a period of $\Lambda = 272\,\text{nm}$, modulation of $w_1 = 545\,\text{nm}$ and $w_2 = 455\,\text{nm}$, gain layer thickness of 300 nm, silicon layer thickness of 250 nm and 50 nm thick Al_2O_3 cladding is $\approx 230\,\text{cm}^{-1}$. We find the stop band bandwidth to be 8 nm and the two closest reflection minima to be at 1,543 nm and 1,554 nm. The confinement factor of the mode inside the gain region for this design is close to 0.5, assuming bulk InGaAsP as a IIIV material for computational simplicity. The high achievable confinement factor allows us to build compact lasers through efficient use of the optical mode. The threshold gain is found to be $\approx 150\,\text{cm}^{-1}$ for the lowest order longitudinal mode from the resonance condition for a simple DFB laser [120]. This gain value can be achieved in bulk InGaAsP [134], which is known to exhibit gain coefficients of $\approx 200\,\text{cm}^{-1}$ at room temperature.

For experimental demonstration we choose InGaAsP with multiple quantum wells (MQW) as a gain material. Compared to bulk IIIVs, gain performance can be greatly enhanced in a well optimized IIIV MQW structure [121, 135, 136]. On the other hand, the optical field confinement factor in the wells is lower than in bulk gain, which would increase the threshold. Comprehensive optimization of these parameters for minimum threshold gain can become rather cumbersome and is outside of the scope of this paper.

Composite InGaAsP/Si laser structures were fabricated from an InGaAsP MQW layer bonded to an SOI chip. The schematic drawings of different fabrication steps are shown in Figure 7.2 (a,b). The MQW InGaAsP/InP wafer was grown by OEpic Semiconductor, Inc. This gain layer is comprised of 9, each 10 nm thick, wells (1.6Q $In_xGa_{1-x}As_yP_{1-y}$, $x = 0.56$, $y = 0.938$ with bandgap wavelength of 1,600 nm (1.6Q)) embedded in 10, each 20 nm thick, barriers (1.3Q $In_xGa_{1-x}As_yP_{1-y}$, $x = 0.734$, $y = 0.571$ with bandgap wavelength of 1,300 nm

(1.3Q)), epitaxially grown on an InP substrate, bringing the total thickness of the gain layer to ≈ 300 nm (the structure is summarized in Table 7.1). This InGaAsP MQW active layer was bonded to an SOI chip with a 250 nm thick top silicon layer via low temperature plasma assisted wafer bonding. This wafer bonding process, as described below, is based on the III-V-to-Si bonding procedure developed by Liang et al [76].

Table 7.1: Multiple quantum well 300nm thick InGaAsP/InP epitaxial structure.

Name	Material	Thickness (Å)	No. of layers
Capping layer	InP	100	1
Active region	1.3Q $In_xGa_{1-x}As_yP_{1-y}$	200	9
	1.6Q $In_xGa_{1-x}As_yP_{1-y}$	100	9
	1.3Q $In_xGa_{1-x}As_yP_{1-y}$	200	1
Substrate	InP	325 µm	

The wafer bonding was performed for a quarter of a 2-inch InGaAsP/InP wafer and a SOI chip of ≈ 10 cm^2 area. Prior to the wafer bonding, we etched vertical outgassing channels (VOC) in the top silicon layer of the SOI chip [76]. The purpose of the VOC is to facilitate the evacuation of gaseous byproducts from the InGaAsP/Si interface during the bonding process. We used NR71-1500 PY negative tone photoresist to form the photolithographic mask for the channels. The silicon layer was then etched in a Oxford P100 reactive ion etch (RIE) tool using a CHF_3:SF_6 chemistry with the following settings: CHF_3 and SF_6 flows are 15 and 100 sccm, respectively; RIE: 30 W, ICP: 1200 W, Pressure: 15 mTorr, Temperature: 20°C , Helium pressure: 10 Torr.

Extremely thorough cleaning procedure of the both wafers is essential for a successful wafer bonding. The low temperature bonding starts with very low power ultrasonication in acetone and isopropanol (IPA), followed by a thorough DI water rinse, to eliminate particles from the bonding surfaces and dissolve any

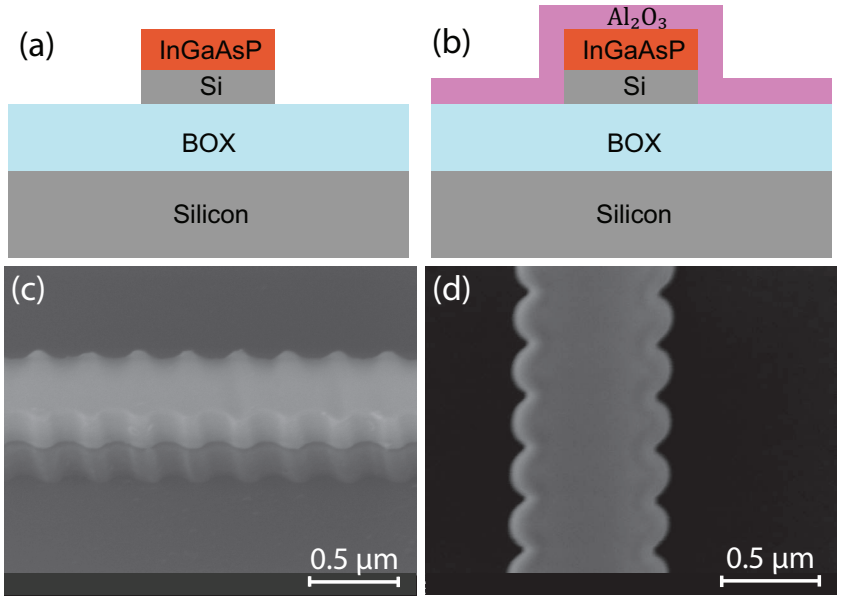

Figure 7.2: (a,b) - schematic steps of fabrication process; (c,d) are the SEM images of the Bragg grating after two-step RIE and after Al_2O_3 layer deposition by atomic layer deposition (ALD), respectively.

remaining organics. Next, the surfaces are to be stripped of native oxides, organic, and ionic contaminations. This is performed on the InGaAsP/InP chip using ammonia hydroxide (NH_4OH) for 5 minutes, and on the SiO_2/Si chip using freshly mixed H_2SO_4:H_2O (3:1) solution for 5 minutes. The chemical clean is followed by a quick water gun rinse and drying in N_2 flow. Next, both chips are dipped in 1 % HF solution for 20 seconds to remove native oxides. After cleaning, both chips undergo O_2 plasma surface activation in a Trion RIE chamber with 20 mTorr pressure, 30 sccm O_2 flux and 50 W RF power for 45 seconds. The oxygen plasma treatment is immediately followed by a brief rinse in DI water to passivate the active surfaces with hydroxyl (–OH) groups. The water flow also removes any new particles that may have accumulated during the plasma activation. Next, nitrogen flow-dried chips are manually mated. The Van der Waals force between the –OH groups promotes spontaneous mating of activated surfaces. The pair is annealed for 17 hours at 300°C in an oven under atmospheric pressure to form strong covalent bonding and facilitate evacuation of the H_2O and H_2 byproducts through the VOC into BOX (SiO_2) layer, and through the BOX away from the

InGaAsP/Si interface. Finally, the InP carrier substrate is selectively etched via immersion into 38% HCl at room temperature, untill reaction is terminated by the InGaAsP etch stop layer, to obtain the composite InGaAsP/SOI structure.

The next step is to perform the self-aligned etch to create the Bragg grating structures on the bonded chip. This is done through a double step reactive ion etch (RIE), which has to be carried out on the gain layer and SiO_2 using appropriate etching chemistry for each of the two materials. To create the initial mask, E-beam lithographic processing with Raith50 writer is performed on hydrogen silsesquioxane (HSQ) negative resist. This is followed by the two-step RIE to form the top (III-V) layer and bottom (Si) layer of the Bragg grating. First, the 300 nm thick InGaAsP MQW layer is dry etched in CH_4:H_2:Ar (4:40:20 sccm) chemistry. Then the Si layer undergoes CHF_3:SF_6 RIE, using the same recipe as for the VOC etching described above, to etch the silicon layer using the gain layer as a mask. Figure 7.2(a) depicts a schematic drawing of the structure after both of these steps are performed. Next the sample is treated in microwave oxygen plasma (Tepla 100) to eliminate polymer buildup. An SEM image of a clean laser sample after this cleaning step is presented in Figure 7.2(c). Lastly, atomic layer deposition (ALD) of 50 nm thick Al_2O_3 is carried out using a Beneq TFS200 for thermal management (Figure 7.2(b) shows a diagram of the resultant structure). An SEM image of the Bragg grating after the aluminum oxide deposition is shown in Figure 7.2(d).

We used a standard micro-photoluminescence setup for optical characterization of the lasers. For optical pumping we employed a 1,064 nm pulsed fiber laser (SPI G3) with a repetition rate of 300 kHz and 12 ns pulse width. The pump beam was focused down to an approximately $20 \times 570\,\mu m^2$ spot size (FWHM) at the sample plane, using a combination of cylindrical and spherical lenses. This spot size calculation includes the effect of the pump beam's quality factor (M^2) of 1.84 (provided by the laser manufacturer). The edge of the sample was imaged onto an infrared (IR) InGaAs camera (Indigo Alpha NIR) through a 20× IR-coated microscope objective and a double 4–f imaging system. The output signal was collected through the same objective and passed through a pump filter (1064 nm Semrock

RazorEdge longpass), onto either the IR camera or a monochromator (Spectral Products DK480). Both total power measurements for the light-light curves and high resolution measurements in the lasing operation mode were performed with the monochromator, which has a resolution of 0.35 nm and is equipped with a cooled InGaAs detector in lock-in detection configuration. All measurements were performed at room temperature.

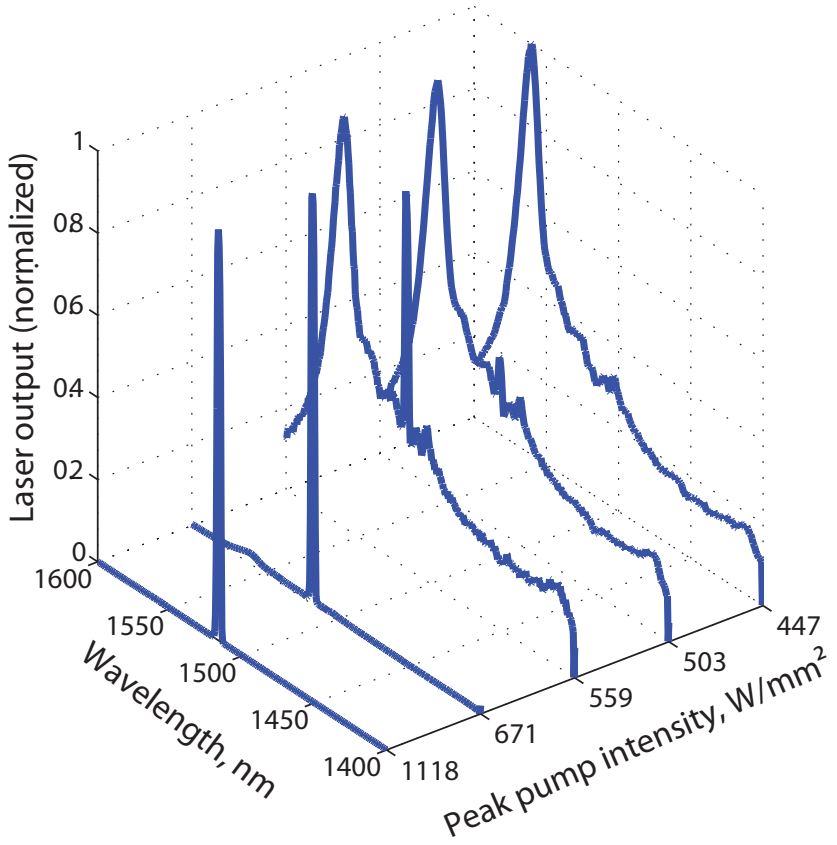

Figure 7.3: Spectral evolution, with final peak wavelength at 1,515 nm.

The optical measurements results for the DFB laser with design physical dimensions described in Sec. II are shown in Figure 7.3 and 7.4. The actual structure may slightly differ from the design due to fabrication inaccuracies. The plot in Figure 7.3 represents spectral evolution from a broad-band photoluminescence at lower pump powers through amplified spontaneous emission (ASE) to a single narrow peak at 1,515 nm wavelength, as the power increases. The width of the peak at the highest pump powers was limited by the monocromator resolution

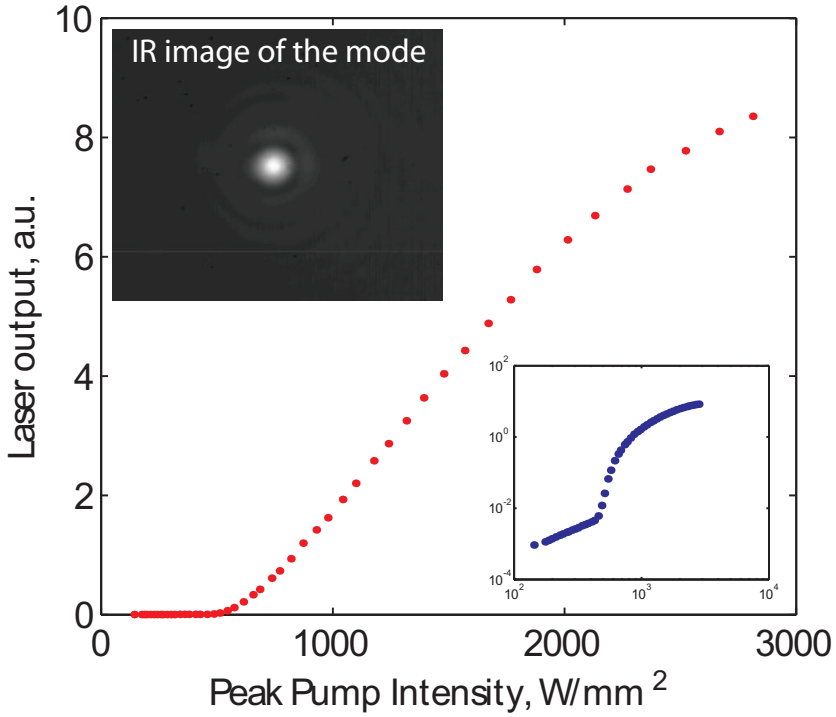

Figure 7.4: The laser light-light curve in linear and logarithmic (lower right inset) scale with the IR image (upper left inset) of the lasing mode; lasing threshold is at 530 W/mm^2.

of 0.35 nm. We observed appearance of coherence rings around the output mode on the IR camera (Figure 7.4, upper left inset), which is one of the signatures of stimulated emission. We measured the extinction ratio between the TE-like and TM-like modes to be higher than 20 dB.

To extract the lasing threshold, we performed light-light measurements (Figure 7.4) and analyzed the corresponding logarithmic scale plot (Figure 7.4, lower right inset). The S-shaped log-log curve is characteristic of laser behavior. In the ideal case (when the recombination only occurs through radiative excitonic transitions), the first and last sections of the curve are linear with slopes close to 1. We found the threshold peak pump intensity to be around 530 W/mm^2, assuming lasing threshold to be at the middle point of the ASE section. For the III-V/Si DFB laser, the PL and stimulated emission sections exhibit varying slope, which deviates from unity. The superlinear behavior of the light-light characteristic in these regions points to various cavity and material losses, including scattering losses,

surface recombination, and non-radiative recombination on the III-V/Si interface. This is a fairly common for a realistic nanoscale structure [19,137], due to the high density of defects per volume.

To summarize the results, we demonstrated a compact optically pumped III-V/Si DFB laser with sidewall modulated Bragg gratings. The laser structure is 100 µm long with average waveguide width of 500 nm and a total waveguide height of 550 nm. We employed plasma-assisted wafer bonding and a self-aligned fabrication approach in making the laser, a process that does not require any lithographic alignment with its associated alignment losses. The flexibility of a sidewall modulated grating design can also enable the development of low-threshold hybrid DFB lasers, with larger physical size. Work on an electrically pumped version of the laser, as well as coupling of the lasing mode to a silicon waveguide, is underway.

This work was supported by the Defense Advanced Research Projects Agency (DARPA), the National Science Foundation through CIAN NSF ERC under grant #EEC-0812072, the Oracle Labs, the Cymer Corporation, and the U.S. Army Research Office. The fabrication was performed at UCSD Nano3 facilities. The authors would like to thank Felipe Vallini, Michael Kats and Maziar Nezhad for helpful discussions.

Chapter 7, in full, is a reprint of the material as it appears in "Wafer bonded distributed feedback laser with sidewall modulated Bragg gratings," O. Bondarenko, Q, Gu, J. Shane, A. Simic, B. Slutsky, and Y. Fainman, *Applied Physics Letters* 103, 043105 (2013). The dissertation author was the primary co-investigator and coauthor of this paper.

Chapter 8

Future work and conclusion

8.1 Laser-to-waveguide coupling

Efficient light routing between passive and active devices in a photonic chip requires a coupler, where the mode is pulled into a silicon waveguide from the active section. The function of a coupler is to transfer the mode from the III-V region of a hybrid III-V/Si structure to the silicon waveguide adiabatically to prevent excitation of other transverse modes. The most commonly used coupler in hybrid integrated circuits is a conventional taper [138].

In this work we propose an alternative coupler design, suitable for the cases when photolithographic alignment to shape the traditional taper coupler is not an option. Usually the error of a commercial mask aligner becomes a problem when the pattern features are on sub-micron scale. Our design of an adiabatic taper with evenly beveled edges throughout the entire length of the coupling region allows effective coupling of the optical mode to a silicon waveguide (Fig. 8.1). Finite element simulations (FEM) in COMSOL were performed for different waveguide widths and the results are presented in the bottom row of Fig. 8.1. The simulations show that for wider waveguides a large portion of the mode interacts with the gain (top part of the waveguide). As the waveguide narrows, the mode becomes confined to the lower silicon waveguide. This suggests a potential way to design the resonator with a large gain/mode overlap with coupling to a conventional single mode silicon waveguide (approximately 500 nm wide and 250 nm thick). Therefore,

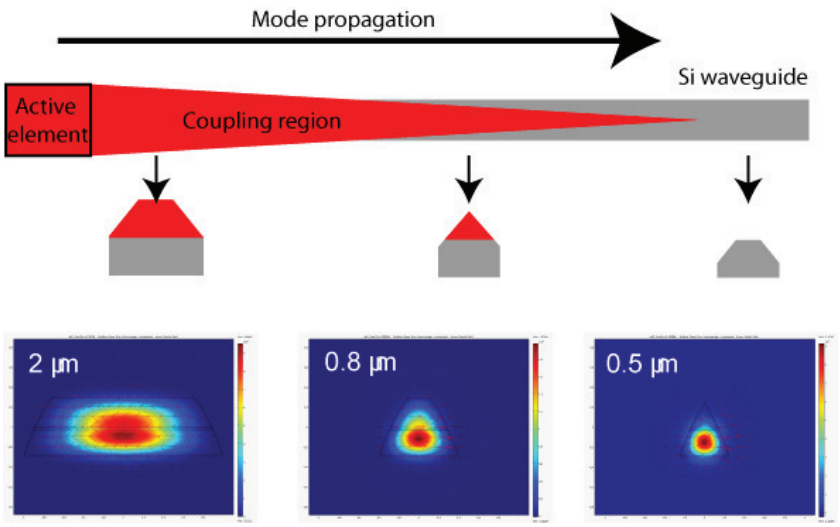

Figure 8.1: On the top: schematics of the III-V/Si beveled adiabatic taper coupler with cross-sections showing decreasing coupler widths. On the bottom: finite element simulations (COMSOL) of a fundamental TE-like mode for beveled waveguides with different widths.

the main advantages of the proposed coupler design are: 1) adiabatic nature of the coupler, both vertically and horizontally, which minimizes the losses compared to the commonly used evanescent coupling approach; 2) the active element can be designed with relatively large mode/gain overlap.

To verify the feasibility of our taper design, we performed ion-milling process using test silicon and III-V/Si structures. The beveling effect, shown in the scanning electron microscope (SEM) pictures (Fig. 8.2), is achieved through an extended (30-50 min) O_2 reactive ion etch (RIE) treatment. For this processing we use Trion RIE tool with elevated O_2 gas flow and chamber pressure of 100 sccm and 100 mT, respectively. The RF power was set to 150 W. SEM images of a silicon waveguide and a test composite Si/InGaAsP structures after 45 minutes of RIE are presented in Fig. 8.2 (a and b), respectively. This process employs concentrated oxygen plasma to achieve the ion-milling effect. From Fig. 8.2(a, b) InGaAsP appears to respond to the treatment faster than silicon due to the difference in mechanical properties. Since this process is physical, rather than chemical, it may be possible to replace O_2 gas with Ar, for example.

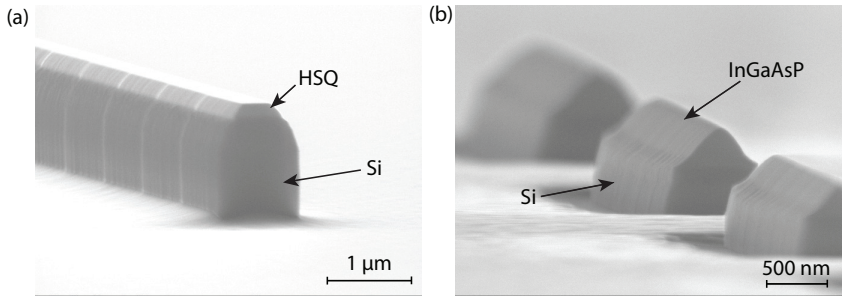

Figure 8.2: SEM pictures of ion-milled test structures: (a) 500 nm wide and 550 nm thick silicon waveguide with HSQ mask on top after 45 minutes; (b) InGaAsP/Si test structures of variable width with 250 nm thick Si bottom layer and 300 nm thick InGaAsP top layer after 45 minutes.

8.2 Electrically pumped III-V/Si laser

The next logical step of this project is an electrically pumped implementation of the laser that can be later used for on-chip optical and quantum information processing circuits. The proposed electrically pumped device layout is depicted in Figure 8.3, a and b. We propose to use AlGaInAs quantum well structure [52] due to its superior thermal properties compared to InGaAsP [39], which may be critical for an electrically pumped laser. We would like to use self-aligned fabrication approach for electrically pumped laser. Thus, a possible route of contact fabrication is: (1) deposition top p-contact metallization on the top of the structure (2) etching through the extended sidewall corrugations to the n-doped layer and deposition of metallization to create Ohmic contact at the bottom. Fang et al [104] use Ni/AuGe/Ni/Au alloy to create n-contact and Pd/Ti/Pd/Au for p-contacts, the approach we can adapt for this design.

8.3 Optimization of laser design

Optimization of the lasing threshold of DFB laser, as well as control of the discrimination between fundamental and higher-order longitudinal modes, requires the knowledge of the following key parameters: coupling coefficient κ of the grating, gain volume interacting with the optical field and losses in the system. Coupling coefficient can be maximized in the DFB structures by tuning the waveguide the

width, height and modulation depth [39]in the waveguide, thereby reducing the lasing threshold.

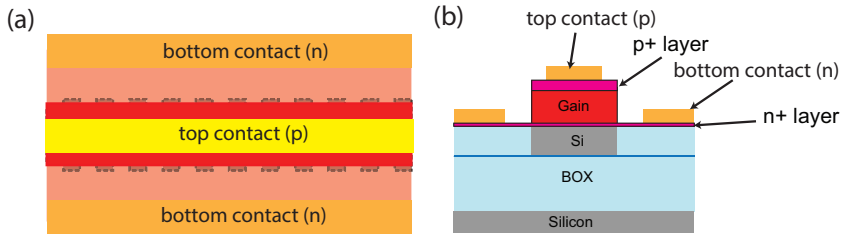

Figure 8.3: Proposed schematics of an electrically pumped IIIV/Si laser with sidewall modulated gratings.

We have already discussed theoretical approaches to calculation of coupling coefficient and threshold gain in Chapters 5 and 6. To evaluate the accuracy of the theoretical approach to estimation of the coupling coefficient, we should compare it with experimental measurement of the coupling coefficient. To measure coupling coefficient, we need to observe the wavelength-dependent transmission of the grating and fit the spectrum with the theoretical expression for transmission with coupling coefficient as a fitting parameter [117]. We designed and built an optical characterization setup capable to perform transmission measurements in waveguides with gain (Chapter 2).

8.4 Conclusion

In this dissertation we discussed state of the art hybrid integration techniques and III-V/Si active components with an emphasis on hybrid distributed feedback (DFB) lasers for telecom applications. We demonstrated several ultra-compact lasers for high-density integration with silicon photonics. We developed fabrication and characterization methods for vertically and edge emitting optically pumped lasers, as well as characterization methods for transmission measurements in waveguides with gain. We presented the first room temperature subwavelength metalo-dielectric laser, uniquely suitable for high-density packaging for optical interconnects due the tight mode confinement in metalo-dielectric resonator. Further, we demonstrated a metalo-dielectric nanolaser on silicon, showing the fea-

sibility of its integration with silicon platform. Finally, we realized ultracompact edge emitting DFB and DBR lasers using post-bond fabrication approach. We outline design challenges associated with the nanoscale device coupling to a silicon waveguide and its electrical pumping.

Appendix A

Distributed Bragg reflector laser

We used a distributed Bragg reflector (DBR) design in our first implementation of an edge emitting wafer bonded laser. It consisted of two DBR grating mirrors with a straignt gain section in the middele, forming a Fabri-Perot cavity. The device was fabricated with a post-bond approach, similarly to the DFB laser, discussed in Chapter 7. The laser in schematically depicted on the upper right inset of Figure A.1. The average waveguide width in both Bragg mirror sections, as well as the width of the resonator section is 750 nm. The narrow part of the Bragg mirror is 500 nm and the wide part is 1000 nm. The number of periods on the left mirror is 40; on the right - 25; grating period Λ is 250 nm. Fabri-Perot resonator section is 40 µm long. The total length of this device is less than 60 µm.

Optical characterization was carried out on the microphotoluminescence setup, configured for measurements of a vertically emitting laser, as described in Chapter 2. We used 2× Mitutoyo IR-coated microscope objective to focus down to a big spot size and cover the area of ≈100 µm. We collected the signal with a multimode fiber and passed the signal to the monocromator. Middle inset on the right of Figure A.1 shown the IR camera image of the lasing sample. The signal is emitted from the both sides of the structure, which points to the Fabri-Perot effect in the edges of the sample, as opposed to the Bragg mirrors. The bottom right inset of Figure A.1 shows a spectrum measured with monochromator. The linewidth is near or below 2 nm.

To optically characterize this laser we used wide grating and short inte-

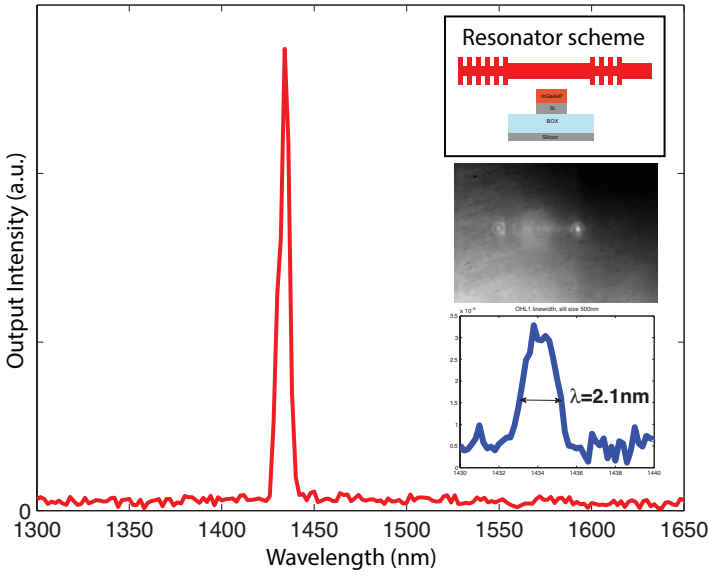

Figure A.1: Optical measurements results of a hybrid III-V/Si DBR laser.

gration time, with the purpose of the fast total monochromator scan time, as the laser had poor stability under optical pumping. We observed rapid degradation of signal intensity and lasing peak width within only a few minutes. Unstable behavior of the sample prevented us from performing a thorough characterization. Additionally, this setup configuration was not optimazed for measurements of thin and long edge emitting lasers, - both pumping and signal collection were expremely inefficient.

Potential reasons for the fast signal degradation and poor device performance in include unoptimized measurement setup (which possibly caused excessive heating) and unoptimized design of the laser itself. The modulation depth of DBR mirrors is too high, wich is very likely to introduce substantial scattering losses.

Appendix B

Simulations

The resonant modes and gain thresholds were found using COMSOL's 2-D and 3-D eigenmode solvers. The analysis of pump penetration and absorption in the cavity was done using the scattered field formulation for plane wave illumination in COMSOL. The optical constants of the metals were obtained from Palik [96] and Johnson and Christy [93]. The optical constants of the MQW gain medium were measured using an infrared thin film measurement system (Filmetrics 20®) and were in good agreement with values cited in the literature [139].

Since the lasers are designed to be optically pumped, pump penetration into the core is an important factor to be considered, given the small size of the input aperture. For pumping we used a 1,064 nm pulsed fiber laser operating at 300 kHz repetition rate and 12 ns pulse width. The pump beam was delivered to the samples using a $\times 20$ or $\times 50$ long working-distance objective which also collected the emitted light. In order to estimate the amount of pump power absorbed by the core, a full 3-D finite element analysis was carried out over a range of core sizes (with fixed dielectric shield thickness), assuming illumination with a plane wave at a pump wavelength of 1,064 nm and a peak illumination intensity of 1 kW/mm^2 (Figure B.1a, solid blue curve). As shown, the total power absorbed in the core exhibits oscillations at small core sizes, which flatten out as the core size increases. These oscillatory features are also present when a perfect conductor is substituted for the aluminum layer (Figure B.1a, dashed blue curve), eliminating the possibility that this phenomenon is a manifestation of surface plasmon related effects (e.g.

extraordinary transmission through a metallic aperture [140]) and indicating that the resonant behavior is due to simple resonance of the pump inside the metallic cavity (which is stronger for smaller core sizes, since a smaller proportion of the core is absorptive). Interestingly, for smaller core sizes a significant proportion of the pump power is funneled through the silica layer and absorbed through the sidewall of the gain core (Figure B.1b), which is an indirect benefit of using the shield layer. The red curve in Figure B.1a shows the generated carrier density for a peak pump intensity of 700 W/mm^2 and a (rectangular) 12 ns pump pulse width.

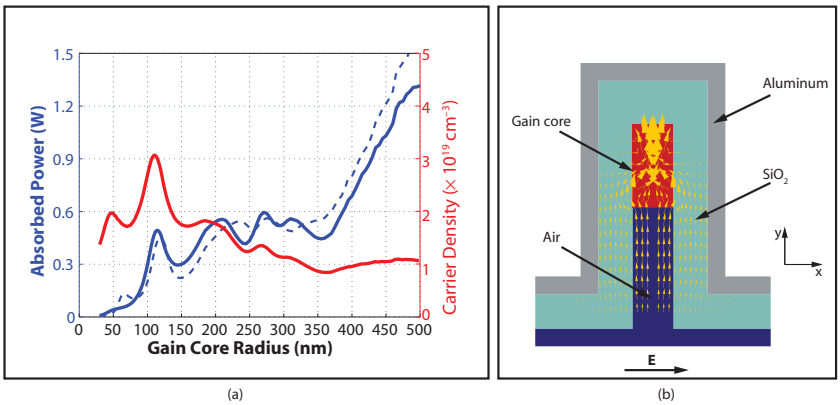

Figure B.1: **(a)** Results of 3-D FEM simulations showing the absorbed pump power in the gain core as the size of the core is varied (blue curves). The core height is 480 nm and the solid and dashed curves correspond to aluminum and perfect conductor metal shields, respectively. The pump wavelength is 1,064 nm, polarized in the x direction and the incident intensity is assumed to be 1 kW/mm^2. The red curve shows the estimated threshold carrier density assuming 12 nm pulses. The pump power is assumed to be the threshold value of 700 W/mm^2. **(b)** Pump power flow (yellow arrows) showing how the dielectric shield funnels the pump beam through the sides of the gain disk. The core radius in this case is 116 nm, corresponding to the first absorption peak for an aluminum shell (solid blue line in **(a)**)

Estimation of the carrier density was performed using the rate Equation B.1 assuming a carrier dependent recombination lifetime $\tau_r = (B_0 N_c)^{-1}$, where N_c is the carrier density, $B_0 = 1 \times 10^{-10}$ cm^3/s [141] and $\phi_0(t)$ is the incoming photon flux signal, calculated from the pump peak power.

$$\frac{dN_c(t)}{dt} = \phi_i(t) - B_0 N_0^2(t) \tag{B.1}$$

The refractive index drop due to carrier effects was estimated using results derived in [97]. Depending on the carrier density level, the effects of band filling, bandgap shrinkage and free carrier absorption can induce a positive or negative refractive index change, depending on the wavelength and the dominating process(es). For InGaAsP at 1.55 µm and for the high carrier densities estimated in our case (about $1.2 \times 10^{19}\,\mathrm{cm}^{-3}$ for a core diameter of 520 nm), the combination of band filling and free carrier absorption dominates the bandgap shrinkage effect, resulting in an estimated net drop of approximately 0.1 in the refractive index [97].

Another phenomenon that may contribute to refractive index decrease is the compressive pressure exerted by the sputtered aluminum shield after it cools down to room temperature. Even though a 70 nm layer of aluminum is sufficient to create optical confinement, the actual sample was covered with an additional one micron layer of aluminum for better heat sinking. This metal layer will have a larger thermal contraction than the silica/InGaAsP core and will exert compressive pressure on it, which will result in a drop in the InGaAsP refractive index. However, we believe this effect to be negligible in our structures. As the device cools, the difference in thermal contraction (24 ppm/°C for aluminum vs. 5 ppm/°C for both silica and InGaAsP) is accommodated partly by compression of silica/InGaAsP core, and partly by compression of nearby aluminum. Even if all of the compression occurred in the core, it would amount to just 0.0019 for a 100 °C drop in temperature. Assuming the Young modulus of the core to be nominally $E = 70\,\mathrm{GPa}$, the stress corresponding to this small compression would be less than 0.14 GPa, and the effect of this small stress on the refractive index less than 0.004 [142, 143].

Appendix B, in part, or in full, is a reprint of the material as it appears in "Room-temperature subwavelength metallo-dielectric lasers," M. Nezhad, A. Simic, O. Bondarenko, B. Slutsky, A. Mizrahi, L. Feng, V. Lomakin, and Y. Fainman, *Nature Photonics*, vol. 4, no. 6, pp. 395–399, 2010. The dissertation author was the primary co-investigator and coauthor of this paper.

Appendix C

Purcell factor estimation

Cavity-induced enhancement of spontaneous emission into a resonant mode relative to spontaneous emission in bulk material (the Purcell factor) can be estimated as [144]:

$$F_{cav} = \frac{Q\lambda_{cav}^3 \zeta}{4\pi^2 n_{bulk}^3 V_{\mathit{eff}}}, \quad V_{\mathit{eff}} = \frac{1}{n_{bulk}^2} \iiint n(\mathbf{r})^2 |\mathbf{f}(\mathbf{r})| d^3\mathbf{r}, \quad \zeta = \frac{|\mathbf{d} \cdot \mathbf{f}(\mathbf{r_e})|^2}{\frac{1}{3}|\mathbf{d}|^2} \quad \text{(C.1)}$$

where bulk n is the refractive index of the bulk material used as reference (in this case InGaAsP, $n_{bulk} = 3.53$), Q is the (unpumped) quality factor, λ_{cav} is the free-space wavelength of the resonance, and V_{eff} and ζ account respectively for the electric field concentration and the location of emitters with respect to the field; $\mathbf{f}(\mathbf{r})$ is the mode field profile, $\mathbf{r_e}$ is the location of the emitter, and $\mathbf{d}$ is its dipole moment. Assuming, as in Hill et al. [92], random orientation of dipole moments, $\zeta = |\mathbf{f}(\mathbf{r_e})|^2$. The scaling of $\mathbf{f}(\mathbf{r_e})$ is arbitrary and has no effect on F_{cav}; it is usually chosen so that $\mathbf{f}(\mathbf{r_e}) = 1$ at the field antinode [95, 144]. With this convention, V_{eff} for the mode shown in 3.2d evaluates to 0.05 µm^3 (Q=1,004, $\lambda_{cav} = 1.538$ µm, cavity dimensions $r_c = 260$ nm, $\Delta = 200$ nm, gain block height $h_c = 480$ nm). The carriers are not all located at field antinodes (which would have produced $\zeta = 1$), but neither are they uniformly distributed over the gain volume, because intensive recombination at the antinodes draws carrier diffusion toward that region [92]. We thus expect ζ to take an intermediate value between unity and the volume average $\frac{1}{V_{gain}} \iiint_{V_{gain}} |\mathbf{f}(\mathbf{r})|^2 d^3\mathbf{r} = 0.456$ (where V_{gain} is the gain volume), yielding the Purcell factor F_{cav} between 19 and 41.

Appendix C, in part, or in full, is a reprint of the material as it appears in "Room-temperature subwavelength metallo-dielectric lasers," M. Nezhad, A. Simic, O. Bondarenko, B. Slutsky, A. Mizrahi, L. Feng, V. Lomakin, and Y. Fainman, *Nature Photonics*, vol. 4, no. 6, pp. 395–399, 2010. The dissertation author was the primary co-investigator and coauthor of this paper.

Appendix D

Fabrication

The (undoped) gain layer was grown on an InP wafer in the InGaAsP quaternary system using MOCVD (fabricated at OEpic Inc.). Both bulk gain and MQWs were used and both exhibited lasing, but the measured results presented are all from the MQW samples. The MQW was comprised of 16 10nm thick wells ($In_{x=0.560}Ga_{1-x}As_{y=0.938}P_{1-y}$) embedded in 17 20 nm thick barriers ($In_{x=0.734}Ga_{1-x}As_{y=0.571}P_{1-y}$), with a PL emission peak at 1,546 nm. The nanolaser fabrication process consisted of the following steps: 1) HSQ resist was spun onto the InGaAsP/InP wafer and patterned into dots via e-beam lithography in a Raith 50 e-beam writer; 2) The dots were etched into pillars using a $CH_4/H_2/Ar$(4:20:20 sccm) RIE process in a Trion etcher at 150 W and 30 mT; 3) Subsequently, the samples were cleaned with O_2 plasma and a buffered oxide etch; 4) silica was deposited on the pillars via SiH_4/N_2O PECVD; 5) The metallization was done using a Denton 18 sputter coater. Initially gold was used for the metal layer but its weak adhesion properties caused the gain disks to fall out of their metal shell in later steps. Simulations showed that the use of an intermediate adhesion layer such as titanium would cause a drastic drop in the cavity Q. Therefore aluminum was used directly, since at 1,550 nm its optical properties are on a par with gold, but it has much better adhesion; 6) After covering the metal coated pillars with SU-8 polymer and bonding to a glass substrate, the InP substrate was removed with a selective HCl etch in the final step of the process.

Appendix D, in part, or in full, is a reprint of the material as it appears in "Room-temperature subwavelength metallo-dielectric lasers," M. Nezhad, A. Simic, O. Bondarenko, B. Slutsky, A. Mizrahi, L. Feng, V. Lomakin, and Y. Fainman, *Nature Photonics*, vol. 4, no. 6, pp. 395–399, 2010. The dissertation author was the primary co-investigator and coauthor of this paper.

Appendix E

Characterization results

Measurement of the light–light curves and the spectral evolution of the laser emission was performed on a sample with major and minor diameters of 490 nm and 420 nm, respectively. The pump was focused to a spot size of approximately 8µm×8µm in diameter (FWHM) with a ×20 long working-distance objective. The pump laser was a 1,064 nm fiber laser operating in either CW mode or pulsed mode (300 kHz and pulse width of 12 ns). During the measurement, the stability of the measurement system was found to be better than 0.25% per hour. The data points were obtained by integrating the emission spectrum over a 20 nm window centered around the lasing peak (from 1,420 nm to 1,440 nm). To observe the spatial coherence of the beam after the onset of lasing, ×50 long working-distance objective was used. The sample was defocused from the object plane of the imaging system by approximately 10 µm (away from the objective) and the resulting diffracted mode pattern was imaged onto the camera. The transition from PL (using a CW pump) to lasing (using a pulsed pump) is dramatically shown by the appearance of Airy-like patterns which indicate the increase of emission coherence. The null feature at the center of the defocused pattern may be a result of a TE_{01} lasing mode (which also has a null in the center), but other effects (such as imaging aberrations) may also be the source of this feature.

The polarization of the emitted beam is elliptical, with a large portion of the lasing power residing in one polarization. This does not agree with the expected azimuthal polarization of a TE_{01} lasing mode. The reason for this discrepancy is

due to the slight ellipticity of the structures which affects the emitted beam in two ways. First, the ellipticity splits the degenerate TE_{01} mode and results in a slightly elliptical lasing mode in the gain core section. Secondly, the elliptic metal coated dielectric section that connects the gain core to free space acts as a weak polarizer and preferentially transmits one polarization, resulting in a rather strong linearly polarized component at the exit aperture of the laser.

For the index of refraction estimation, nine different lasers were selected and pumped with a large area beam (approximately $30\,\mu m \times 30\,\mu m$ in diameter). The major and minor diameters of the nine lasing samples were individually measured using SEM measurements of their base apertures. The gain core was modeled as a three layer stack of elliptical truncated cones to account for the etch profile and slight RIE induced erosion of the core. Then the resonant eigenmodes for each sample were found using a nominal refractive index derived from the unpumped dispersion curve (Figure 3.6, red dashed curve). Based on the estimated gain spectrum of the material, the location of the modes and their lasing threshold, the most likely eigenmode for lasing was found for each cavity and the refractive index was perturbed so that the eigenmode coincided with its corresponding experimental lasing line, resulting in the green data points in Figure 3.6. It is interesting to note that even though for each sample several different eigenmodes were possible lasing candidates, in every case the process of finding the best eigenmode resulted in one of the non-degenerate TE_{012}-like modes being chosen, indicating that the optimized cavity shield thickness is (to some extent) insensitive to variations of the core size. The error bars were calculated assuming a 5 nm error in measuring the laser diameter. Using a least squares fit over the set of lasing points and assuming a constant refractive index drop across the spectrum of interest, the unpumped dispersion curve was down shifted by 0.102 RIU, resulting in the pumped dispersion curve (solid blue line in Figure 3.6).

Appendix E, in part, or in full, is a reprint of the material as it appears in "Room-temperature subwavelength metallo-dielectric lasers," M. Nezhad, A. Simic, O. Bondarenko, B. Slutsky, A. Mizrahi, L. Feng, V. Lomakin, and Y. Fainman,

Nature Photonics, vol. 4, no. 6, pp. 395–399, 2010. The dissertation author was the primary co-investigator and coauthor of this paper.

Appendix F

Linewidth Measurements of IIIV/Si DFB Laser

We examined lasing spectra above the threshold at different pump powers (Figure F.1(a))to study the behavior of the laser linewidth. At the pump powers below 2,000W/mm^2, measured linewidth values are close or below the monochromator resolution limit of 0.35 nm,hence no conclusion about the linewidth dynamics can be drawn. At higher powers, the linewidth steadily broadens as the pump increases. This contradicts the classic Schawlow-Townes and Henry formulae [145, 146] and suggests that the linewidth broadening mechanisms other then spontaneous emission noise may be at work. Several detailed studies of line broadening in fiber lasers [147] and semiconductor lasers [148, 149] describe the spectrum as a Voigt function, which is a convolution of Lorentzian and Gaussian. While the Lorentzian contribution to the linewidth is linked to spontaneous emission noise and narrows with pump, as predicted by Schawlow-Townes and Henry, the Gaussian contribution is attributed to the 1/f population noise [148] and does not necessarily narrow.

Another possible reason for seeming increasing linewidth is the instrumental response. It can be particularly prominent around the instrument resolution limit. To investigate this possibility we measured linewidth using optical spectrum analyzer ANDO 6317B with resolution limit of 0.01 nm (Fig. F.2). Once again, we observed linewidth widening from 0.25 nm at 13 mW input power to 2 nm at

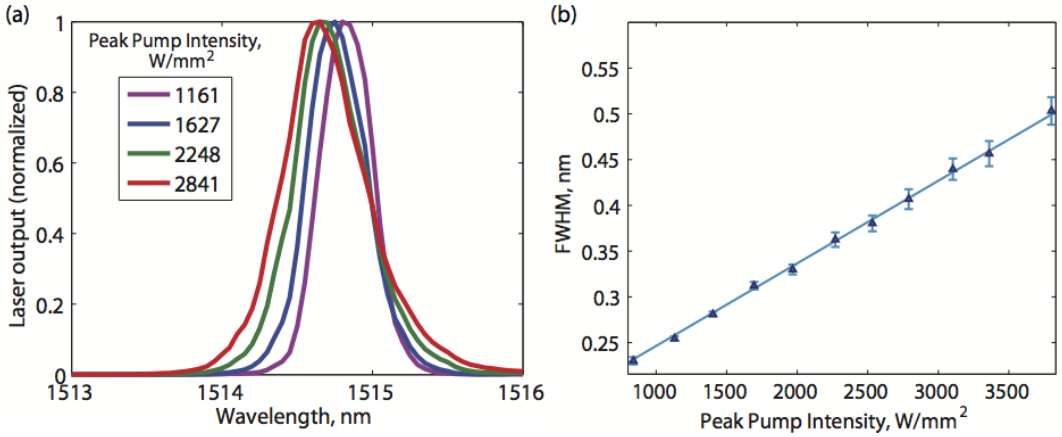

Figure F.1: Linewidth measurements for a 100 µm long laser structure and 545/455 nm grating in spontaneous emission regime: (a) monochromator spectra for different input powers; (b) above threshold linewidth dependence on pump powers.

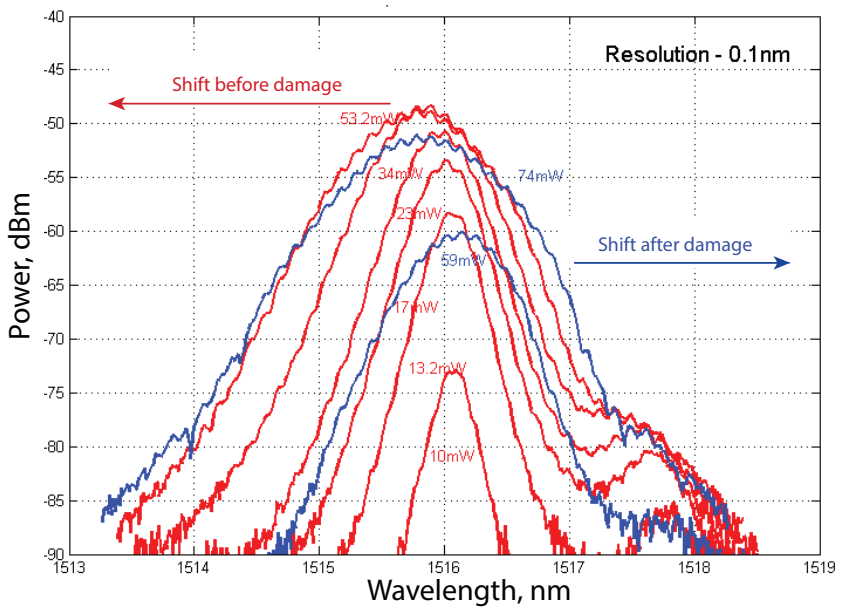

Figure F.2: Linewidth measurements with optical spectrum analyzer ANDO 6317B (resolution limit of 0.01 nm) of a 100 µm long laser structure and 545/455 nm grating in spontaneous emission regime.

53 mW input power. We also observed the peak shifting to the shorter wavelengths. This can be explained by the refractive index increase due to growing carrier concentration. At some point the sample reaches damage threshold and

sustains permanent damage. After that threshold the peak starts shifting to the larger wavelength. The linewidth widening and peak shifting phenomena need to be further investigated.

Appendix G

Mode orthogonality in waveguides

All guided and radiation waveguide modes in a waveguide are mutually orthogonal. This property is related to power conservation law and reciprocity.

Let us consider two different solutions to Maxwell's equations in a lossless scalar medium:

$$\begin{aligned} \mathbf{E}_1(x,y,z) &= \mathbf{E}_{\nu,1}(x,y)e^{(-i\beta_\nu z)},\ \mathbf{H}_1(x,y,z) = \mathbf{H}_{\nu,1}(x,y)e^{(-i\beta_\nu z)} \\ \mathbf{E}_2(x,y,z) &= \mathbf{E}_{\nu,2}(x,y)e^{(-i\beta_\nu z)},\ \mathbf{H}_2(x,y,z) = \mathbf{H}_{\nu,2}(x,y)e^{(-i\beta_\nu z)} \end{aligned} \tag{G.1}$$

where ν is a mode number and β_ν is a propagation constant of the mode. We will next apply the vector identity to the vectr product of $\mathbf{E_1}$ and $\mathbf{E_2}$ fields,

$$\nabla \cdot (a \times \underline{\ }) = b \cdot (\nabla \times a) - a \cdot (\nabla \times b), \tag{G.2}$$

and obtain

$$\nabla \cdot (\mathbf{E_1} \times \mathbf{H^*_2}) = i\omega(\epsilon \mathbf{E_1} \cdot \mathbf{E^*_2} - \mu \mathbf{H_1} \cdot \mathbf{H^*_2}) \tag{G.3}$$

Further manipulations with complex conjugates of the fields [116] render:

$$\nabla \cdot (\mathbf{E_1} \times \mathbf{H^*_2} + \mathbf{E^*_2} \times \mathbf{H_1}) = 0 \tag{G.4}$$

Separation of transverse and longitudinal components, applying of divergence theorem and z-reversal symmetry [116] yields the orthogonality relation:

$$\iint_{-\infty}^{\infty} \mathbf{E_{t\nu}} \times \mathbf{H^*_{t\nu}} \mathrm{d}x\, \mathrm{d}y,\ \beta_\mu \neq \beta_\nu \tag{G.5}$$

Appendix H

Mode expansion and normalization

An electromagnetic field in a waveguide can be represented as a superposition of the continuum of the waveguide modes. It is justified by the mode orthogonality condition [116]. We will only consider exclusively transverse field components, because the longitudinal components can be readily derived from Maxwell's equations and known transverse component. The notations for the transverse electric and magnetic field are $\mathbf{E}_{\nu\mu}(x,y)$ and $\mathbf{H}_{\nu\mu}(x,y)$, respectively.

The total forward propagating field in a waveguide can be expressed as a sum over all the guided and radiation modes in the waveguide:

$$\begin{aligned}\mathbf{E}_t &= \sum_{\nu}\sum_{\mu} a_{\nu\mu}\mathbf{E}_{\nu\mu}(x,y) + \iint_0^\infty d\nu\, d\mu\, a(\nu,\mu)\mathbf{E}(\nu,\mu;x,y) \\ \mathbf{H}_t &= \sum_{\nu}\sum_{\mu} a_{\nu\mu}\mathbf{H}_{\nu\mu}(x,y) + \iint_0^\infty d\nu\, d\mu\, a(\nu,\mu)\mathbf{H}(\nu,\mu;x,y)\end{aligned} \tag{H.1}$$

where the labels ν and μ are called "spatial frequencies" and assigned the units of cm^{-1}. With the purpose of keeping consistent dimensionality across both guided and radiation modes, we have to keep the discrete coefficients $a_{\nu\mu}$ dimensionless and assign the dimension of cm^2 to the continuum coefficients $a(\nu,\mu)$.
Electromagnetic fields in the modes are usually normalized to a power flow of 1W in the z direction. For discrete modes, the normalization factor is

$$\bar{P} = 2\iint_{-\infty}^{\infty} \mathbf{E}_{\nu\mu} \times \mathbf{H^*}_{\nu\mu}\mathrm{d}x\,\mathrm{d}y = \delta_{\nu\bar{\nu}}\delta_{\mu\bar{\mu}} \tag{H.2}$$

where $\delta_{\nu\bar{\nu}}$ is the Kroniker delta.

For continuum of radiation modes, the power normalization factor is

$$\bar{P} = 2\iint_{-\infty}^{\infty} \mathbf{E}_{\nu\mu} \times \mathbf{H}^*{}_{\bar{\nu}\bar{\mu}} \mathrm{d}x\,\mathrm{d}y = \delta(\nu - \bar{\nu})\delta(\mu - \bar{\mu}) \tag{H.3}$$

where $\delta_{\nu-\bar{\nu}}$ is a delta function. Orthonormality relations H.2 in conjunction with Eq. H.3 allow to define mode expansion coefficients $a_{\nu\mu}$ and $a(\nu, \mu)$ in a simple way. For the discrete coefficients, we arrive to:

$$a_{\nu\mu} = 2\iint_{-\infty}^{\infty} \mathbf{E}_t \times \mathbf{H}^*{}_{\nu\mu} \mathrm{d}x\,\mathrm{d}y = 2\iint_{-\infty}^{\infty} \mathbf{E}^*{}_{\nu\mu} \times \mathbf{H}_t \mathrm{d}x\,\mathrm{d}y, \tag{H.4}$$

and for continuum coefficients, we obtain:

$$a(\nu, \mu) = 2\iint_{-\infty}^{\infty} \mathbf{E}_t \times \mathbf{H}^*(\nu, \mu) \mathrm{d}x\,\mathrm{d}y = 2\iint_{-\infty}^{\infty} \mathbf{E}^*{}_(\nu, \mu) \times \mathbf{H}_t \mathrm{d}x\,\mathrm{d}y. \tag{H.5}$$

We can also express the power carried by the total field in terms of the expansion coefficients through the orthogonality relations:

$$P = \iint_{-\infty}^{\infty} (\mathbf{E}_t \times \mathbf{H}^*{}_t + \mathbf{E}^*{}_t \times \mathbf{H}_t)_z \tag{H.6}$$

where P is measured in Watts. A backward propagating waveguide mode has an identical transverse field distribution to the forward propagating mode:

$$\mathbf{E}_{-\nu}(x, y) = \mathbf{E}_\nu(x, y)\mathbf{H}_{-\nu}(x, y) = -\mathbf{H}_\nu(x, y) \tag{H.7}$$

Thus, we can present a waveguide field in the following form:

$$\mathbf{E}_t = \sum (a_\nu + b_\nu)\mathbf{E}_\nu \mathbf{H}_t = \sum (a_\nu - b_\nu)\mathbf{H}_\nu \tag{H.8}$$

where a_ν are the coefficients of forward propagating modes and b_ν are the coefficients for the backward propagating modes. Using the orthogonality relation

$$\iint_{-\infty}^{\infty} \mathbf{E}_\nu \times \mathbf{H}^*{}_\mu \mathrm{d}x\,\mathrm{d}y \tag{H.9}$$

where $\beta_\mu \neq \beta_\nu$ we can find a_ν and b_ν:

$$\begin{aligned} a_\nu &= \iint_{-\infty}^{\infty} (\mathbf{E}_t \times \mathbf{H}^*{}_\nu + \mathbf{E}^*{}_\nu \times \mathbf{H}_t) \mathrm{d}x\,\mathrm{d}y \\ b_\nu &= \iint_{-\infty}^{\infty} (\mathbf{E}_t \times \mathbf{H}^*{}_\nu - \mathbf{E}^*{}_\nu \times \mathbf{H}_t) \mathrm{d}x\,\mathrm{d}y \end{aligned} \tag{H.10}$$

For a rigorous information about mode orthogonality, expansion and field normalization, refer to [116].

Bibliography

[1] Cisco, *The Zettabyte Era – Trends and Analysis (white paper)*. 2014.

[2] M. M. Center, *Scaling Limits for Copper Interconnects (white paper)*. 2011.

[3] D. A. B. Miller, "Optical interconnects to electronic chips," *Applied optics*, vol. 49, no. 25, pp. F59–70, 2010.

[4] K. Igarashi, K. Takeshima, T. Tsuritani, H. Takahashi, S. Sumita, I. Morita, Y. Tsuchida, M. Tadakuma, K. Maeda, T. Saito, K. Watanabe, K. Imamura, R. Sugizaki, and M. Suzuki, "110.9-Tbit/s SDM transmission over 6,370 km using a full C-band seven-core EDFA," *Optics Express*, vol. 21, no. 15, pp. 18053–60, 2013.

[5] T. Morioka, Y. Awaji, R. Ryf, P. Winzer, D. Richardson, and F. Poletti, "Enhancing optical communications with brand new fibers," *IEEE Communications Magazine*, vol. 50, no. 2, pp. s31–s42, 2012.

[6] V. A. Sleiffer, P. Leoni, Y. Jung, H. Chen, M. Kuschnerov, S. Alam, M. Petrovich, F. Poletti, N. V. Wheeler, N. Baddela, J. Hayes, E. Numkam Fokoua, D. J. Richardson, L. E. Gruner-Nielsen, Y. Sun, and H. de Waardt, "Ultra-high Capacity Transmission with Few-mode Silica and Hollow-core Photonic Bandgap Fibers," in *Optical Fiber Communication Conference*, (Washington, D.C.), p. Tu2J.3, OSA, 2014.

[7] F. Poletti, N. V. Wheeler, M. N. Petrovich, N. Baddela, E. Numkam Fokoua, J. R. Hayes, D. R. Gray, Z. Li, R. Slavík, and D. J. Richardson, "Towards high-capacity fibre-optic communications at the speed of light in vacuum," *Nature Photonics*, vol. 7, no. 4, pp. 279–284, 2013.

[8] D. Dai, J. Wang, and Y. Shi, "Silicon mode (de)multiplexer enabling high capacity photonic networks-on-chip with a single-wavelength-carrier light," *Optics Letters*, vol. 38, no. 9, pp. 1422–4, 2013.

[9] L. Chen, C. R. Doerr, L. Buhl, Y. Baeyens, and R. A. Aroca, "Monolithically Integrated 40-Wavelength Demultiplexer and Photodetector Array on

Silicon," *IEEE Photonics Technology Letters*, vol. 23, no. 13, pp. 869–871, 2011.

[10] L.-W. Luo, N. Ophir, C. P. Chen, L. H. Gabrielli, C. B. Poitras, K. Bergmen, and M. Lipson, "WDM-compatible mode-division multiplexing on a silicon chip," *Nature Communications*, vol. 5, p. 3069, 2014.

[11] F. Horst, W. M. J. Green, S. Assefa, S. M. Shank, Y. A. Vlasov, and B. J. Offrein, "Cascaded Mach-Zehnder wavelength filters in silicon photonics for low loss and flat pass-band WDM (de-)multiplexing," *Optics Express*, vol. 21, no. 10, pp. 11652–8, 2013.

[12] Infinera, *Photonic Integration (white paper)*. 2005.

[13] F. E. M. P. (FEMP), "Best Practices Guide for Energy-Efficient Data Center Design," 2011.

[14] Q. Gu, J. S. T. Smalley, M. P. Nezhad, A. Simic, J. H. Lee, M. Katz, O. Bondarenko, B. Slutsky, A. Mizrahi, V. Lomakin, and Y. Fainman, "Subwavelength semiconductor lasers for dense chip-scale integration," *Advances in Optics and Photonics*, vol. 6, no. 1, p. 1, 2014.

[15] R. F. Oulton, V. J. Sorger, T. Zentgraf, R.-M. Ma, C. Gladden, L. Dai, G. Bartal, and X. Zhang, "Plasmon lasers at deep subwavelength scale," *Nature*, vol. 461, no. 7264, pp. 629–632, 2009.

[16] K. Yu, A. Lakhani, and M. Wu, "Subwavelength metal-optic semiconductor nanopatch lasers," *Optics Express*, vol. 18, no. 9, pp. 8790–8799, 2010.

[17] J. H. Lee, M. Khajavikhan, A. Simic, Q. Gu, O. Bondarenko, B. Slutsky, M. P. Nezhad, and Y. Fainman, "Electrically pumped sub-wavelength metallo-dielectric pedestal pillar lasers.," *Optics Express*, vol. 19, no. 22, pp. 21524–31, 2011.

[18] Y. Halioua, A. Bazin, P. Monnier, T. J. Karle, G. Roelkens, I. Sagnes, R. Raj, and F. Raineri, "Hybrid III-V semiconductor/silicon nanolaser," *Optics Express*, vol. 19, no. 10, pp. 9221–31, 2011.

[19] O. Bondarenko, A. Simic, Q. Gu, J. H. Lee, B. Slutsky, M. P. Nezhad, and Y. Fainman, "Wafer Bonded Subwavelength Metallo-Dielectric Laser," *IEEE Photonics Journal*, vol. 3, no. 3, pp. 608–616, 2011.

[20] A. Mizrahi, V. Lomakin, B. Slutsky, M. Nezhad, L. Feng, and Y. Fainman, "Low threshold gain metal coated laser nanoresonators," *Optics Letters*, vol. 33, no. 11, pp. 1261–1263, 2008.

[21] M. P. Nezhad, A. Simic, O. Bondarenko, B. Slutsky, A. Mizrahi, L. Feng, V. Lomakin, and Y. Fainman, "Room-temperature subwavelength metallodielectric lasers," *Nature Photonics*, vol. 4, no. 6, pp. 395–399, 2010.

[22] M. Khajavikhan, A. Simic, M. Katz, J. H. Lee, B. Slutsky, A. Mizrahi, V. Lomakin, and Y. Fainman, "Thresholdless nanoscale coaxial lasers," *Nature*, vol. 482, no. 7384, pp. 204–7, 2012.

[23] S. Assefa, S. Shank, W. Green, M. Khater, E. Kiewra, C. Reinholm, S. Kamlapurkar, A. Rylyakov, C. Schow, F. Horst, H. Pan, T. Topuria, P. Rice, D. M. Gill, J. Rosenberg, T. Barwicz, M. Yang, J. Proesel, J. Hofrichter, B. Offrein, X. Gu, W. Haensch, J. Ellis-Monaghan, and Y. Vlasov, "A 90nm CMOS Intergated Nanophotonics Technology for 25Gbps WDM Optical Communications Applications," in *2012 International Electron Devices Meeting*, pp. 33.8.1–33.8.3, IEEE, 2012.

[24] Intel, "Intel Unveils New Technologies for Efficient Cloud Datacenters," 2013.

[25] E. Marchena, T. Creazzo, S. B. Krasulick, P. Yu, D. Van Orden, J. Y. Spann, C. C. Blivin, J. M. Dallesasse, P. Varangis, R. J. Stone, and A. Mizrahi, "Integrated Tunable CMOS Laser for Si Photonics," in *Optical Fiber Communication Conference/National Fiber Optic Engineers Conference 2013*, (Washington, D.C.), p. PDP5C.7, OSA, 2013.

[26] B. R. Koch, E. J. Norberg, B. Kim, J. Hutchinson, J.-H. Shin, G. Fish, and A. Fang, "Integrated Silicon Photonic Laser Sources for Telecom and Datacom," in *Optical Fiber Communication Conference/National Fiber Optic Engineers Conference 2013*, (Washington, D.C.), p. PDP5C.8, OSA, 2013.

[27] G. Roelkens, U. Dave, A. Gassenq, N. Hattasan, B. Kuyken, F. Leo, A. Malik, M. Muneeb, E. Ryckeboer, D. Sanchez, S. Uvin, R. Wang, Z. Hens, R. Baets, Y. Shimura, F. Gencarelli, B. Vincent, R. Loo, J. Van Campenhout, L. Cerutti, J.-B. Rodriguez, E. Tournie, M. Nedeljkovic, G. Mashanovich, N. Healy, A. C. Peacock, R. Osgood, and W. M. J. Green, "Silicon-Based Photonic Integration Beyond the Telecommunication Wavelength Range," *IEEE Journal of Selected Topics in Quantum Electronics*, vol. 20, no. 4, pp. 394–404, 2014.

[28] G. T. Reed, G. Mashanovich, F. Y. Gardes, and D. J. Thomson, "Silicon optical modulators," *Nature Photonics*, vol. 4, no. 8, pp. 518–526, 2010.

[29] S. S. Djordjevic, K. Shang, B. Guan, S. T. S. Cheung, L. Liao, J. Basak, H.-F. Liu, and S. J. B. Yoo, "CMOS-compatible, athermal silicon ring modulators clad with titanium dioxide," *Optics Express*, vol. 21, no. 12, pp. 13958–68, 2013.

[30] M. Casalino, M. Iodice, L. Sirleto, I. Rendina, and G. Coppola, "Asymmetric MSM sub-bandgap all-silicon photodetector with low dark current," *Optics Express*, vol. 21, no. 23, pp. 28072–82, 2013.

[31] M.-J. Lee and W.-Y. Choi, "A silicon avalanche photodetector fabricated with standard CMOS technology with over 1 THz gain-bandwidth product," *Optics Express*, vol. 18, no. 23, pp. 24189–94, 2010.

[32] S. Huang, W. Lu, C. Li, W. Huang, H. Lai, and S. Chen, "A CMOS-compatible approach to fabricate an ultra-thin germanium-on-insulator with large tensile strain for Si-based light emission," *Optics Express*, vol. 21, no. 1, pp. 640–6, 2013.

[33] C. T. DeRose, D. C. Trotter, W. A. Zortman, A. L. Starbuck, M. Fisher, M. R. Watts, and P. S. Davids, "Ultra compact 45 GHz CMOS compatible Germanium waveguide photodiode with low dark current," *Optics Express*, vol. 19, no. 25, pp. 24897–904, 2011.

[34] A. Pospischil, M. Humer, M. M. Furchi, D. Bachmann, R. Guider, T. Fromherz, and T. Mueller, "CMOS-compatible graphene photodetector covering all optical communication bands," *Nature Photonics*, vol. 7, no. 11, pp. 892–896, 2013.

[35] H. Rong, R. Jones, A. Liu, O. Cohen, D. Hak, A. Fang, and M. Paniccia, "A continuous-wave Raman silicon laser," *Nature*, vol. 433, no. 7027, pp. 725–8, 2005.

[36] O. Boyraz and B. Jalali, "Demonstration of directly modulated silicon Raman laser," *Optics Express*, vol. 13, no. 3, p. 796, 2005.

[37] R. E. Camacho-Aguilera, Y. Cai, N. Patel, J. T. Bessette, M. Romagnoli, L. C. Kimerling, and J. Michel, "An electrically pumped germanium laser," *Optics Express*, vol. 20, no. 10, pp. 11316–11320, 2012.

[38] J. Liu, X. Sun, R. Camacho-Aguilera, L. C. Kimerling, and J. Michel, "Ge-on-Si laser operating at room temperature," *Optics Letters*, vol. 35, no. 5, pp. 679–81, 2010.

[39] L. Coldren and S. Corzine, *Diode Lasers and Photonic Integrated Circuits*. ohn Wiley and Sons, New York N. Y., 1995.

[40] P. Abraham, J. Piprek, S. P. DenBaars, and J. E. Bowers, "Improvement of Internal Quantum Efficiency in 1.55 mum Laser Diodes with InGaP Electron Stopper Layer," *Japanese Journal of Applied Physics*, vol. 38, no. Part 1, No. 2B, pp. 1239–1242, 1999.

[41] C. Kittel, *Introduction to Solid State Physics*, vol. 11. Wiley, 2004.

[42] S. Tanaka, S.-H. Jeong, S. Sekiguchi, T. Kurahashi, Y. Tanaka, and K. Morito, "High-output-power, single-wavelength silicon hybrid laser using precise flip-chip bonding technology.," *Optics Express*, vol. 20, no. 27, pp. 28057–69, 2012.

[43] A. J. Zilkie, P. Seddighian, B. J. Bijlani, W. Qian, D. C. Lee, S. Fathololoumi, J. Fong, R. Shafiiha, D. Feng, B. J. Luff, X. Zheng, J. E. Cunningham, A. V. Krishnamoorthy, and M. Asghari, "Power-efficient III-V/silicon external cavity DBR lasers.," *Optics Express*, vol. 20, no. 21, pp. 23456–62, 2012.

[44] J. H. Lee, I. Shubin, J. Yao, J. Bickford, Y. Luo, S. Lin, S. S. Djordjevic, H. D. Thacker, J. E. Cunningham, K. Raj, X. Zheng, and A. V. Krishnamoorthy, "High power and widely tunable Si hybrid external-cavity laser for power efficient Si photonics WDM links.," *Optics Express*, vol. 22, no. 7, pp. 7678–85, 2014.

[45] S. Lourdudoss, "Heteroepitaxy and selective area heteroepitaxy for silicon photonics," *Current Opinion in Solid State and Materials Science*, vol. 16, no. 2, pp. 91–99, 2012.

[46] C.-W. Hsu, Y.-F. Chen, and Y.-K. Su, "Heteroepitaxy for GaAs on Nanopatterned Si (001)," *IEEE Photonics Technology Letters*, vol. 24, no. 12, pp. 1009–1011, 2012.

[47] M. Cantoro, C. Merckling, S. Jiang, W. Guo, N. Waldron, H. Bender, A. Moussa, B. Douhard, W. Vandervorst, M. M. Heyns, *et al.*, "Heteroepitaxy of iii-v compound semiconductors on silicon for logic applications: Selective area epitaxy in shallow trench isolation structures vs. direct epitaxy mediated by strain relaxed buffers," *ECS Transactions*, vol. 50, no. 9, pp. 349–355, 2013.

[48] A. Lee, Q. Jiang, M. Tang, A. Seeds, and H. Liu, "Continuous-wave InAs/GaAs quantum-dot laser diodes monolithically grown on Si substrate with low threshold current densities," *Optics Express*, vol. 20, no. 20, pp. 22181–7, 2012.

[49] T. Frost, S. Jahangir, E. Stark, S. Deshpande, A. Hazari, C. Zhao, B. S. Ooi, and P. Bhattacharya, "Monolithic electrically injected nanowire array edge-emitting laser on (001) silicon," *Nano letters*, vol. 14, no. 8, pp. 4535–41, 2014.

[50] H. Ghafouri-Shiraz, *Distributed feedback laser diodes and optical tunable filters*. John Wiley & Sons, 2004.

[51] P. Rojo Romeo, J. Van Campenhout, P. Regreny, A. Kazmierczak, C. Seassal, X. Letartre, G. Hollinger, D. Van Thourhout, R. Baets, J. M. Fedeli, and

L. Di Cioccio, "Heterogeneous integration of electrically driven microdisk based laser sources for optical interconnects and photonic ICs," *Optics Express*, vol. 14, no. 9, p. 3864, 2006.

[52] A. W. Fang, H. Park, O. Cohen, R. Jones, M. J. Paniccia, and J. E. Bowers, "Electrically pumped hybrid AlGaInAs-silicon evanescent laser," *Optics Express*, vol. 14, no. 20, p. 9203, 2006.

[53] A. W. Fang, R. Jones, H. Park, O. Cohen, O. Raday, M. J. Paniccia, and J. E. Bowers, "Integrated AlGaInAs-silicon evanescent race track laser and photodetector," *Optics Express*, vol. 15, no. 5, p. 2315, 2007.

[54] A. W. Fang, E. Lively, Y.-H. Kuo, D. Liang, and J. E. Bowers, "A distributed feedback silicon evanescent laser," *Optics Express*, vol. 16, no. 7, p. 4413, 2008.

[55] B. R. Koch, A. Alduino, L. Liao, R. Jones, M. Morse, B. Kim, W.-Z. Lo, J. Basak, H.-F. Liu, H. Rong, M. Sysak, C. Krause, R. Saba, D. Lazar, L. Horwitz, R. Bar, S. Litski, A. Liu, K. Sullivan, O. Dosunmu, N. Na, T. Yin, F. Haubensack, I.-w. Hsieh, J. Heck, R. Beatty, J. Bovington, and M. J. Paniccia, "A 4x12.5 Gbps CWDM Si Photonics Link using Integrated Hybrid Silicon Lasers," in *CLEO:2011 - Laser Applications to Photonic Applications*, (Washington, D.C.), p. CThP5, OSA, 2011.

[56] S. Stankovic, R. Jones, M. Sysak, J. Heck, G. Roelkens, and D. Van Thourhout, "Hybrid iii-v/si distributed-feedback laser based on adhesive bonding," *Photonics Technology Letters, IEEE*, vol. 24, no. 23, pp. 2155–2158, 2012.

[57] S. Keyvaninia, G. Roelkens, D. Van Thourhout, C. Jany, M. Lamponi, A. Le Liepvre, F. Lelarge, D. Make, G.-H. Duan, D. Bordel, and J.-M. Fedeli, "Demonstration of a heterogeneously integrated III-V/SOI single wavelength tunable laser," *Optics Express*, vol. 21, no. 3, pp. 3784–92, 2013.

[58] L. Tao, L. Yuan, Y. Li, H. Yu, B. Wang, Q. Kan, W. Chen, J. Pan, G. Ran, and W. Wang, "4-λ InGaAsP-Si distributed feedback evanescent lasers with varying silicon waveguide width," *Optics Express*, vol. 22, no. 5, pp. 5448–54, 2014.

[59] O. Bondarenko, Q. Gu, J. Shane, A. Simic, B. Slutsky, and Y. Fainman, "Wafer bonded distributed feedback laser with sidewall modulated Bragg gratings," *Applied Physics Letters*, vol. 103, no. 4, p. 043105, 2013.

[60] Y. de Koninck, F. Raineri, A. Bazin, R. Raj, G. Roelkens, and R. Baets, "Experimental demonstration of a hybrid III-V-on-silicon microlaser based on resonant grating cavity mirrors," *Optics Letters*, vol. 38, no. 14, pp. 2496–8, 2013.

[61] Y. Zhang, H. Qu, H. Wang, S. Zhang, L. Liu, S. Ma, and W. Zheng, "A hybrid silicon single mode laser with a slotted feedback structure," *Optics Express*, vol. 21, no. 1, pp. 877–83, 2013.

[62] C. T. Santis, S. T. Steger, Y. Vilenchik, A. Vasilyev, and A. Yariv, "High-coherence semiconductor lasers based on integral high-Q resonators in hybrid Si/III-V platforms," *Proceedings of the National Academy of Sciences of the United States of America*, vol. 111, no. 8, pp. 2879–84, 2014.

[63] D. Pasquariello and K. Hjort, "Plasma-assisted InP-to-Si low temperature wafer bonding," *IEEE Journal of Selected Topics in Quantum Electronics*, vol. 8, no. 1, pp. 118–131, 2002.

[64] T. R. Chung, L. Yang, N. Hosoda, and T. Suga, "Room temperature GaAs-Si and InP-Si wafer direct bonding by the surface activated bonding method," *Nuclear Instruments and Methods in Physics Research Section B*, vol. 121, no. 1-4, pp. 203–206, 1997.

[65] D. Liang, J. E. Bowers, D. C. Oakley, A. Napoleone, D. C. Chapman, C.-L. Chen, P. W. Juodawlkis, and O. Raday, "High-Quality 150âĂŽÃĎÃĞmm InP-to-Silicon Epitaxial Transfer for Silicon Photonic Integrated Circuits," *Electrochemical and Solid-State Letters*, vol. 12, no. 4, p. H101, 2009.

[66] M. Schmidt, "Wafer-to-wafer bonding for microstructure formation," *Proceedings of the IEEE*, vol. 86, no. 8, pp. 1575–1585, 1998.

[67] D. Liang, A. W. Fang, H. Park, T. E. Reynolds, K. Warner, D. C. Oakley, and J. E. Bowers, "Low-Temperature, Strong SiO2-SiO2 Covalent Wafer Bonding for IIIâĂŽÃĎÃňV Compound Semiconductors-to-Silicon Photonic Integrated Circuits," *Journal of Electronic Materials*, vol. 37, no. 10, pp. 1552–1559, 2008.

[68] M. Howlader, T. Watanabe, and T. Suga, "Bonding of p-Si/n-InP wafers through surface activated bonding method at room temperature," in *Conference Proceedings. 2001 International Conference on Indium Phosphide and Related Materials. 13th IPRM (Cat. No.01CH37198)*, pp. 272–275, IEEE, 2001.

[69] V. Dragoi, G. Mittendorfer, J. Burggraf, and M. Wimplinger, "Metal Thermocompression Wafer Bonding for 3D Integration and MEMS Applications," in *ECS Transactions*, vol. 33, pp. 27–35, The Electrochemical Society, 2010.

[70] M. Koyanagi, T. Nakamura, Y. Yamada, H. Kikuchi, T. Fukushima, T. Tanaka, and H. Kurino, "Three-Dimensional Integration Technology Based on Wafer Bonding With Vertical Buried Interconnections," *IEEE Transactions on Electron Devices*, vol. 53, no. 11, pp. 2799–2808, 2006.

[71] R. Wolffenbuttel and K. Wise, "Low-temperature silicon wafer-to-wafer bonding using gold at eutectic temperature," *Sensors and Actuators A: Physical*, vol. 43, no. 1-3, pp. 223–229, 1994.

[72] K. M. Knowles and A. T. J. van Helvoort, "Anodic bonding," *International Materials Reviews*, vol. 51, no. 5, pp. 273–311, 2006.

[73] F. Niklaus, G. Stemme, J. Lu, and R. Gutmann, "Adhesive wafer bonding," *Journal of Applied Physics*, vol. 99, p. 031101, 2006.

[74] J. W. Chung, E. L. Piner, and T. Palacios, "N-face gan/algan hemts fabricated through layer transfer technology," *Electron Device Letters, IEEE*, vol. 30, no. 2, pp. 113–116, 2009.

[75] R. Wolffenbuttel, "Low-temperature intermediate Au-Si wafer bonding; eutectic or silicide bond," *Sensors and Actuators A: Physical*, vol. 62, no. 1-3, pp. 680–686, 1997.

[76] D. Liang, J. E. Bowers, D. C. Oakley, A. Napoleone, D. C. Chapman, L.-C. Chen, P. W. Juodawlkis, and O. Raday, "High-quality 150 mm inp-to-silicon epitaxial transfer for silicon photonic integrated circuits," vol. 12, no. 4, pp. H101 – H104, 2009.

[77] A. Simic, *Sub-wavelength resonant structures at microwave and optical frequencies*. PhD thesis, University of California San Diego, 2011.

[78] F. Iacopi, M. Baklanov, E. Sleeckx, T. Conard, H. Bender, H. Meynen, and K. Maex, "Properties of porous hsq-based films capped by plasma enhanced chemical vapor deposition dielectric layers," *Journal of Vacuum Science & Technology B: Microelectronics and Nanometer Structures*, vol. 20, no. 1, pp. 109–115, 2002.

[79] M. P. Nezhad, O. Bondarenko, M. Khajavikhan, A. Simic, and Y. Fainman, "Etch-free low loss silicon waveguides using hydrogen silsesquioxane oxidation masks," *Optics Express*, vol. 19, no. 20, pp. 18827–18832, 2011.

[80] G. T. Edwards, P. M. Smowton, and D. I. Westwood, "Dry etching of anisotropic microstructures for distributed bragg reflectors in algainp/gaas laser structures," *IEEE Journal of Selected Topics in Quantum Electronics*, vol. 14, no. 4, pp. 1098–1103, 2008.

[81] T. R. Hayes, M. A. Dreisbach, P. M. Thomas, W. C. DautremontâĂŽÃĎÃł-Smith, and L. A. Heimbrook, "Reactive ion etching of inp using ch4/h2 mixtures: Mechanisms of etching and anisotropy," *Journal of Vacuum Science & Technology B*, vol. 7, no. 5, 1989.

[82] J. Diniz, J. Swart, K. Jung, J. Hong, and S. Pearton, "Inductively coupled plasma etchingof in-based compound semiconductorsin ch 4/h 2/ar," *Solid-State Electronics*, vol. 42, no. 11, pp. 1947–1951, 1998.

[83] D. L. Melville, J. G. Simmons, and D. A. Thompson, "Identification of volatile products in low pressure hydrocarbon electron cyclotron resonance reactive ion etching of inp and gaas," *Journal of Vacuum Science & Technology B*, vol. 11, no. 6, 1993.

[84] S. McCall, A. Levi, R. Slusher, S. Pearton, and R. Logan, "Whispering-gallery mode microdisk lasers," *Applied physics letters*, vol. 60, no. 3, pp. 289–291, 1992.

[85] P. Jin Shan, C. Po Hsiu, L. Tsin Dong, L. Yinchieh, and T. Kuochou, "0.66 µm InGaP/InGaAlP single quantum well microdisk lasers," *Japanese Journal of Applied Physics, Part 2*, vol. 37, pp. L643–L645, 1998.

[86] M. Zain, N. Johnson, M. Sorel, and R. De La Rue, "High quality-factor 1-D-suspended photonic crystal/photonic wire silicon waveguide micro-cavities," *Photonics Technology Letters, IEEE*, vol. 21, no. 24, pp. 1789–1791, 2009.

[87] Y. Akahane, T. Asano, B. Song, and S. Noda, "High-Q photonic nanocavity in a two-dimensional photonic crystal," *Nature*, vol. 425, no. 6961, pp. 944–947, 2003.

[88] Q. Song, H. Cao, S. Ho, and G. Solomon, "Near-IR subwavelength microdisk lasers," *Applied Physics Letters*, vol. 94, p. 061109, 2009.

[89] E. Smotrova, A. Nosich, T. Benson, and P. Sewell, "Optical coupling of whispering-gallery modes of two identical microdisks and its effect on photonic molecule lasing," *IEEE Journal of Selected Topics in Quantum Electronics*, vol. 12, no. 1, pp. 78–85, 2006.

[90] M. Nezhad, K. Tetz, and Y. Fainman, "Gain assisted propagation of surface plasmon polaritons on planar metallic waveguides," *Optics Express*, vol. 12, no. 17, pp. 4072–4079, 2004.

[91] B. Min, E. Ostby, V. Sorger, E. Ulin-Avila, L. Yang, X. Zhang, and K. Vahala, "High-Q surface-plasmon-polariton whispering-gallery microcavity," *Nature*, vol. 457, no. 7228, pp. 455–458, 2009.

[92] M. Hill, Y. Oei, B. Smalbrugge, Y. Zhu, T. De Vries, P. van Veldhoven, F. van Otten, T. Eijkemans, J. Turkiewicz, H. de Waardt, *et al.*, "Lasing in metallic-coated nanocavities," *Nature Photonics*, vol. 1, no. 10, pp. 589–597, 2007.

[93] P. Johnson and R. Christy, "Optical constants of the noble metals," *Physical Review B*, vol. 6, no. 12, pp. 4370–4379, 1972.

[94] E. Goebel, G. Luz, and E. Schlosser, "Optical gain spectra of InGaAsP/InP double heterostructures," *IEEE Journal of Quantum Electronics*, vol. 15, no. 8, pp. 697–700, 1979.

[95] M. Hill, M. Marell, E. Leong, B. Smalbrugge, Y. Zhu, M. Sun, P. van Veldhoven, E. Geluk, F. Karouta, Y. Oei, *et al.*, "Lasing in metal-insulator-metal sub-wavelength plasmonic waveguides," *Optics Express*, vol. 17, no. 13, pp. 11107–11112, 2009.

[96] E. Palik and G. Ghosh, *Handbook of optical constants of solids: five-volume set*. Academic press, 1998.

[97] B. Bennett, R. Soref, and J. Del Alamo, "Carrier-induced change in refractive index of InP, GaAs, and InGaAsP," *IEEE Journal of Quantum Electronics*, vol. 26, no. 1, 1990.

[98] C. Chua, R. Thornton, D. Treat, and R. Donaldson, "Independently addressable VCSEL arrays on 3 µm pitch," *IEEE Photonics Technology Letters*, vol. 10, no. 7, pp. 917–919, 1998.

[99] A. Kroner, F. Rinaldi, R. Rosch, and R. Michalzik, "Optical particle manipulation by application-specific densely packed VCSEL arrays," *Electronics Letters*, vol. 44, no. 5, pp. 353–354, 2008.

[100] D. Hatice Altug *et al.*, "Ultrafast photonic crystal nanocavity laser," *Nature Physics*, vol. 2, no. 7, pp. 484–488, 2006.

[101] Z. Rao, L. Hesselink, and J. Harris, "High-intensity bowtie-shaped nano-aperture vertical-cavity surface-emitting laser for near-field optics," *Optics Letters*, vol. 32, no. 14, pp. 1995–1997, 2007.

[102] H. Rong, R. Jones, A. Liu, O. Cohen, D. Hak, A. Fang, and M. Paniccia, "A continuous-wave Raman silicon laser," *Nature*, vol. 433, no. 7027, pp. 725–728, 2005.

[103] L. Dal Negro, "Light emission from silicon nanostructures: Past, present and future perspectives," in *Conference on Lasers and Electro-Optics and Conference on Quantum electronics and Laser Science (CLEO/QELS) 2009.*, pp. 1–2, IEEE, 2009.

[104] A. Fang, H. Park, O. Cohen, R. Jones, M. Paniccia, and J. Bowers, "Electrically pumped hybrid AlGaInAs-silicon evanescent laser," *Optics Express*, vol. 14, no. 20, pp. 9203–9210, 2006.

[105] H. Park, S. Kim, S. Kwon, Y. Ju, J. Yang, J. Baek, S. Kim, and Y. Lee, "Electrically driven single-cell photonic crystal laser," *Science*, vol. 305, no. 5689, p. 1444, 2004.

[106] M. Nezhad, A. Simic, O. Bondarenko, B. Slutsky, A. Mizrahi, L. Feng, V. Lomakin, and Y. Fainman, "Room-temperature subwavelength metallo-dielectric lasers," *Nature Photonics*, vol. 4, no. 6, pp. 395–399, 2010.

[107] R. Ma, R. Oulton, V. Sorger, G. Bartal, and X. Zhang, "Room-temperature sub-diffraction-limited plasmon laser by total internal reflection," *Nature Materials*, vol. 10, no. 2, pp. 110–113, 2010.

[108] D. Van Thourhout, G. Roelkens, R. Baets, W. Bogaerts, J. Brouckaert, P. Debackere, P. Dumon, S. Scheerlinck, J. Schrauwen, D. Taillaert, *et al.*, "Coupling mechanisms for a heterogeneous silicon nanowire platform," *Semiconductor Science and Technology*, vol. 23, p. 064004, 2008.

[109] D. Liang, J. Bowers, D. Oakley, A. Napoleone, D. Chapman, C. Chen, P. Juodawlkis, and O. Raday, "High-quality 150 mm InP-to-silicon epitaxial transfer for silicon photonic integrated circuits," *Electrochemical and Solid-state Letters*, vol. 12, p. H101, 2009.

[110] D. Liang, A. Fang, H. Park, T. Reynolds, K. Warner, D. Oakley, and J. Bowers, "Low-Temperature, Strong SiO_2-SiO_2 Covalent Wafer Bonding for III–V Compound Semiconductors-to-Silicon Photonic Integrated Circuits," *Journal of Electronic Materials*, vol. 37, no. 10, pp. 1552–1559, 2008.

[111] D. Pasquariello and K. Hjort, "Plasma-assisted InP-to-Si low temperature wafer bonding," *IEEE Journal of Selected Topics in Quantum Electronics*, vol. 8, no. 1, pp. 118–131, 2002.

[112] L. Coldren, S. Corzine, and L. Coldren, *Diode lasers and photonic integrated circuits*. Wiley New York, 1995.

[113] M. Osinski and J. Buus, "Linewidth broadening factor in semiconductor lasers–An overview," *IEEE Journal of Quantum Electronics*, vol. 23, no. 1, pp. 9–29, 1987.

[114] T. Baba and D. Sano, "Low-threshold lasing and Purcell effect in microdisk lasers at room temperature," *IEEE Journal of Selected Topics in Quantum Electronics*, vol. 9, no. 5, pp. 1340–1346, 2003.

[115] K. Srinivasan, M. Borselli, O. Painter, A. Stintz, and S. Krishna, "Cavity Q, mode volume, and lasing threshold in small diameter AlGaAs microdisks with embedded quantum dots," *Optics Express*, vol. 14, no. 3, pp. 1094–1105, 2006.

[116] H. Kogelnik, "2. theory of dielectric waveguides," in *Integrated Optics*, vol. 7 of *Topics in Applied Physics*, pp. 13–81, Springer Berlin Heidelberg, 1975.

[117] H.-C. Kim, K. Ikeda, and Y. Fainman, "Resonant waveguide device with vertical gratings," *Optics Letters*, vol. 32, no. 5, pp. 539–541, 2007.

[118] P. Y. A. Yariv, *Optical waves in crystals: propagation and control of laser radiation*. John Wiley and Sons, Hoboken N. J., 2003.

[119] H. Kogelnik, "Coupled-Wave Theory of Distributed Feedback Lasers," *Journal of Applied Physics*, vol. 43, no. 5, p. 2327, 1972.

[120] G. Morthier and P. Vankwikelberge, *Handbook of distributed feedback laser diodes*. Artech House, 1997.

[121] M. Körbl, A. Gröning, H. Schweizer, and J. L. Gentner, "Gain spectra of coupled ingaasp/inp quantum wells measured with a segmented contact traveling wave device," *Journal of Applied Physics*, vol. 92, no. 5, 2002.

[122] J. S. T. Smalley, M. W. Puckett, and Y. Fainman, "Invariance of optimal composite waveguide geometries with respect to permittivity of the metal cladding," *Optics Letters*, vol. 38, no. 23, pp. 5161–4, 2013.

[123] A. B. Miller, "Optical interconnects to silicon," *IEEE Journal of Selected Topics in Quantum Electronics*, vol. 6, no. 6, pp. 1312–1317, 2000.

[124] B. Jalali and S. Fathpour, "Silicon photonics," *Lightwave Technology, Journal of*, vol. 24, no. 12, pp. 4600–4615, 2006.

[125] N. Izhaky, M. T. Morse, S. Koehl, O. Cohen, D. Rubin, A. Barkai, G. Sarid, R. Cohen, and M. J. Paniccia, "Development of cmos-compatible integrated silicon photonics devices," *IEEE Journal of Selected Topics in Quantum Electronics*, vol. 12, no. 6, pp. 1688–1698, 2006.

[126] J. M. Fedeli, R. Orobtchouk, C. Seassal, and L. Vivien, "Integration issues of a photonic layer on top of a cmos circuit," vol. 6125, pp. 61250H–61250H–15, 2006.

[127] K. Ohira, K. Kobayashi, N. Iizuka, H. Yoshida, M. Ezaki, H. Uemura, A. Kojima, K. Nakamura, H. Furuyama, and H. Shibata, "On-chip optical interconnection by using integrated iii-v laser diode and photodetector with silicon waveguide," *Optics Express*, vol. 18, no. 15, pp. 15440–15447, 2010.

[128] T. Aalto, M. Harjanne, M. Kapulainen, S. Ylinen, and L. Morl, "Fast 100-channel wavelength selectors integrated on silicon," vol. 7943, pp. 79430V–79430V–9, 2011.

[129] J. Cunningham, A. Krishnamoorthy, R. Ho, I. Shubin, H. Thacker, J. Lexau, D. Lee, D. Feng, E. Chow, Y. Luo, X. Zheng, G. Li, J. Yao, T. Pinguet, K. Raj, M. Asghari, and J. Mitchell, "Integration and packaging of a macrochip with silicon nanophotonic links," *IEEE Journal of Selected Topics in Quantum Electronics*, vol. 17, no. 3, pp. 546–558, 2011.

[130] C. Hahn, Z. Zhang, A. Fu, C. H. Wu, Y. J. Hwang, D. J. Gargas, and P. Yang, "Epitaxial growth of ingan nanowire arrays for light emitting diodes," *ACS Nano*, vol. 5, no. 5, pp. 3970–3976, 2011.

[131] M. J. R. Heck, J. F. Bauters, M. L. Davenport, J. K. Doylend, S. Jain, G. Kurczveil, S. Srinivasan, and J. E. Bowers, "Hybrid Silicon Photonic Integrated Circuit Technology," *IEEE Journal of Selected Topics in Quantum Electronics*, vol. 19, no. 4, pp. 6100117–6100117, 2013.

[132] H. Park, A. W. Fang, O. Cohen, R. Jones, M. J. Paniccia, and J. E. Bowers, "Design and fabrication of optically pumped hybrid silicon-algainas evanescent lasers," *IEEE Journal of Selected Topics in Quantum Electronics*, vol. 12, no. 6, pp. 1657–1663, 2006.

[133] S. Srinivasan, A. W. Fang, D. Liang, J. Peters, B. Kaye, and J. E. Bowers, "Design of phase-shifted hybrid silicon distributed feedback lasers," *Optics Express*, vol. 19, no. 10, pp. 9255–9261, 2011.

[134] E. Goebel, G. Luz, and E. Schlosser, "Optical gain spectra of ingaasp/inp double heterostructures," *IEEE Journal of Quantum Electronics*, vol. 15, no. 8, pp. 697–700, 1979.

[135] L. A. Coldren and S. W. Corzine, *Diode lasers and photonic integrated circuits*. Wiley, 1995.

[136] J. Shimizu, H. Yamada, S. Murata, A. Tomita, M. Kitamura, and A. Suzuki, "Optical-confinement-factor dependencies of the k factor, differential gain, and nonlinear gain coefficient for 1.55 mu m ingaas/ingaasp mqw and strained-mqw lasers," *Photonics Technology Letters, IEEE*, vol. 3, no. 9, pp. 773–776, 1991.

[137] K. Srinivasan, M. Borselli, O. Painter, A. Stintz, and S. Krishna, "Cavity q, mode volume, and lasing threshold in small diameter algaas microdisks with embedded quantum dots," *Optics Express*, vol. 14, no. 3, pp. 1094–1105, 2006.

[138] M. Lamponi, S. Keyvaninia, C. Jany, F. Poingt, F. Lelarge, G. de Valicourt, G. Roelkens, D. Van Thourhout, S. Messaoudene, J.-M. Fedeli, and G. H. Duan, "Low-Threshold Heterogeneously Integrated InP/SOI Lasers With a Double Adiabatic Taper Coupler," *IEEE Photonics Technology Letters*, vol. 24, no. 1, pp. 76–78, 2012.

[139] B. Jensen and A. Torabi, "Refractive index of quaternary InGaAsP lattice matched to InP," *Journal of Applied Physics*, vol. 54, p. 3623, 1983.

[140] C. Genet and T. Ebbesen, "Light in tiny holes," *Nature*, vol. 445, no. 7123, pp. 39–46, 2007.

[141] K. Stubkjaer, M. Asada, S. Arai, and Y. Suematsu, "Spontaneous recombination, gain and refractive index variation for 1.6 microns wavelength InGaAsP/InP lasers," *Japanese Journal of Applied Physics*, vol. 20, pp. 1499–1505, 1981.

[142] A. Goi, K. Syassen, and M. Cardona, "Effect of pressure on the refractive index of Ge and GaAs," *Physical Review B*, vol. 41, no. 14, pp. 10104–10110, 1990.

[143] G. Theodorou and G. Tsegas, "Piezooptical Properties of GaAs and InP," *Physica Status Solidi (b)*, vol. 211, no. 2, pp. 847–868, 1999.

[144] J. Gerard and B. Gayral, "Strong Purcell effect for InAs quantum boxes in three-dimensional solid-state microcavities," *Journal of Lightwave Technology*, vol. 17, no. 11, pp. 2089–2095, 2002.

[145] A. L. Schawlow and C. H. Townes, "Infrared and optical masers," *Physical Review*, vol. 112, no. 6, p. 1940, 1958.

[146] C. H. Henry, "Theory of the linewidth of semiconductor lasers," *IEEE Journal of Quantum Electronics*, vol. 18, no. 2, pp. 259–264, 1982.

[147] P. Horak, N. Y. Voo, M. Ibsen, and W. H. Loh, "Pump-noise-induced linewidth contributions in distributed feedback fiber lasers," *IEEE photonics technology letters*, vol. 18, no. 9-12, pp. 998–1000, 2006.

[148] G. M. Stéphan, T. T. Tam, S. Blin, P. Besnard, and M. Têtu, "Laser line shape and spectral density of frequency noise," *Phys. Rev. A*, vol. 71, p. 043809, 2005.

[149] L. B. Mercer, "1/f frequency noise effects on self-heterodyne linewidth measurements," *Lightwave Technology, Journal of*, vol. 9, no. 4, pp. 485–493, 1991.